HASP 2019

Science Report of Payload # 7

University of North Florida and University of North Dakota

Measurements of Bad Ozone in Troposphere and Good Ozone in Stratosphere

Students Team:
Joseph Ward (UNF) (Team Leader),
Trevor Roger (UNF)

Faculty Advisors:
Dr. Nirmalkumar G. Patel
Department of Physics, University of North Florida, Jacksonville, FL 32224
and
Dr. Ron Fevig
Department of Space Studies, University of North Dakota, Grand Forks, ND 58202

Index

1. Introduction and Mission Objectives

University of North Florida (UNF)-University of North Dakota (UND) team have successfully flown payloads on the HASP balloon flights since 2008 and measured the ozone gas profile in the stratosphere. Based on the success and experience of previous flights and observation of interesting larger ozone peak in troposphere after termination of HASP2018 flight, the UNF-UND team proposed the HASP 2019 flight for the development of new improved version of ozone sensors and payload to measure good ozone profile in the stratosphere and bad ozone in the troposphere. In addition, we are interested to explore the measurements of nocturnal ozone maxima before launching of the flight during early morning as well as in the troposphere after termination of flight at nighttime. The objectives of proposed HASP2019 flight science experiment were to measure good ozone in stratosphere, bad ozone in troposphere and any possible observation of higher concentration of ozone due to nocturnal ozone maxima after termination of flight at nighttime. About 90% of ozone is concentrated between 15 and 32 kilometers above the earth's surface (stratospheric ozone). Tropospheric ozone found at ground level in lower concentrations where it is a key component of smog over major cities. The atmospheric layers defined by changes in temperature are shown in fig.1 (a), while the presence of ozone layer in the stratosphere is shown in fig. 1(b).

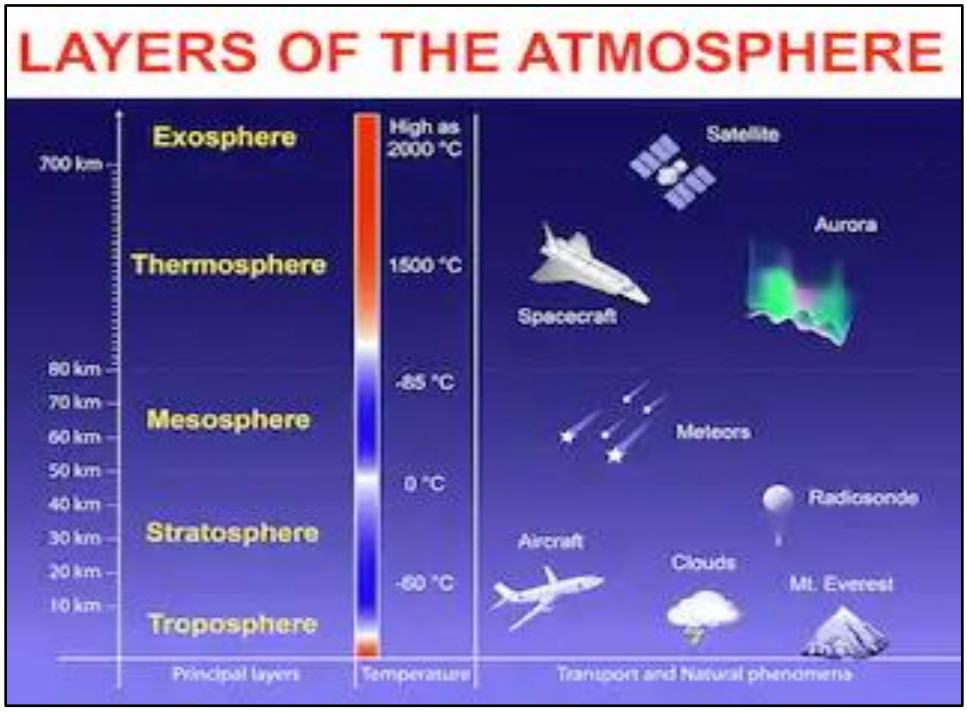

Fig.1 (a) shows the atmospheric layers defined by changes in temperature.
Picture Courtesy: https://scied.ucar.edu/atmosphere-layers

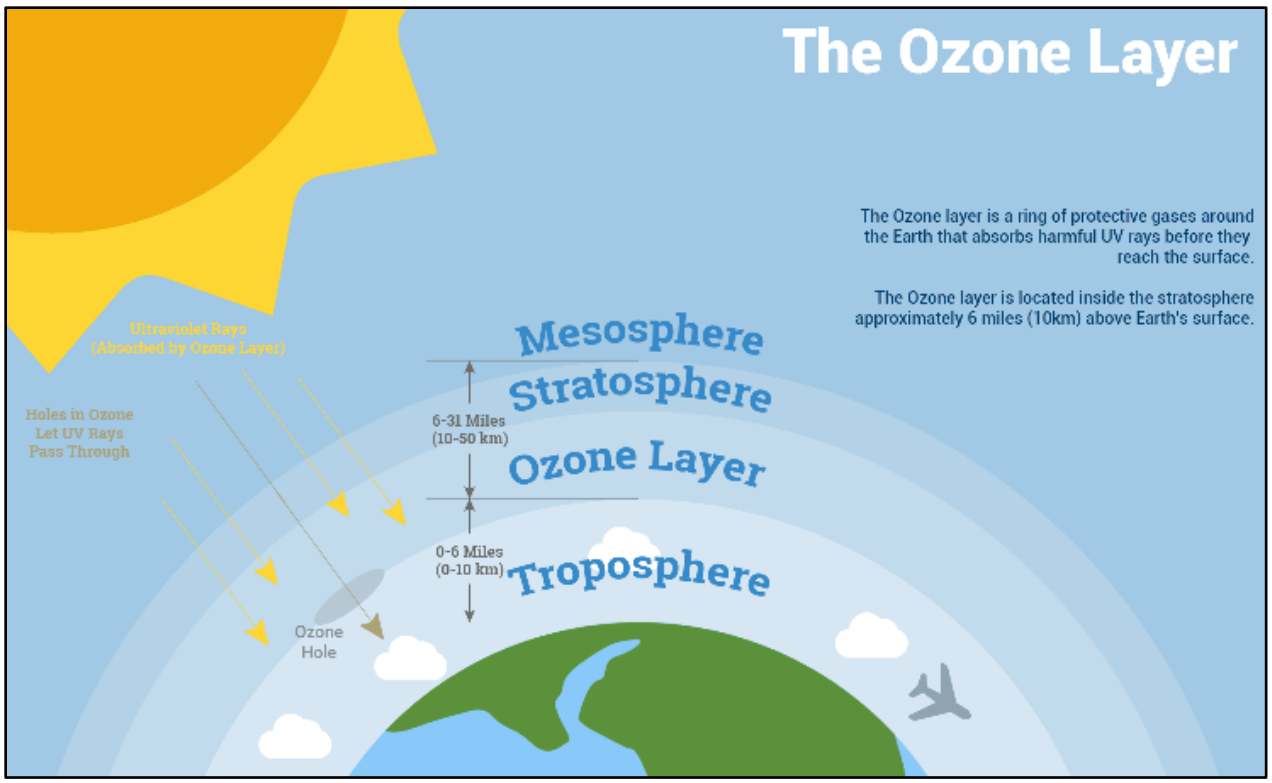

Fig.1 (b) The Ozone layer in the stratosphere.
Picture Courtesy: https://www.whatarethe7continents.com/the-ozone-layer-what-how-formed-important/

Generation of Ozone in the Stratosphere: Oxygen gas (O_2) is present in the atmosphere. High energy or shorter wavelength UV light ($h\nu$) collides with the oxygen molecule (O_2), causing it to split into two oxygen atoms. These atoms are unstable, and they prefer being "bound" to something else. The free oxygen atoms then smash into other molecules of oxygen, forming ozone (O_3).

$$O_2 + h\nu \rightarrow O_1 + O_1$$

$$O_{1\ (atom)} + O_{2\ (Oxygen\ gas)} \rightarrow O_{3\ (Ozone)}$$

The overall reaction between oxygen and ozone formation is:

$$3\ O_2 \rightarrow 2\ O_3$$

The ozone destroyed in the process that protects us from UV-B and UV-C rays emitted by the Sun. When ozone (O_3) absorbs UV light *(hv)*, it will split the molecule into one free oxygen atom (O_1) and one molecule of oxygen gas (O_2). Thus, absorption of UV-B and UV-C leads to the destruction of ozone

$$O_{3\ (Ozone)} + h\nu \rightarrow O_{1\ (atom)} + O_{2\ (Oxygen\ gas)}$$

Ozone is valuable to us because it absorbs harmful UV radiation during its destruction process (fig.2 (a)). A dynamic equilibrium established in these reactions. The ozone concentration varies due to the amount of radiation of light received from the sun.

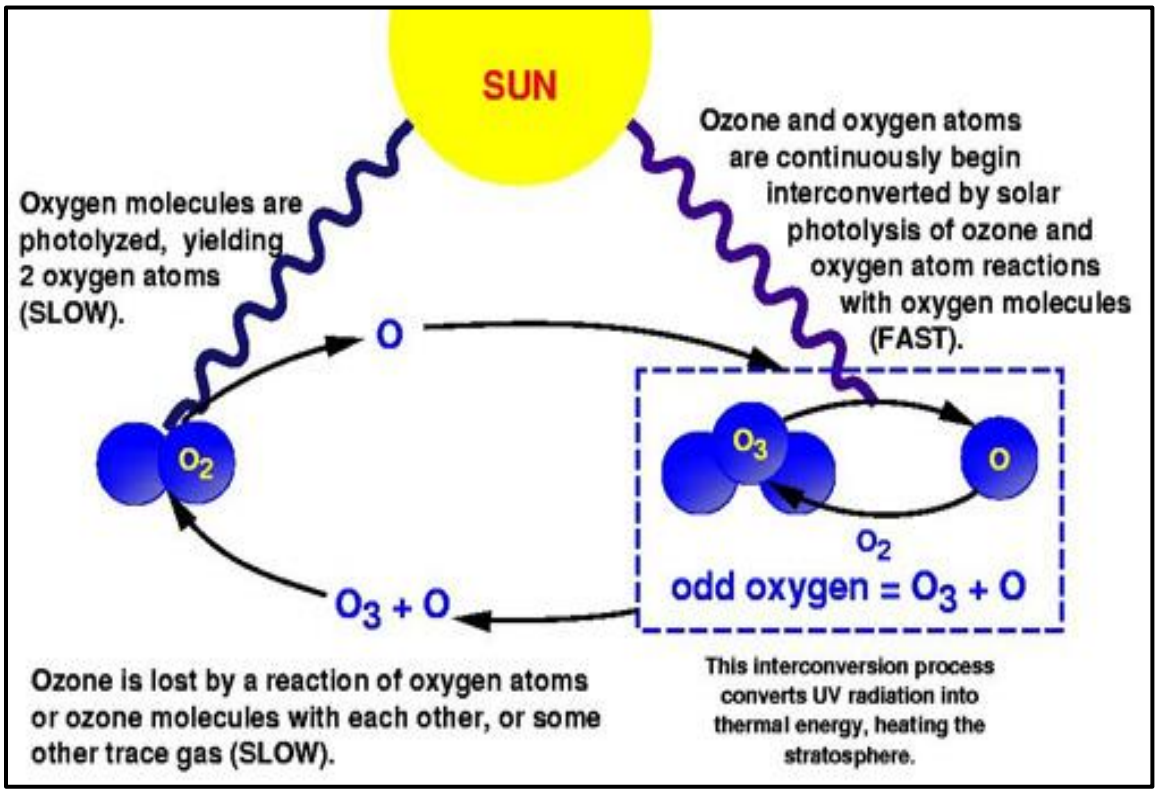

Fig. 2(a) Generation of ozone in the presence of UV light in stratosphere.
Picture Courtesy: https://environment-chemistry.weebly.com/ozone-depletion.html

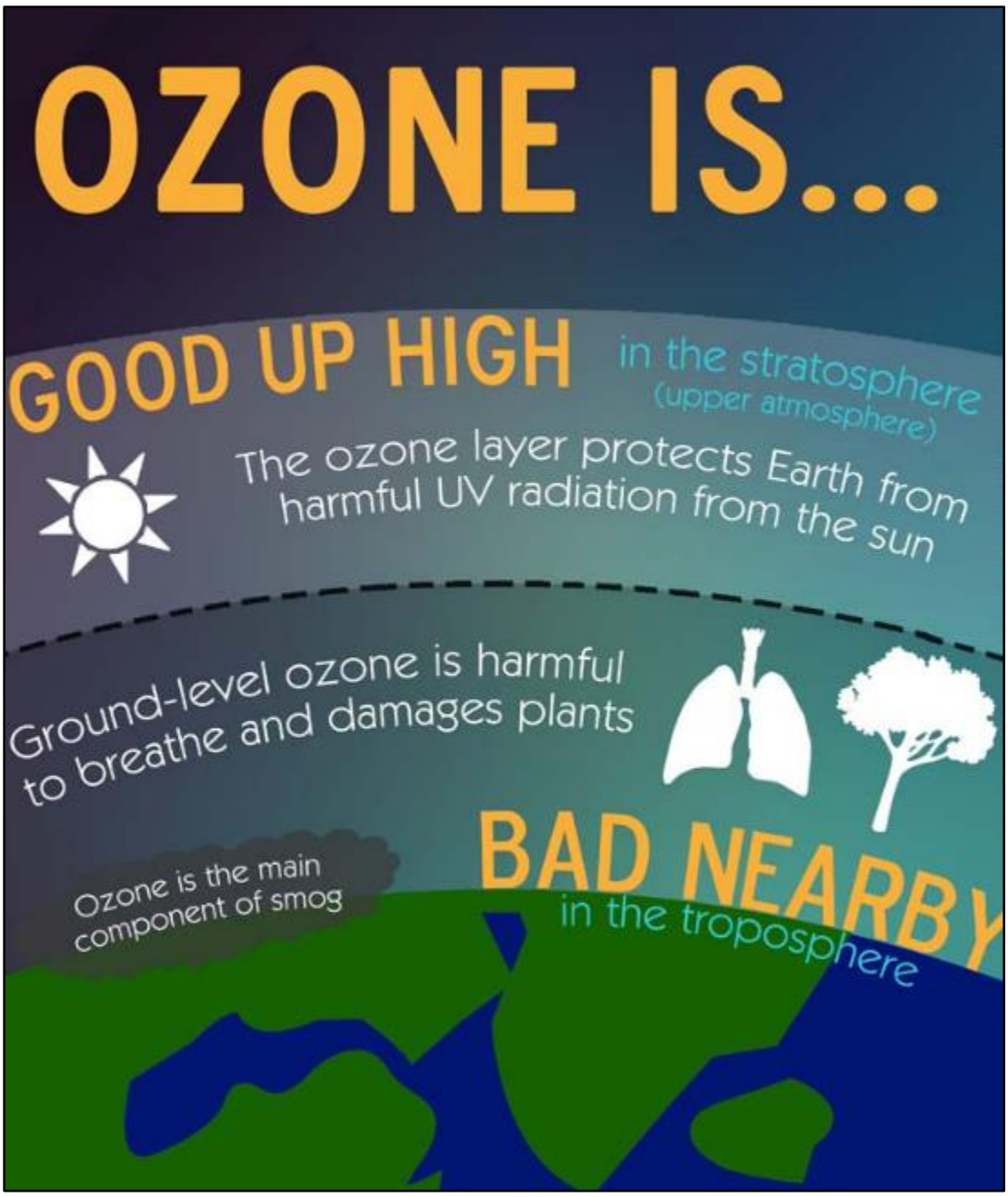

Fig. 2 (b) Good and bad ozone.
Picture Courtesy: https://www.ourair.org/gooduphigh-badnearby-ozone-infographic/

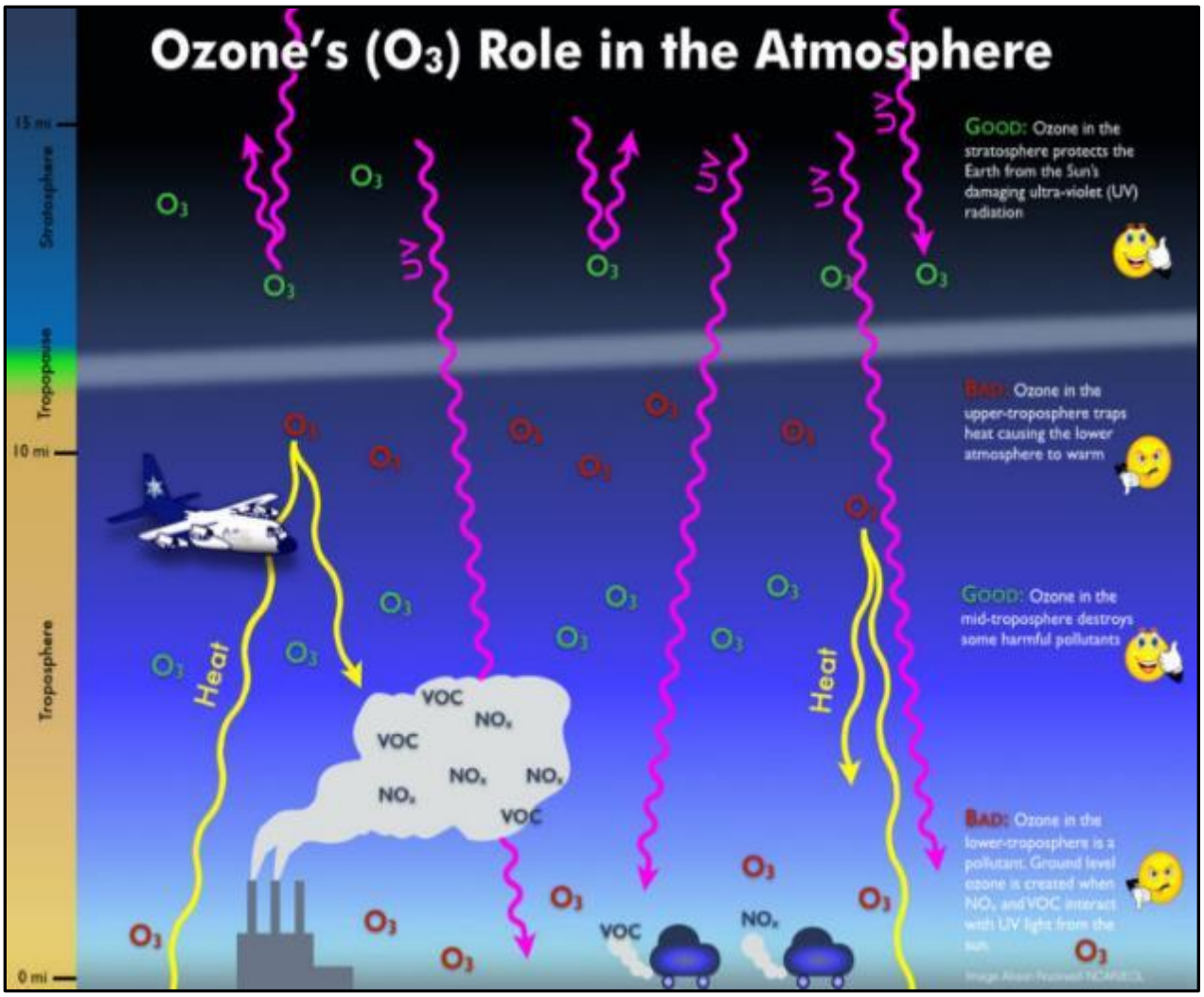

Fig. 2 (c) Ozone's role in the atmosphere.
Picture Courtesy: https://www.weathernationtv.com/news/ozone-action-days-mean/

Generation of Ozone in the Troposphere: Ozone in the troposphere is bad. This ozone is contributing to the smog and greenhouse gases created by human activities, which is shown in fig.2 (b) (c) and (d). Ozone close to the ground surface does not exist in high enough concentrations to shield us from UV light.

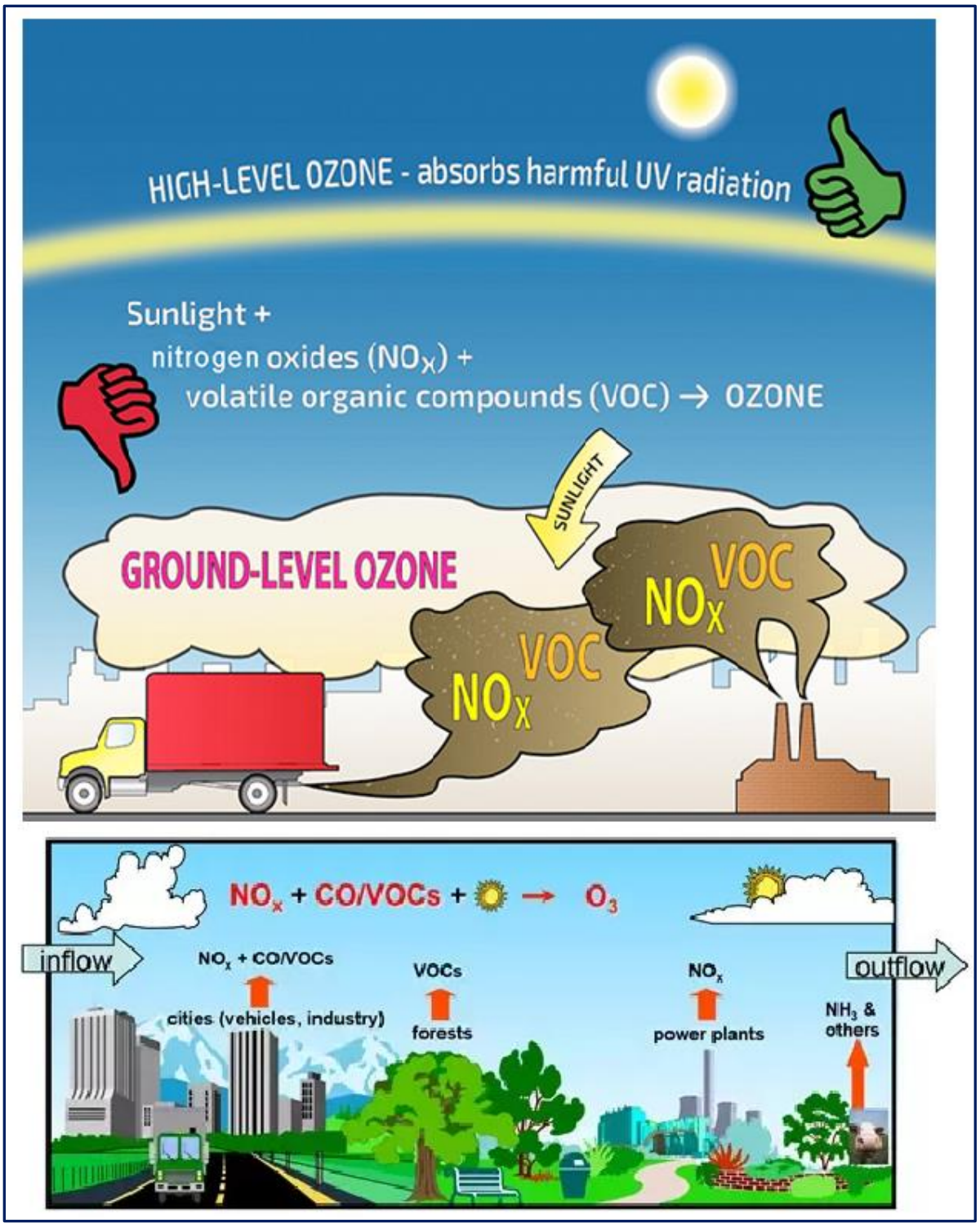

Fig. 2(d) Formation of bad ozone in the troposphere by NOx, VOC and sunlight.

Bad ozone creates the respiratory problem, destroys polymers and reduces the plant growth. Fig. 2 (e) shows how bad ozone, the main ingredient in smog, is the most dangerous.

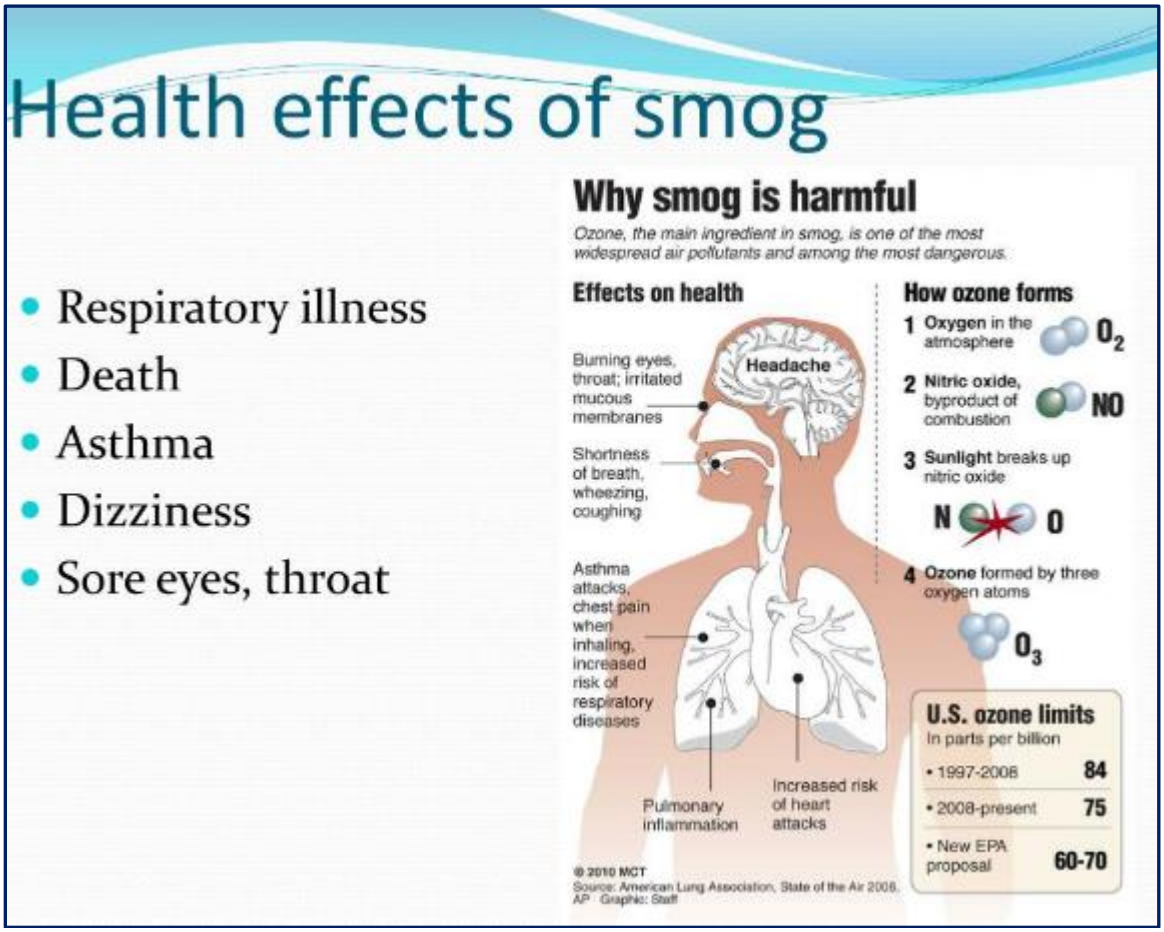

Fig. 2 (e) Health effects of smog
https://www.slideserve.com/fausto/smog-cities

Ozone depletion and Ozone Hole

Pollutant gases, particularly, reactive halogen gases such as chlorine and bromine compounds in the atmosphere are responsible to cause the ozone depletion, which mainly observed in the `ozone hole' over Antarctica and over the North Pole. Most of the chlorine, and nearly half of the bromine in the stratosphere, where most of the depletion has observed, comes from human activities. Fig. 2 (f) shows the production of ozone and destruction of ozone in the presence of UN light. Fig 2(f) also shows the life cycle of the chlorofluorocarbons (CFCs); how they are transported up into the upper stratosphere/lower mesosphere, how sunlight breaks down the compounds and then how their breakdown products descend into the polar vortex.

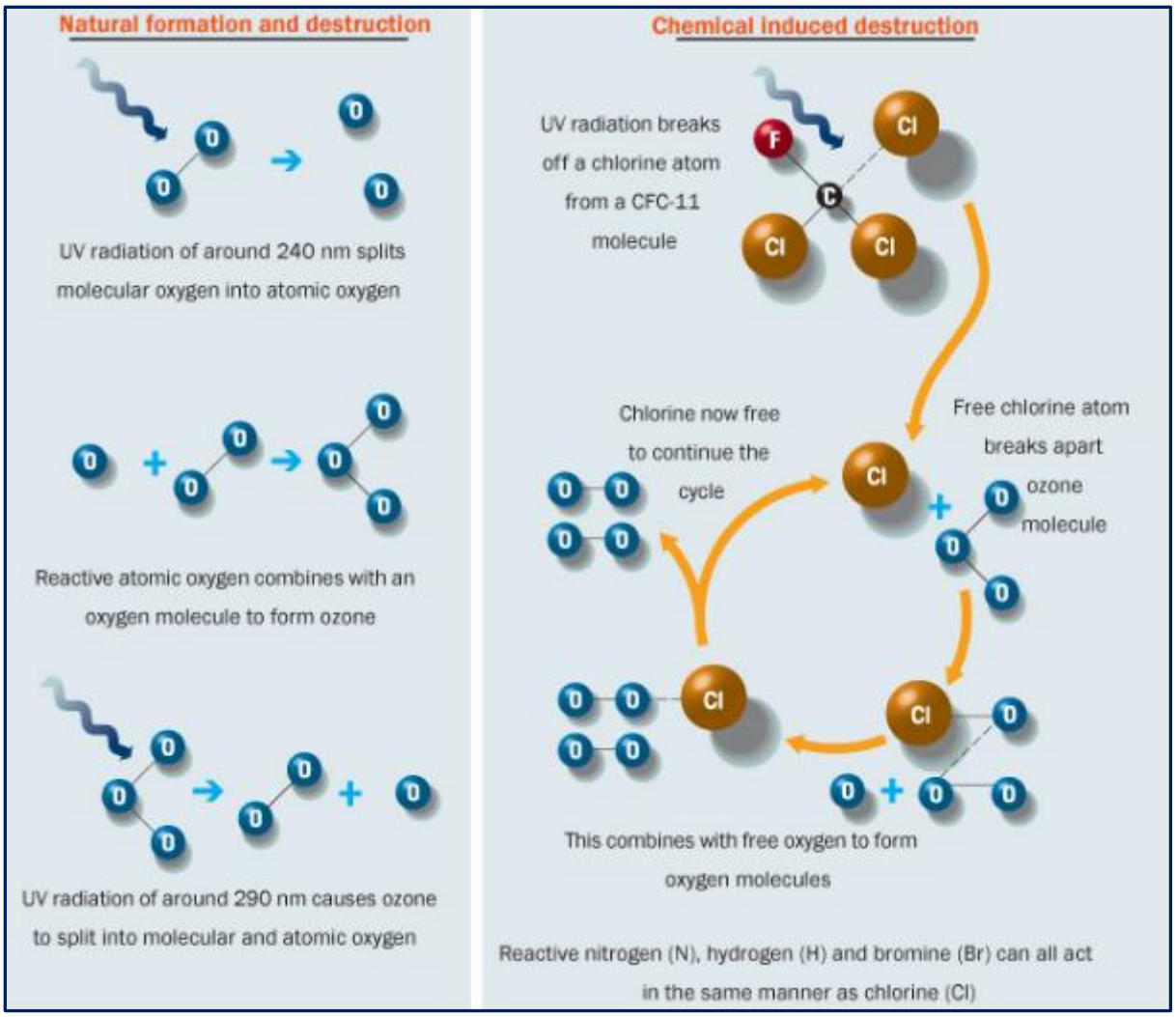

Fig. 2 (f), Natural formation and destruction of ozone and Chemical induced destruction of ozone.

Substances such as CFCs, HCFCs, Halons and methyl bromide, that lower the ozone layer do not directly destroy ozone. First they undergo photolysis, forming hydrogen chloride (HCl) or chlorine nitrate (ClONO2), molecules that do not react with ozone directly, but slowly decompose, giving, among other things, a small number of chlorine atoms (Cl) and Of chlorine monoxide (ClO) molecules that catalyze the destruction of ozone.
The reactions involved in the processes of destruction are more than 100, but can simplified in the following:
Cl + O 3 ——> ClO + O 2
ClO + O ——> Cl + O 2
Net effect: O 3 + O ——> 2 O 2

The chlorine atom acts as a catalyst and it is not consumed in the reaction, so it destroys thousands of ozone molecules before disappearing. The bromine atom is even more destructive than chlorine (about 10 or 100 times more). On the other hand, along with this, the chlorine concentrations are very low in the stratosphere and the bromine concentrations are even lower.

Mechanism of Ozone hole – The criticality of ozone layer can understood from the fact that, only 10 or less of every million molecules of air is ozone. The majority of these ozone molecules reside in a layer between 10 and 40 kilometers above the surface of the Earth known as stratosphere. Each spring in the stratosphere over Antarctica (spring in the southern hemisphere is from September through November.), atmospheric ozone is rapidly destroyed by chemical processes. As winter arrives, a vortex of winds develops around the pole and isolates the polar stratosphere. When temperatures drop below -78 °C, thin clouds form of ice, nitric acid, and sulfuric acid mixtures. Chemical reactions on the surfaces of ice crystals in the clouds release active forms of CFCs. Ozone depletion begins, and the ozone “hole” appears (Fig. 2 (f)).

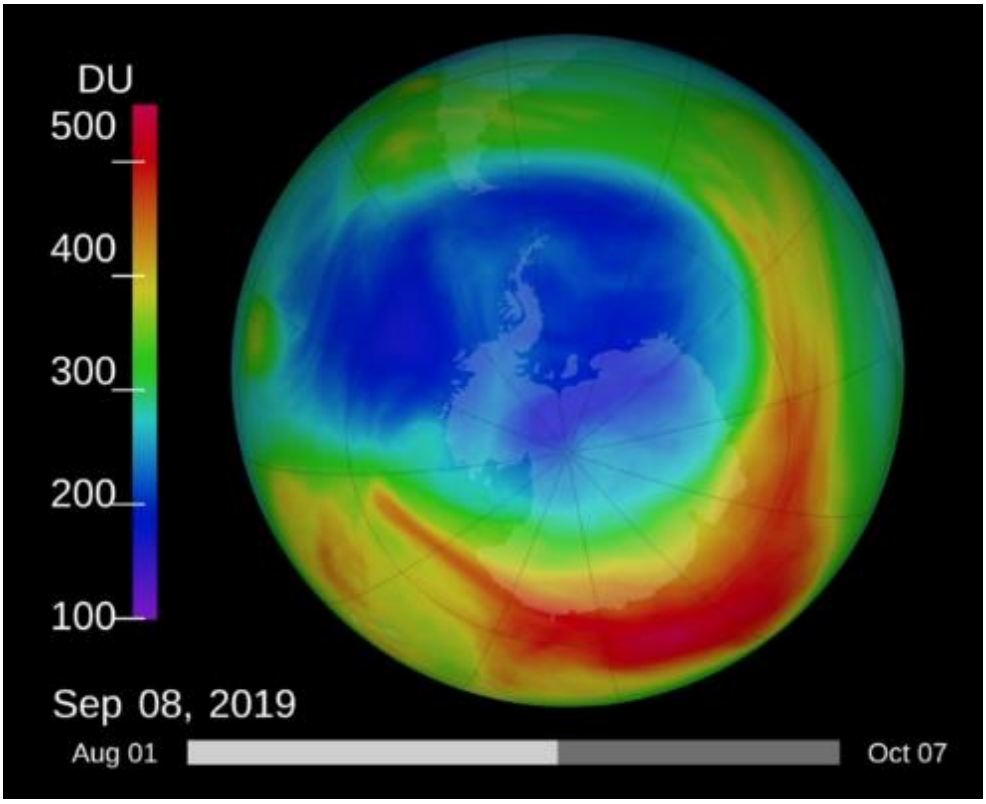

Fig 2 (f) Ozone hole
Picture Courtesy: https://research.noaa.gov/article/ArtMID/587/ArticleID/2566/2019-ozone-hole-smallest-on-record

About 50% of the total column amount of ozone in the atmosphere disappears during two to three months. At some levels, the losses approach 90%. This has come to call the Antarctic ozone hole. In spring, temperatures begin to rise, the ice evaporates, and the ozone layer starts to recover. Thus, ozone "hole" is a reduction in concentrations of ozone high above the earth in the stratosphere. The ozone hole is defined geographically as the area wherein the total ozone amount is less than 220 Dobson Units. The ozone hole has steadily grown in size and length of existence over the past two and half decades. Now, the size of ozone hole over Antarctica is estimated to be about 30 million sq. km. Synthetic chlorines, primarily chloroflourobcarbons (CFCs), contribute to the thinning of the ozone layer and allow larger quantities of harmful ultraviolet rays to reach the earth.

Looking into this global issue of ozone depletion, we are continuously working on the development and improvement of ozone sensors and low weight sensors payload to measure the ozone profile in the stratosphere on the real time mode using the HASP balloon flight since 2008. HASP-NASA provided a platform for 12 small payloads and 4 large payloads. The maximum mass limit was 20 kg for a large payload and 3 kg for a small payload. UNF and UND jointly had one small payload to measure the ozone profile in the stratosphere. UNF team

fabricated the gas sensors system, payload body, microcontroller circuit, software, and electronic communication circuits. The HASP had an onboard computer, power supply batteries, GPS, video camera, and communication link for all payloads.

UNF team was participated the workshop at the NASA-Columbia Scientific Balloon Facility (CSBF) in Palestine, Texas during July 15 to 19, 2019 for the integration of the sensors payload with the HASP. Ozone sensor payload was integrated with the HASP platform. The UND-UNF payload successfully passed all required thermal vacuum tests and certified for the flight. Then, NASA-CSBF successfully launched the HASP2019 flight (#698N) on September 5, 2019 from Fort Sumner, New Mexico. After spending 7 hour and 37 minutes at about 37,000 m. it landed in rugged terrain West of White Mesa, Utah. The CSBF recovery truck has not be able to find a route that can used to drive up to or near the payload. A helicopter retrieved the gondola. During the flight, the UNF ozone sensors array detected and measured ozone in the stratosphere. The payload sent out the data files during the flight without any problem. Our payload was recovered with minor damage. This report described the technical details, pictures and science results of the ozone sensors payload.

2. Fabrication of Nanocrystalline Thin Film Gas Sensors

Ozone sensors were fabricated by UNF team at Dr. Patel's Sensors Laboratory at the UNF. Fig.3 (a) and (b) shows thermal vacumm depositon system and electron beam deposition system, respectively, were used to fabricate nanocrsyaline nanocomposite thin film gas sensors for the detection of ozone gas.

Fig. 3 (a) Thermal vacuum depsoition system and (b) electron beam depsoition system.

Fig. 4(a) shows the top view of one typical low magnification scanning electron microscope image of the Indium Tin Oxide (ITO) thin film gas sensor having two gold electrodes for external electrical contacts. Fig. 4 (b) shows a typical array of 8 ITO thin film gas sensors fabricated on an approximately 2.5cm x 2.5cm ultra cleaned glass slide. The glass slides were throughlly cleaned by the ultrasonic cleaner, detergent, solvant and baked in the ovan. The interface of the cicuit board to the array is also shown in fig. 4(b).

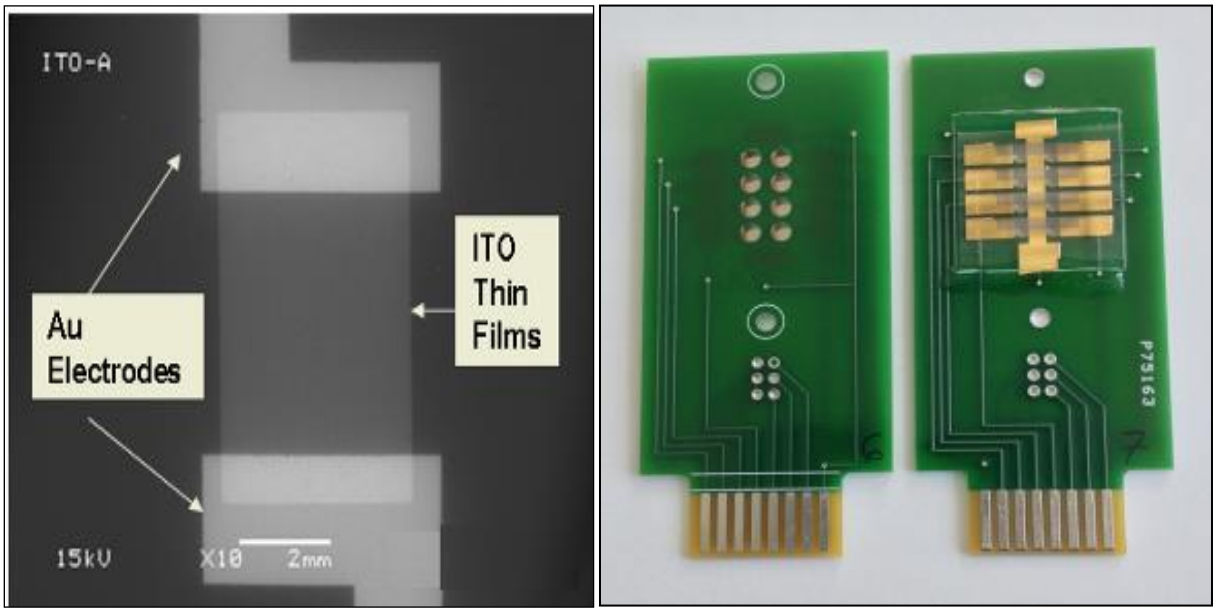

Fig.4 (a) Scanning electron microscope image of top view of one ITO thin film gas sensor (Size: 2 x2 mm), (b) Top and bottom view of 8 gas sensor array interface with the printed circuit board (Size: 4 x 7 cm) (UNF US Patent 9,606,078).

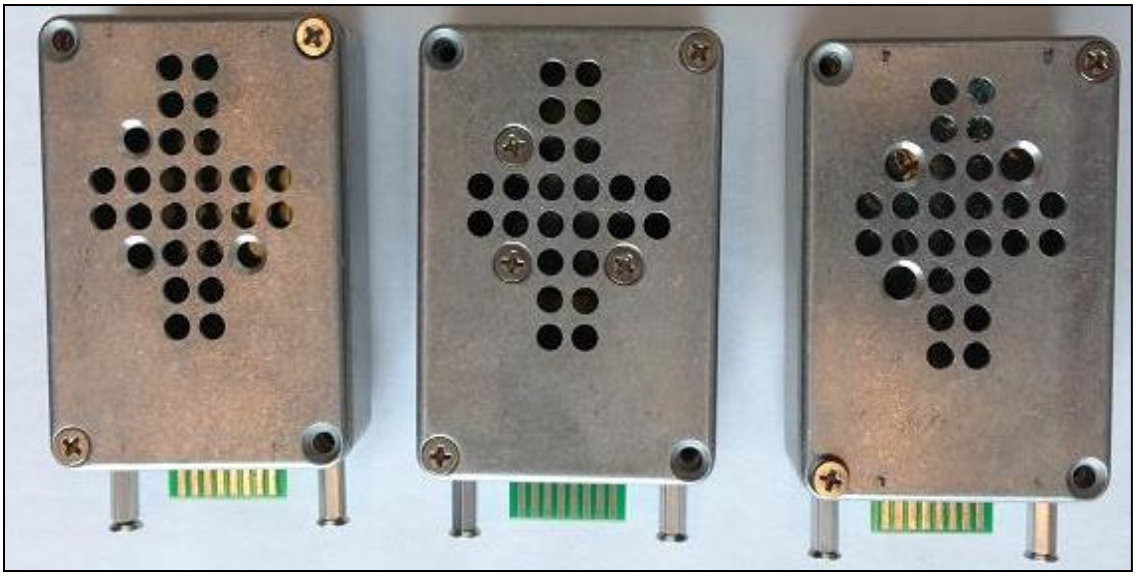

Fig. 4(c) Sensors boxes # 1, 2 and 3. Size of box: 5.5 x 2.5 x 8.0 cm.

Three types of sensor array boxes were fabicated as shown in Fig. 4(c). Each type of sensor array was mounted in a separate box. In addition to the sensors box for the payload, three backup sensors PCB boxes were fabricated. UNF students' team calibrated sensors several times and then tested in the thermal vacuum test chamber at CSBF, Palestine, TX.

We fabricated several new sensors at different growth conditions every year in order to improve the performance and optimization of fabrication parameters such as thickness of film, substrate temperature, deposition rate and doping concnetration, etc.

Box #1 sensors are nanocrystalline ITO thin film deposited on glass for detection of good ozone.
Box #2 sensors are WO_{3-x}+ITO thin films deposited on glass for detection of good ozone.
Box #3 sensors are nanocomposite of α-phase of Ag_2WO_4 +ITO thin films deposited on glass for detection of bad ozone in Atmosphere / Troposhere and nocturnal ozone.
Backup Box # 4, 5 and 6, Backup PCB # 7, 8 and 9.

Fig. 5 (a) shows the picture of housing for the UNF sensors, consisting of an array of 8 gas sensors interfaced with a printed circuit board (PCB), flexible Kapton heater (MINCO make HK 5573R30.0 L12BU), temperature sensor (Analog Device TMP36), electrical fan (SUNON, MC25060V2-0000-A99, DC 5V, 0.38W) and a 16 wires flat cable. One end of flat cable has a female card edge connector to connect sensor PCB (Make 3M, MCS16K-ND), while another end has 16 pin female to connect microcontroller PCB.

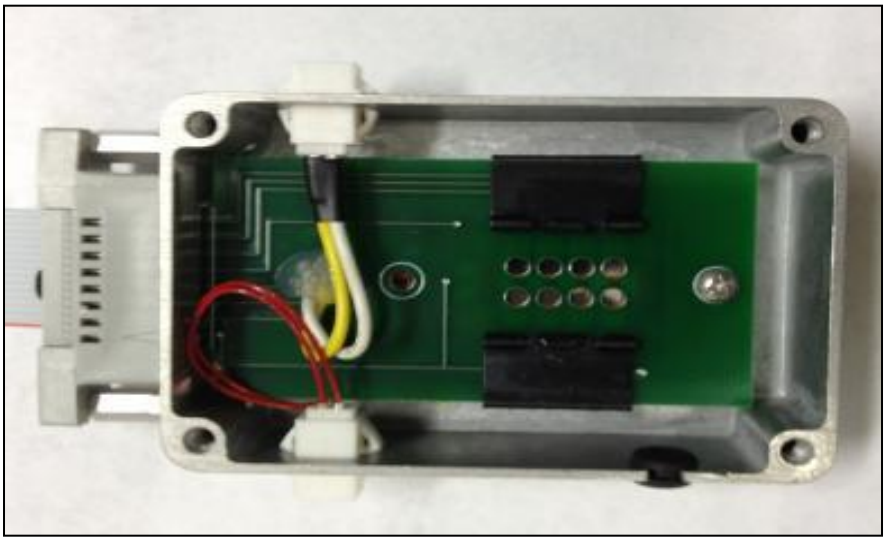

Fig.5 (a) Inner view of UNF Ozone sensors box.

Fig. 5(b) and (c) shows the pin information of sensor PCB and connector.

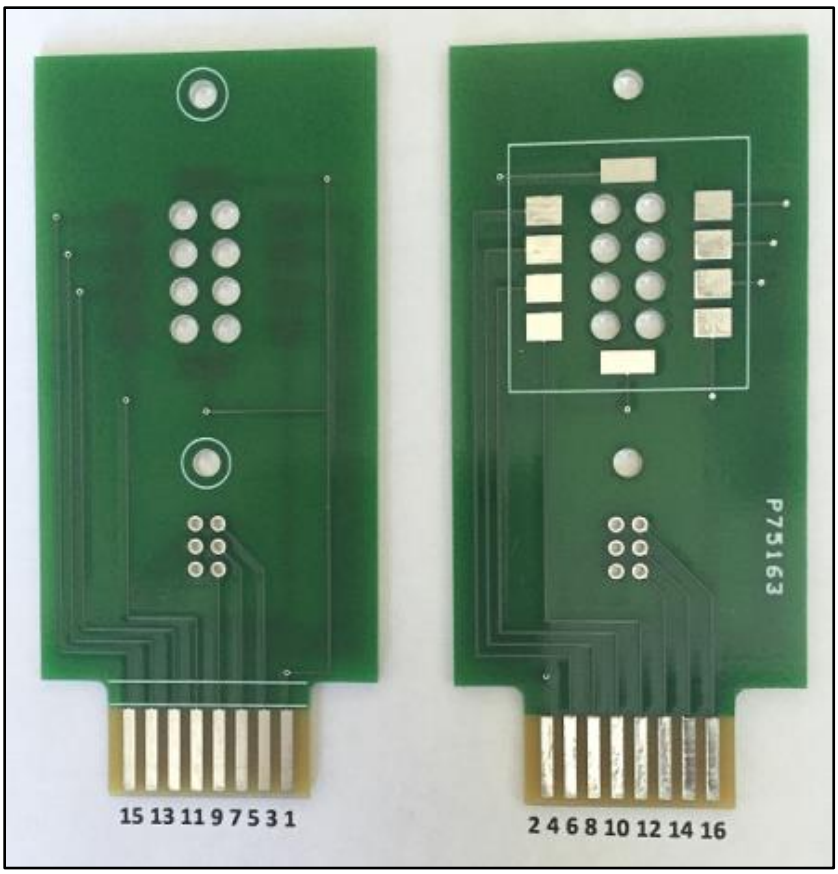

Fig.5 (b) Pin numbers of sensor PCB.

Pin number per connector datasheet							
1	3	5	7	9	11	13	15
Common	Temp Sensor	Temp Sensor	Temp Sensor	Gas Sensor	Gas Sensor	Gas Sensor	Gas Sensor
Open	Gas Sensor	Gas Sensor	Gas Sensor	Gas Sensor	Light Sensor	Light Sensor	Pin not used
2	4	6	8	10	12	14	16
Pin number per connector datasheet							

Fig.5 (c) Pin information for connection of 16 pins female card edge connector with sensor PCB

3. Working Principles of Gas Sensors

Interaction of oxidizing gas on surface of n-type ITO thin film sensor

Upon adsorption of charge accepting molecules at the vacancy sites, namely from oxidizing gases such as ozone (O_3), these electrons are effectively depleted from the conduction band of ITO. This leads to an increase in the electrical resistance of n-type ITO.

For ozone gas:

Oxygen vacancy (V) + Ozone (O_3) →Lattice Oxygen site (O_o) + O_2

Vacancies can be filled by the reaction with ozone. Filled vacancies are effectively electron traps and consequently the resistance of the sensor increases upon reaction with ozone.

Interaction of reducing gas on surface of n-type ITO thin film sensor

Oxygen vacancies on ITO surfaces are electrically and chemically active. These vacancies function as n-type donors decreasing the electrical resistivity of ITO. Reducing gases such as CO, H_2 and alcohol vapors result in detectable decreases in the electrical resistance of n-type ITO.

For reducing gas, e.g. methanol:

CH_3OH (methanol) + O^- (chemisorbed ion on surface of ITO)

→ HCOH (Formaldehyde) + H_2O (water) + e^- (electron)

Vapors incident the surface and react with chemisorbed oxygen ions O- or O^{2-} and re-inject electrons into the conduction band.

In summary, the electrical resistance of ITO increases in the presence of oxidizing gases such as ozone. Upon adsorption of the charge accepting molecules at the vacancy sites, namely oxidizing gases such as ozone, electrons are effectively depleted from the conduction band, leading to an increase in the electrical resistance of n-type ITO. Note that our three different types of sensors boxes have n-type semiconductor gas sensors.

Dobson Spectrophotometer

Spectrometer invented by Gordon Dobson in 1924. Used to measure both total column ozone and profiles of ozone in the atmosphere. It measures total ozone by measuring the relative intensity of the dangerous UVB radiation that reaches the Earth and comparing to that of UVA radiation at ground level. If all of the ozone removed from the atmosphere, the amount of UVB radiation would equals the amount of UVA radiation on the ground. As ozone does exit in the atmosphere, the spectrometer can use the ration between the UVA and UVB radiation on the ground to determine how much ozone is present in the upper atmosphere to absorb the UVC radiation.

Units for measurement of ozone

I**n the presence study, we used part per million (ppm) units for determination of ozone concentration. We calibrated our sensors in the closed chamber using a digital ozone meter, which has unit in ppm only.** Ozone is measured by the Dobson spectrometer in Dobson Units (DU). Our sensors are very cheap, smaller in size, low mass and easy to interface with electronic compared to that of Dobson spectrometer.

1 Dobson Unit (DU) is defined to be 0.01 mm thickness of gas at STP (0ºC, 1 atm); the ozone layer represented above is then ~300 DU.

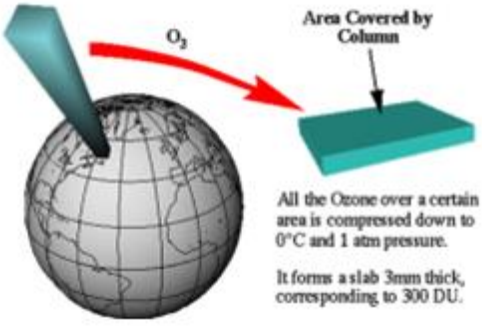

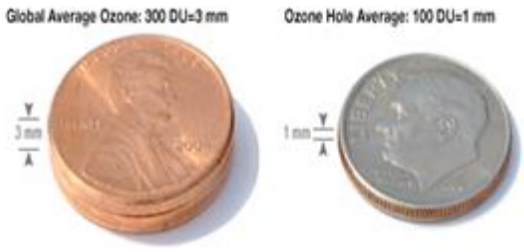

4. Calibration of Gas Sensors

The ITO sensors array was first tested and calibrated in the test chamber at UNF. The test chamber was adjusted to the identical coonditions of temperature and pressure as in the startosphere. Fig. 6(a) and (b) shows the pictures of ozone generator and detector used for the calibration of sensors. An ozone gnerator (Ozone Solutions, Model# OMZ-3400) was used as the source of ozone, which generated 0 to 12 ppm ozone gas.

A digital ozone detector (Eco Sensors, Inc., Model:A-21ZX) was used to measure the concentration of ozone in part per million (ppm). The Keithley digital multimeters and electrometers attached with comoputer having LabView program wereused for the measurements of the ITO sensor's resistance.

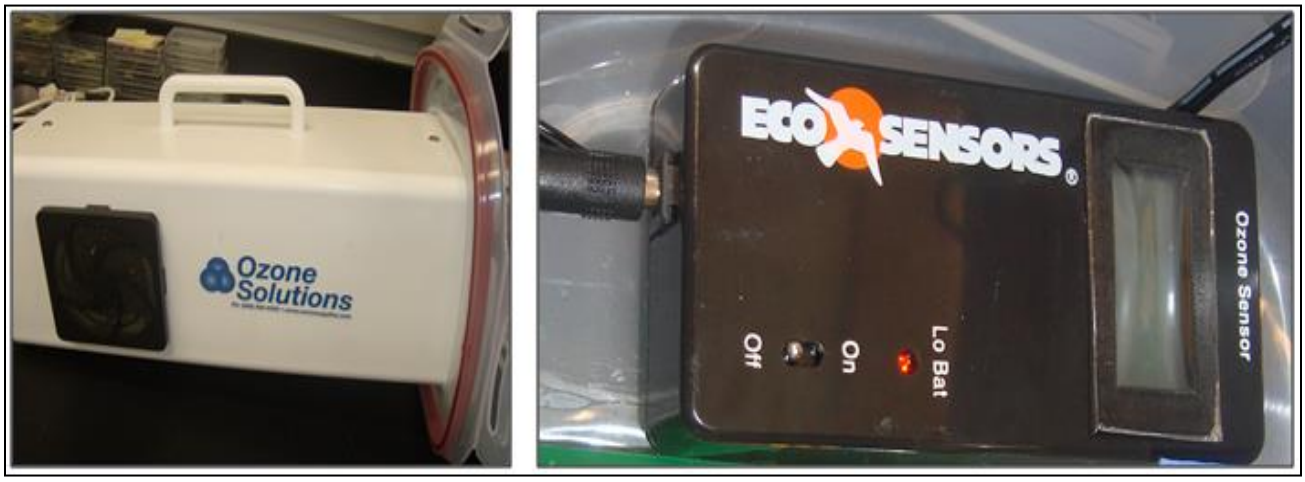

Fig.6(a) Ozone generator and (b) digital ozone detector.

All the 24 sensors of sensors box was calibrated simulataneously under indetical conditions of pressure, temepratue and concnetration of ozone in the test chamber. The sensors were calibrated with ozone gas in the range of 0.02 to about 10.00 ppm in the test chamber in the same run. The usual variation of ozone in the stratosphere is about 3.0 to 10.0 ppm. The measured data fit linearly and trend line equations for each plot were determined.

Fig.7 (a) show the calibration plots ozone sensors Box#1 having sensors # S1-1 to S1-8. These sensors were made of nanocrystalline ITO thin film gas sensors fabricated on the glass.

Figs.7 (b) show the calibration plots ozone sensors Box#2 having sensors # S2-1 to S2-8. These sensors were made of nanocomposite of WO_{3-x}+ITO thin film fabricated on the glass.

The calibration fit parameters of all three sensors Box checked before flight and after flight and receiving payload back. The calibration fit parameters of sensors Box # 3 before and after flight did not match within 2-sigma variation. There may possibility of change of α phase of silver tungstate to β phase of silver tungstate and lose sensitivity. Therefore, the calibration plots ozone sensors Box#3 are not presented here. These sensors were made of nanocomposite of Ag_2WO_4+ITO thin film fabricated on the glass.

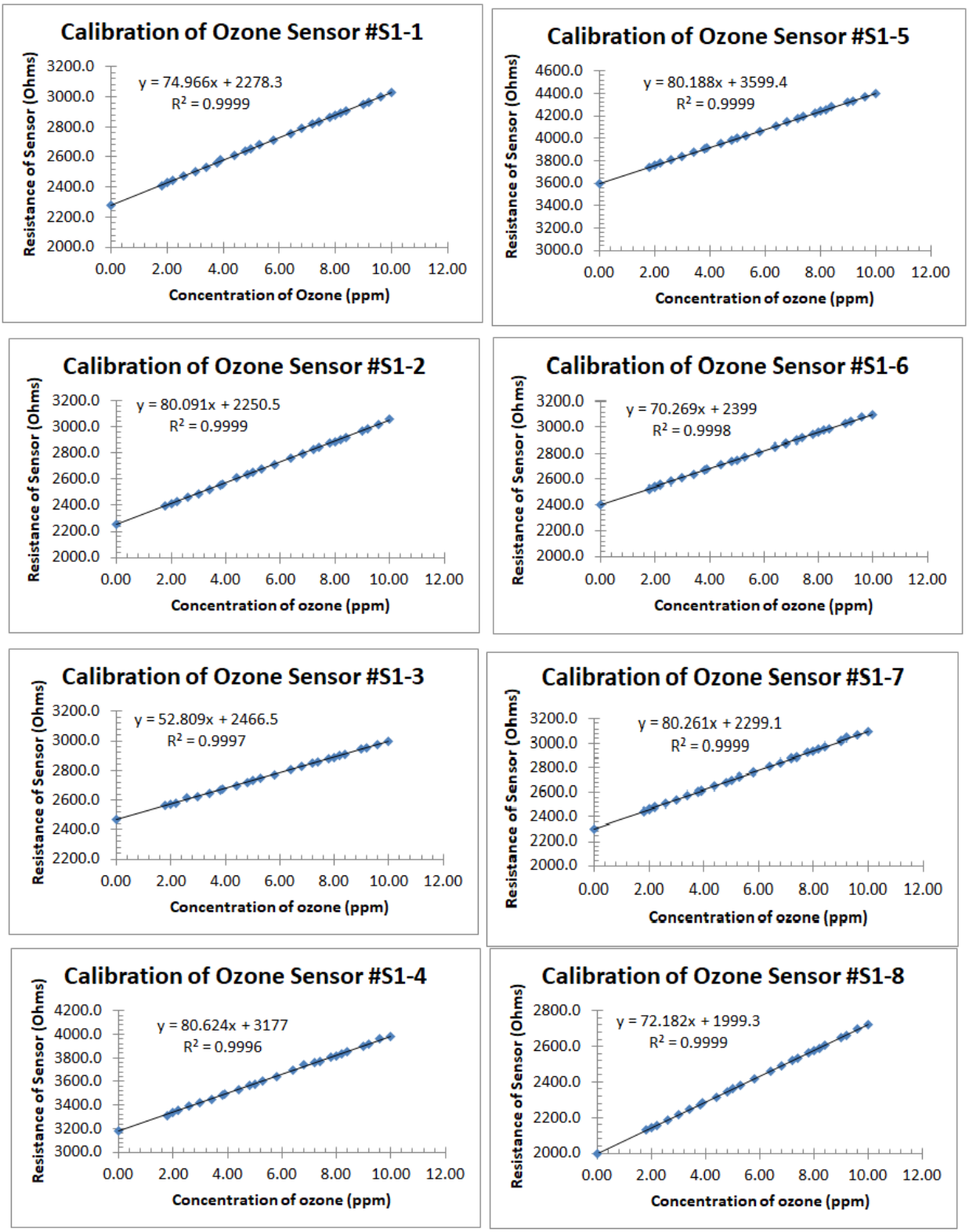

Figs.7 (a) show the calibration plots ozone sensors Box#1 having ITO thin film gas sensors # S1-1 to S1-8.

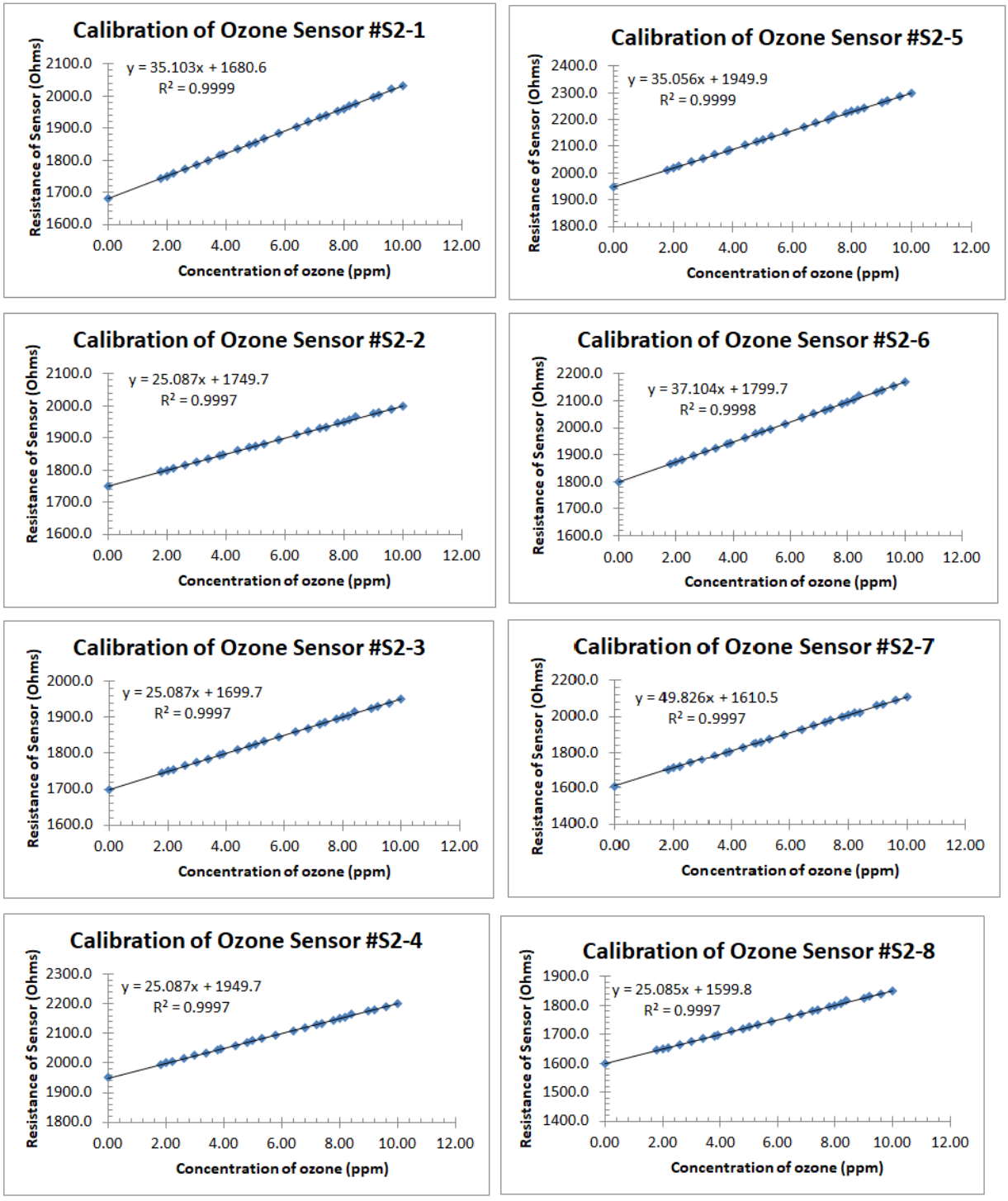

Figs.7 (b) show the calibration plots ozone sensors Box#2 having WO_{3-x}+ITO thin film gas sensors # S2-1 to S2-8.

Small variations in the slope and y-intercept values were observed due to the variation of sensor thickness and experimental error. Note that the calibration algorithm for each layer such as atmosphere, troposphere and stratosphere based on pressure and temperature were applied to determine the concentration of ozone in the entire range of altitude

5. Fabrication of Payload Body

The payload retained it's easy to open and close design utilizing the top plate for access to the PCB as well as all sensor boxes. The payload continues to feature a rectangular design due to its robustness as well as for its low rate of outgassing under extreme pressure drops. This design is optimal for the team's goal of a reusable payload body. The details of design and drawing and fabrication work are shown in fig.8 (a) to (r). UNF team made new design and drawings of the payload body using AutoCAD. UNF students did fabrication work of the payload boy in the UNF workshop. The height of 2018 payload was about 228.6 mm (≈ about 9 inches).

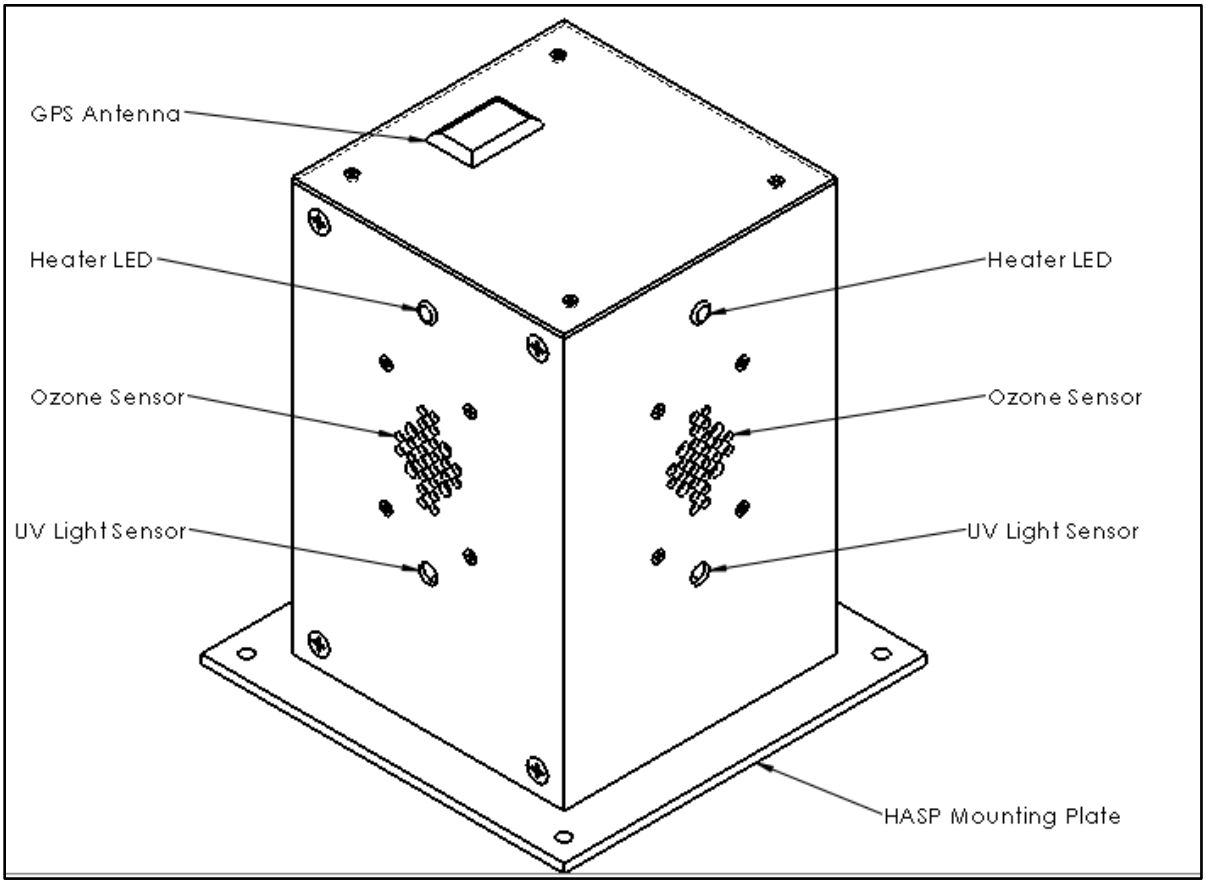

Fig.8 (a) Design of payload body.

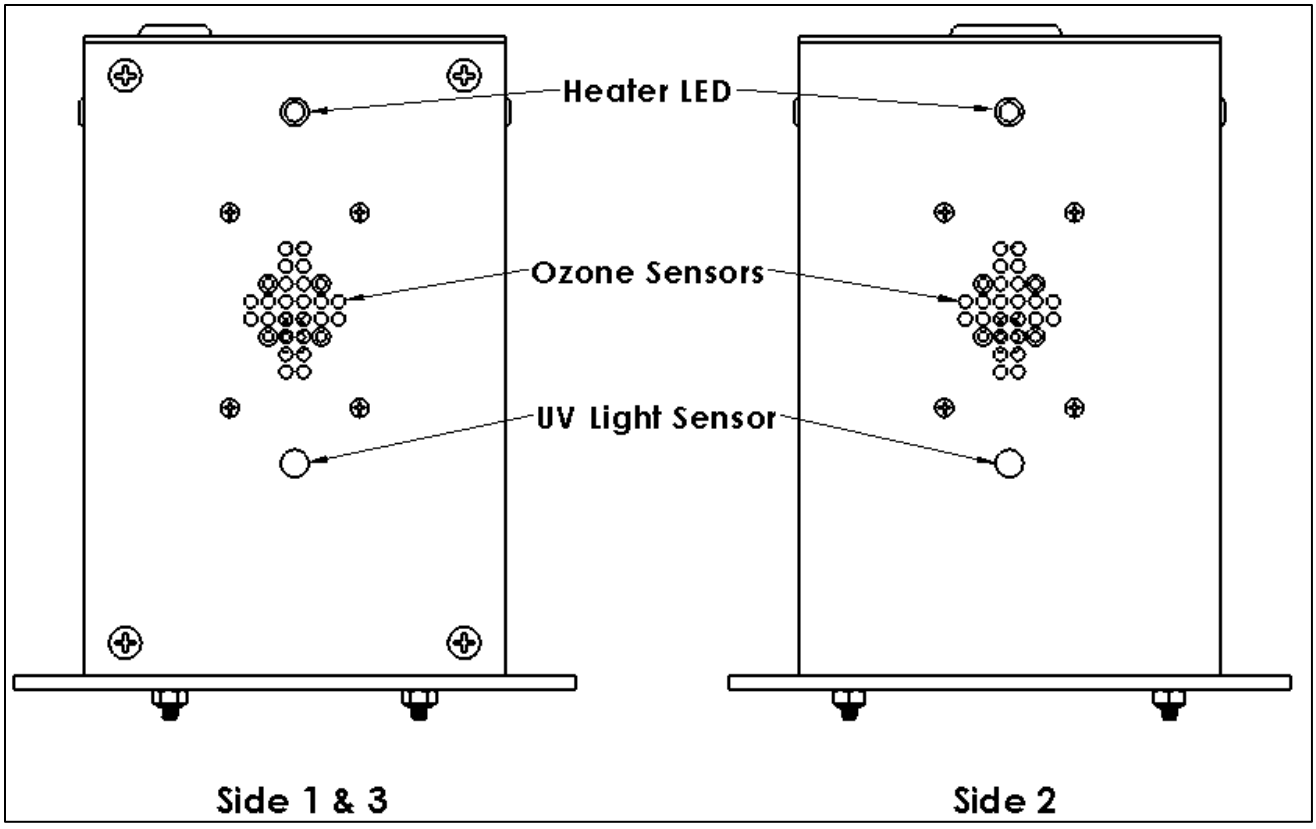

Fig. 8 (b) Side view design of the payload

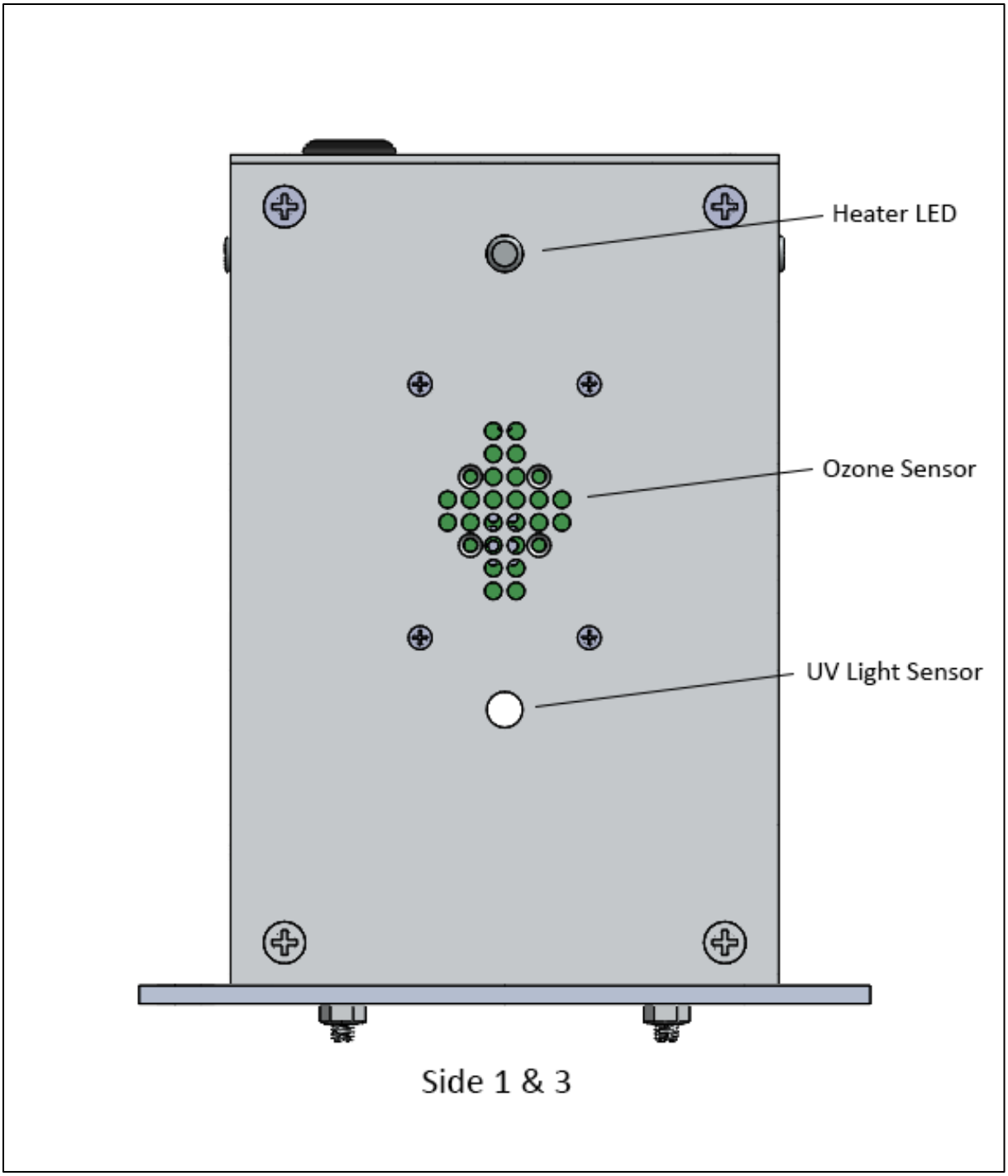

Fig. 8(c) Outer view of design of sides # 1 and 3 of the payload

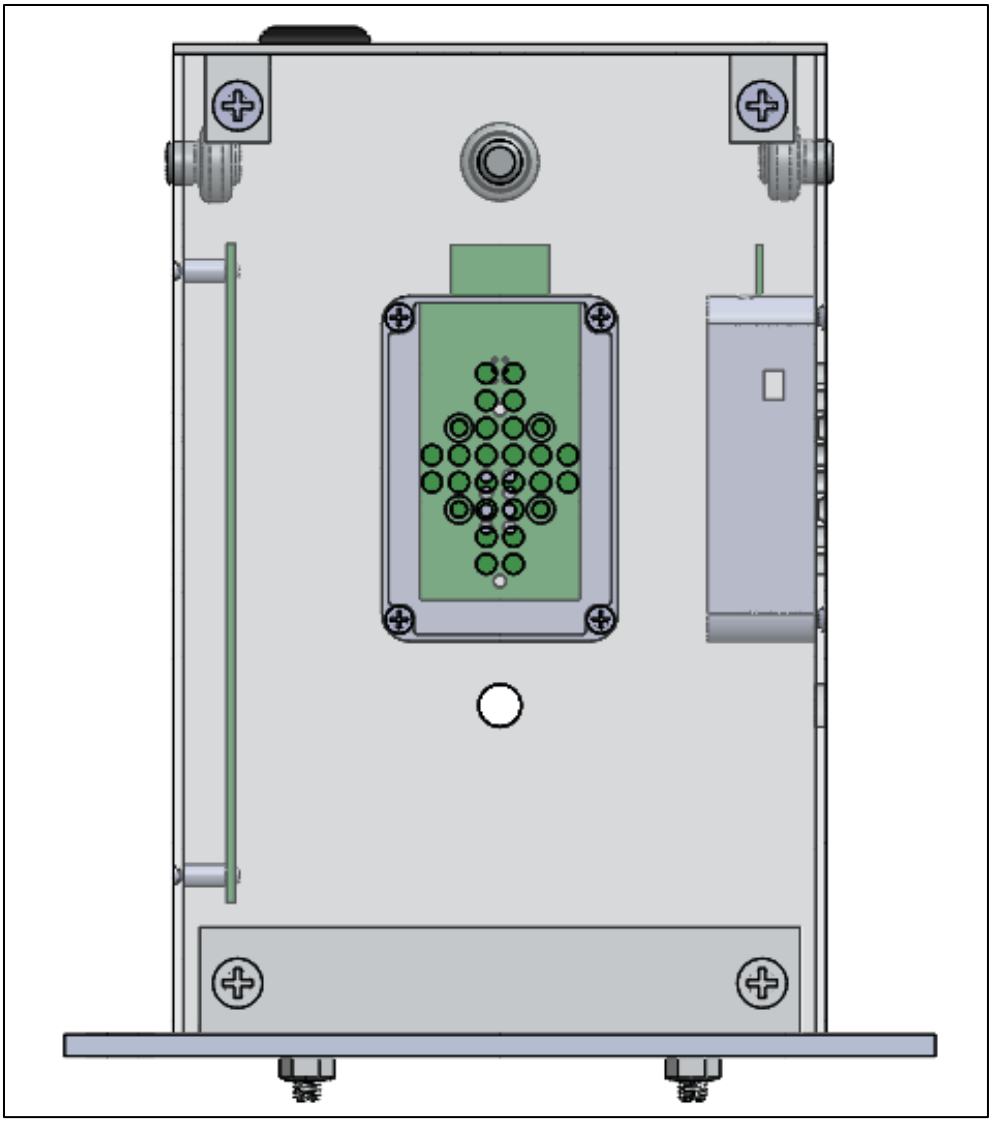

Fig. 8(d) Inside view of design of sides # 1 and 3 of the payload

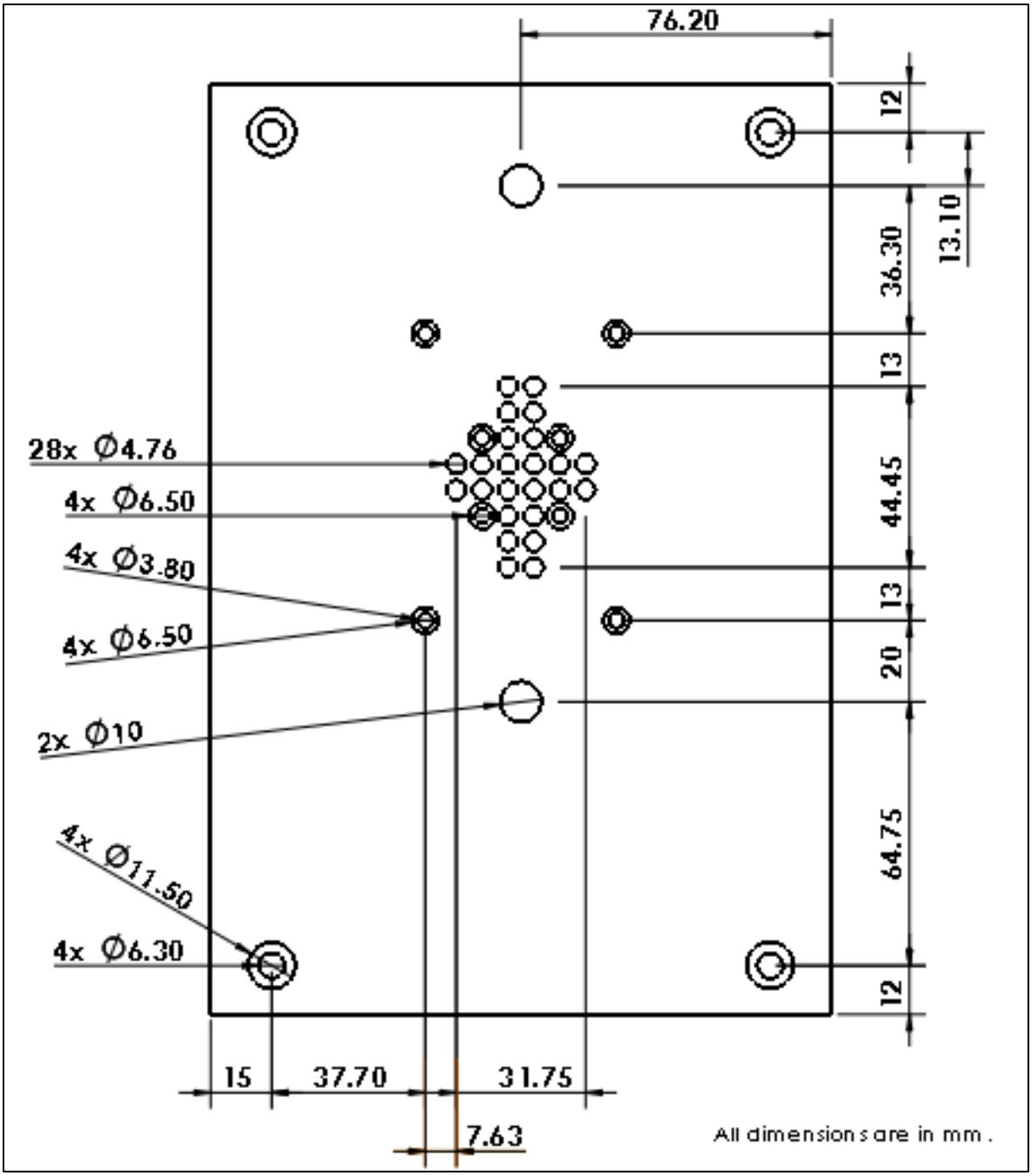

Fig. 8(e) Design with dimensions of sides # 1 and 3 of the payload

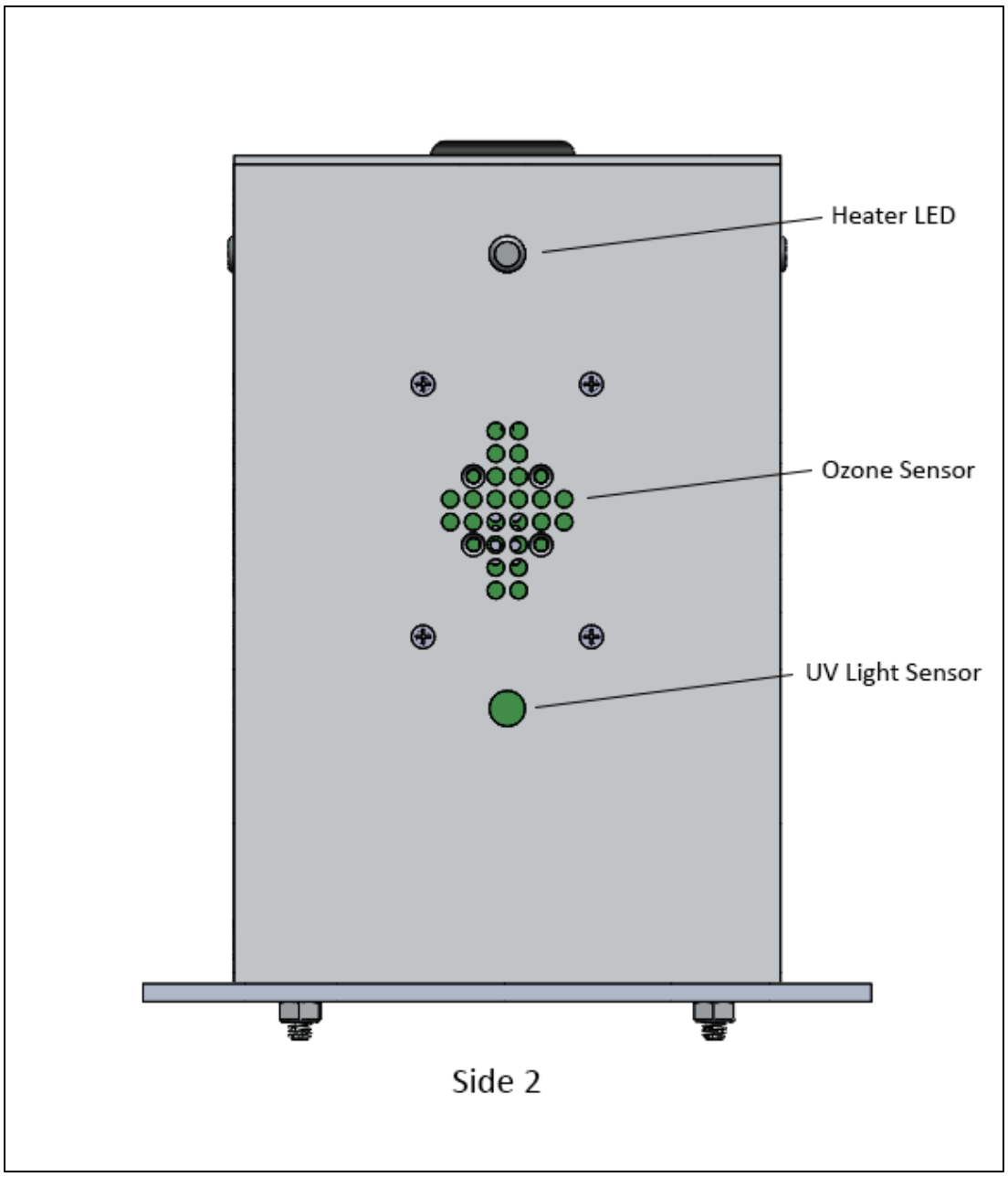

Fig. 8(f) Outer view of design of side # 2 of the payload

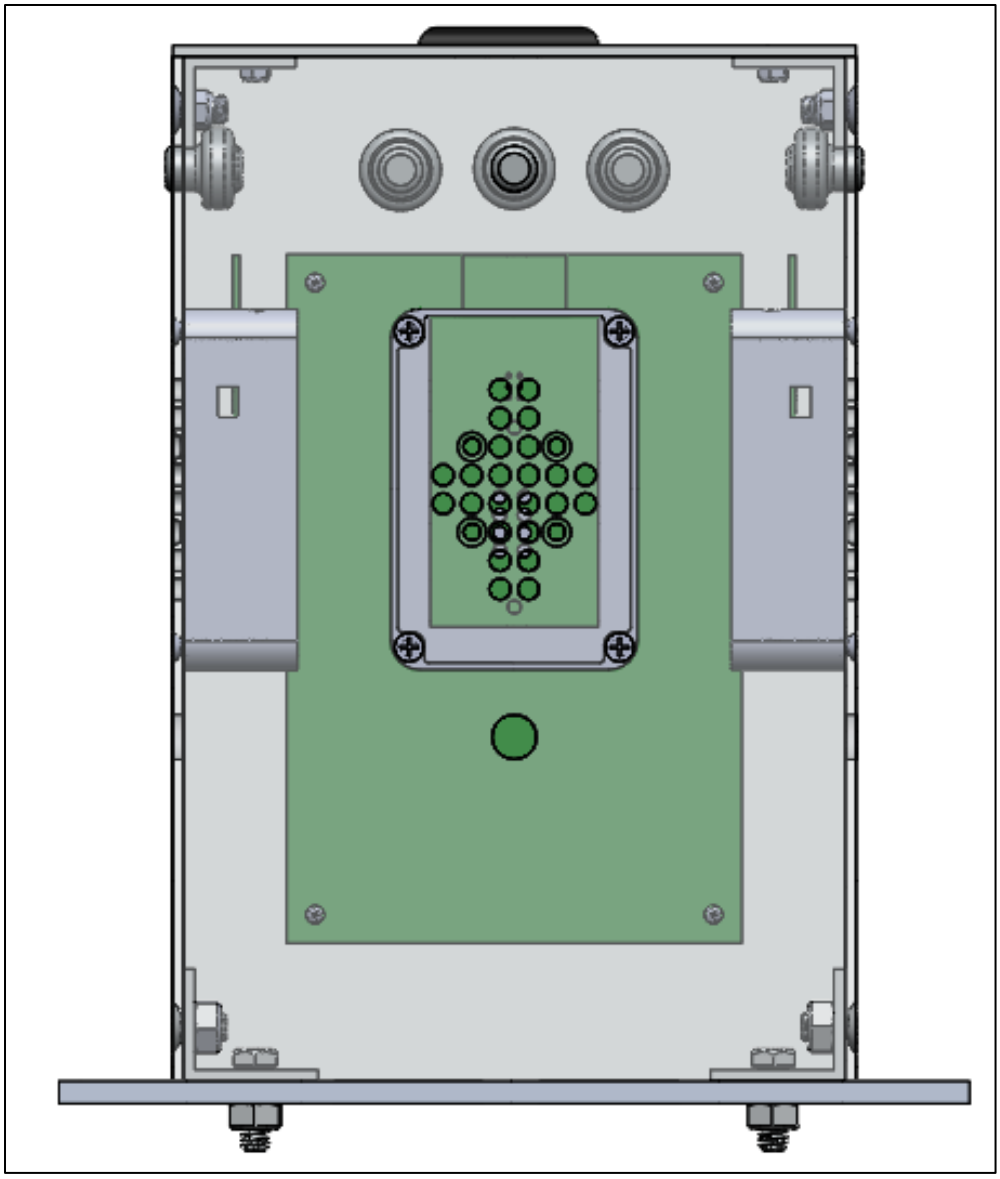

Fig. 8(f) Inside view of design of side # 2 of the payload

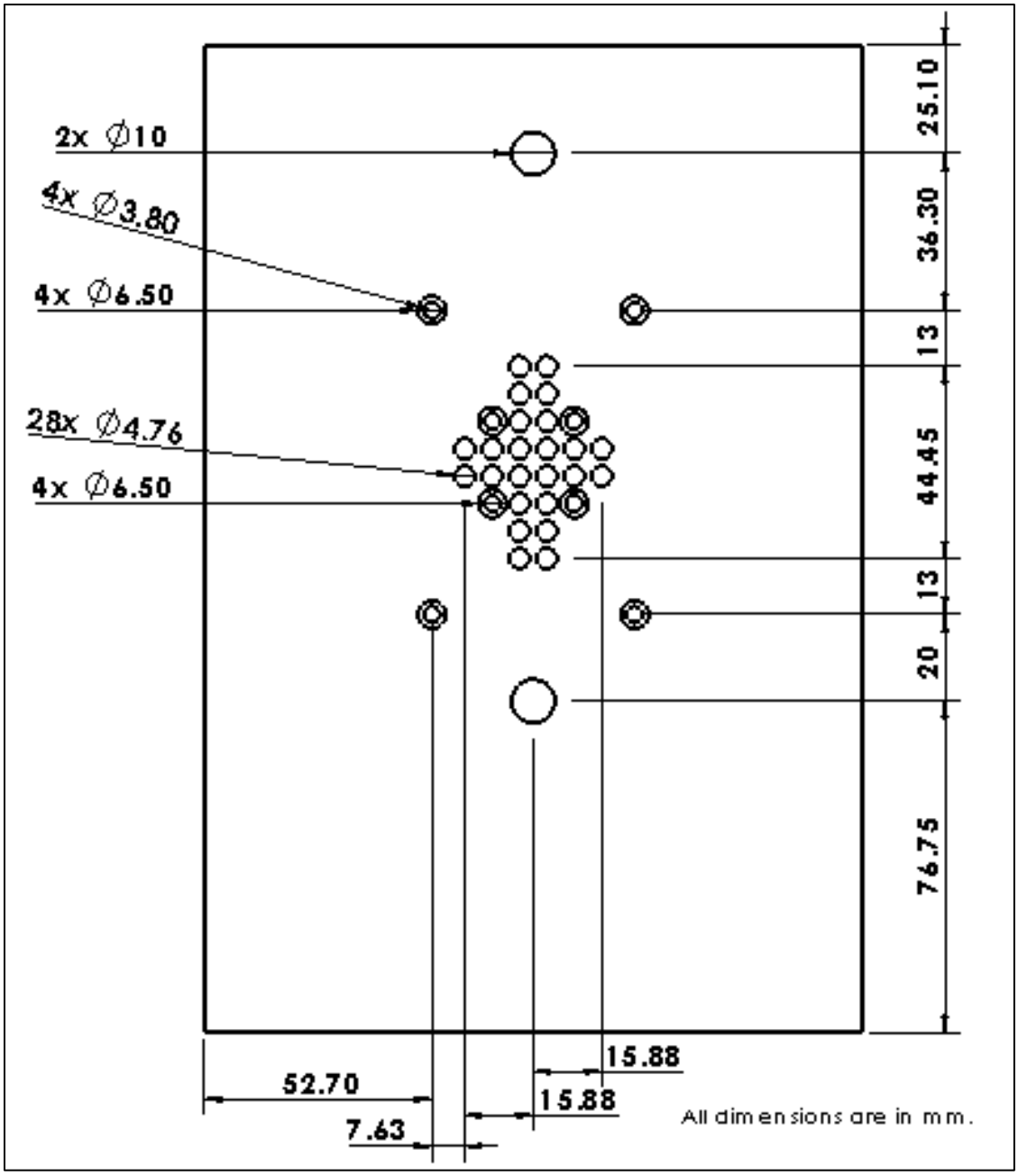

Fig. 8(g) Design with dimensions of side # 2 of the payload

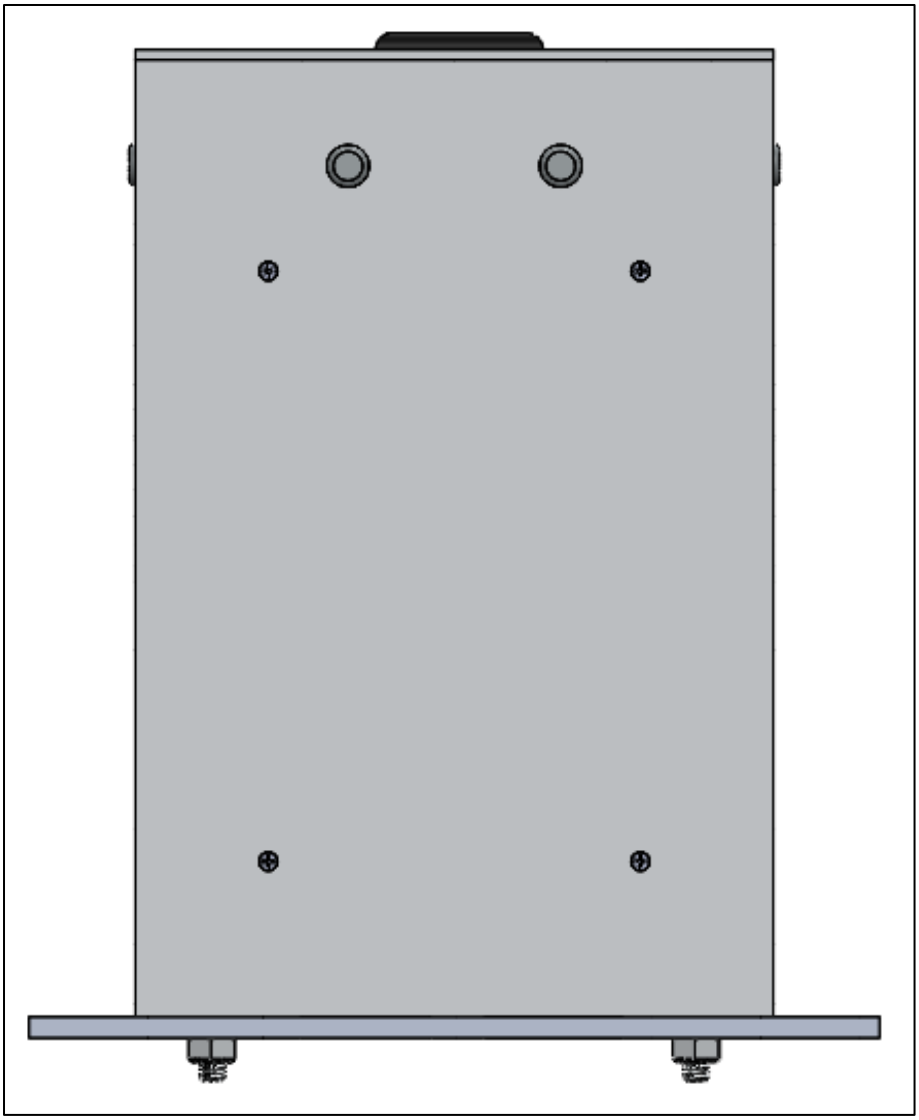

Fig. 8(h) Outer view of design of side # 4 of the payload

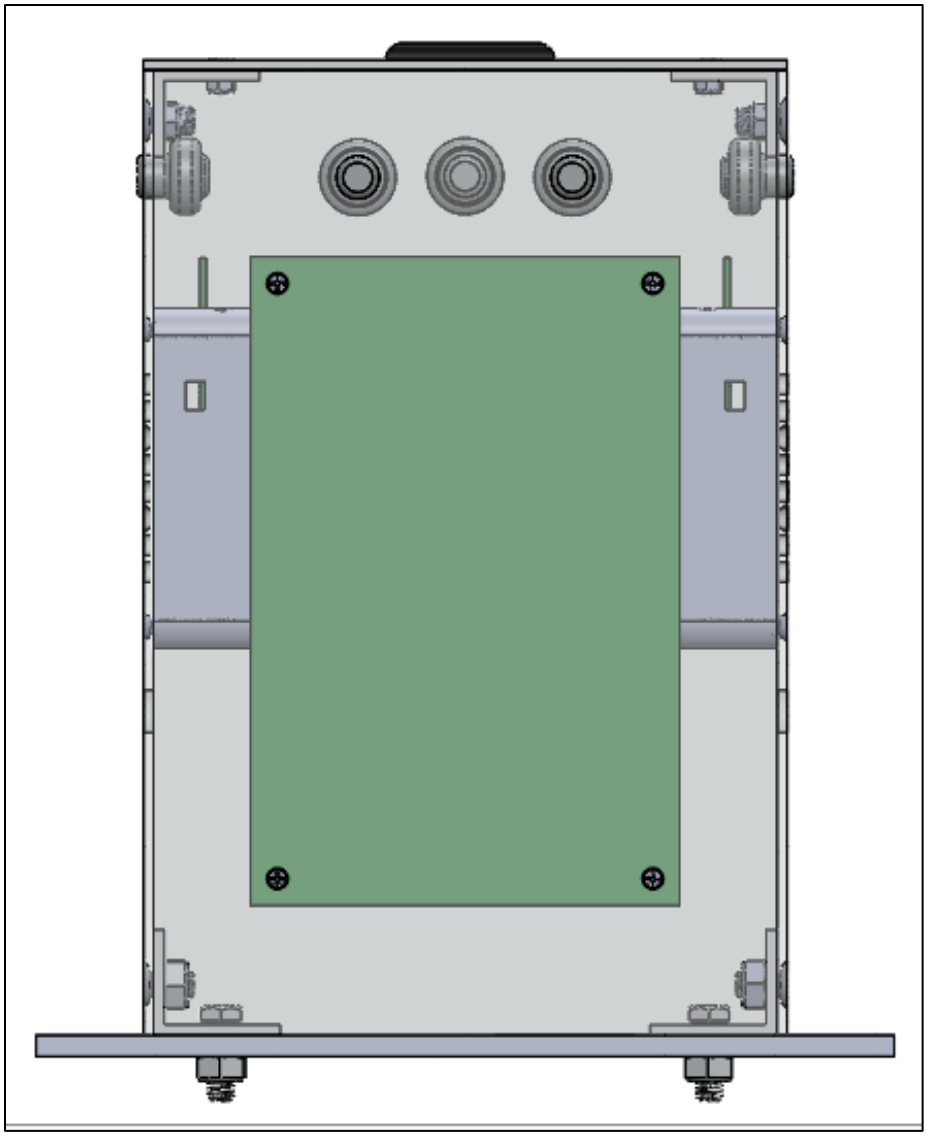

Fig. 8(i) Inside view of design of side # 4 of the payload

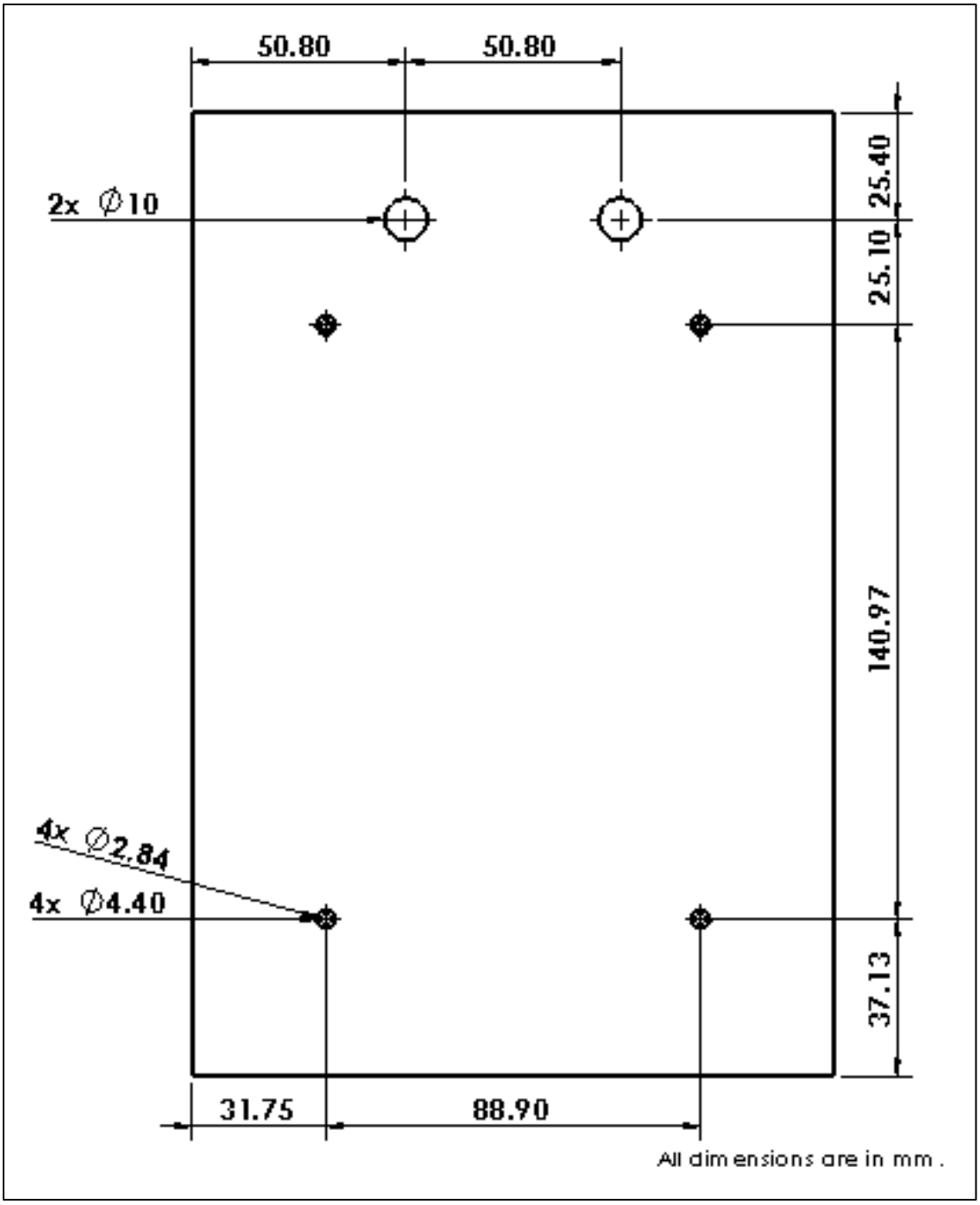

Fig. 8(j) Design with dimensions of side # 4 of the payload

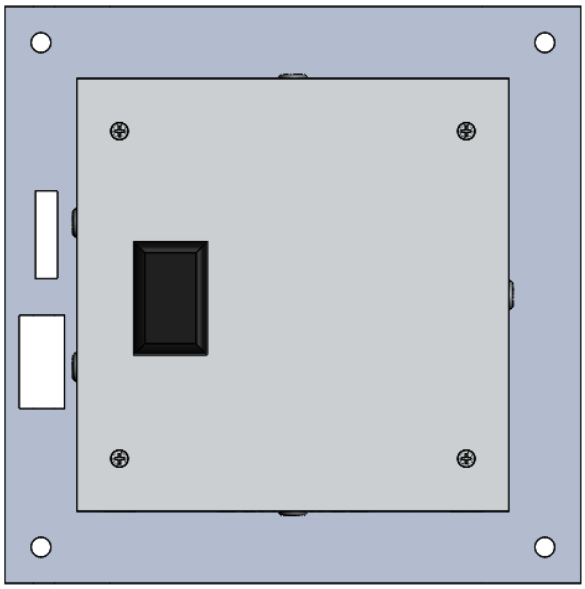

Fig. 8 (k) Design of top plate of the payload

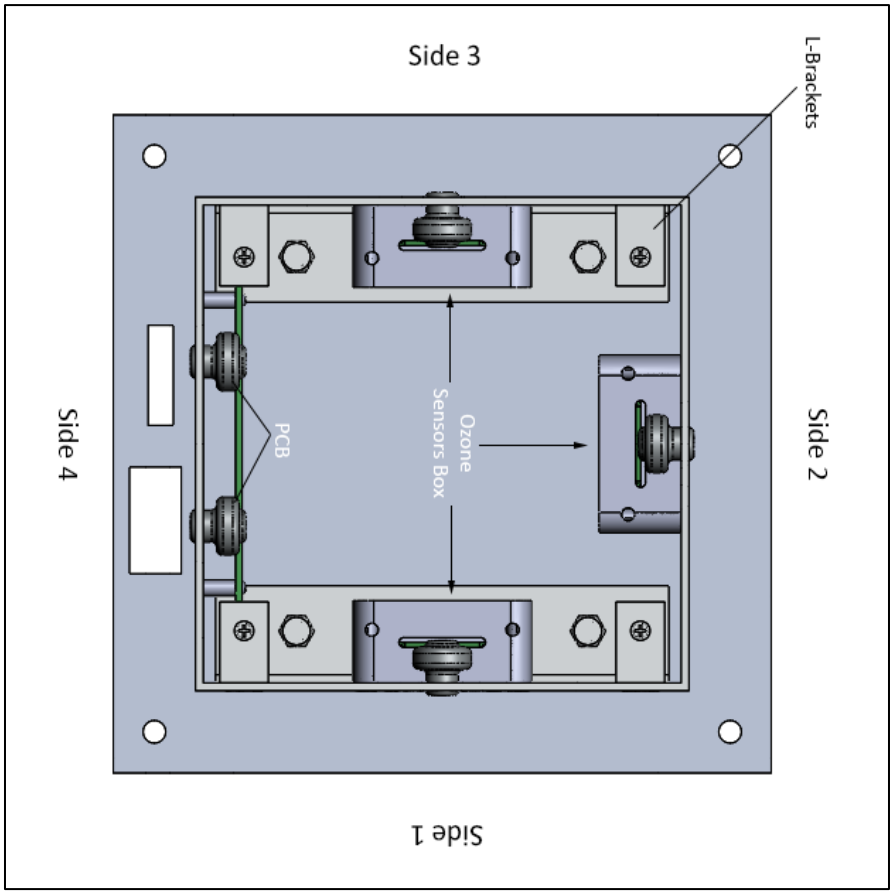

Fig. 8 (l) Top inside view of the payload

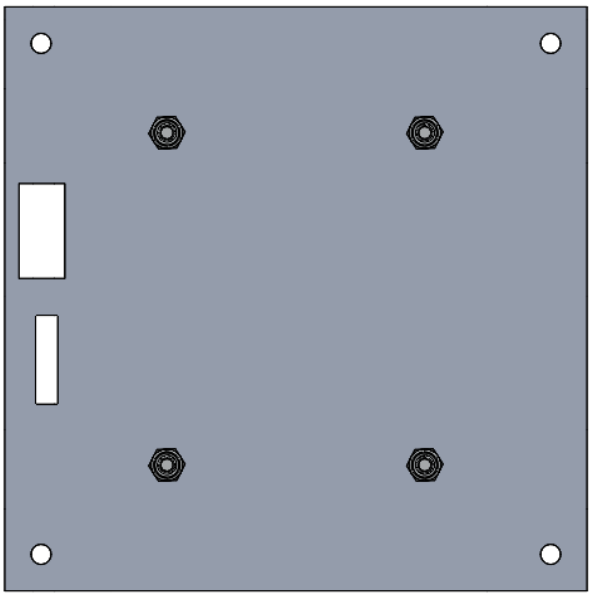

Fig. 8 (m) Bottom outer view of the payload

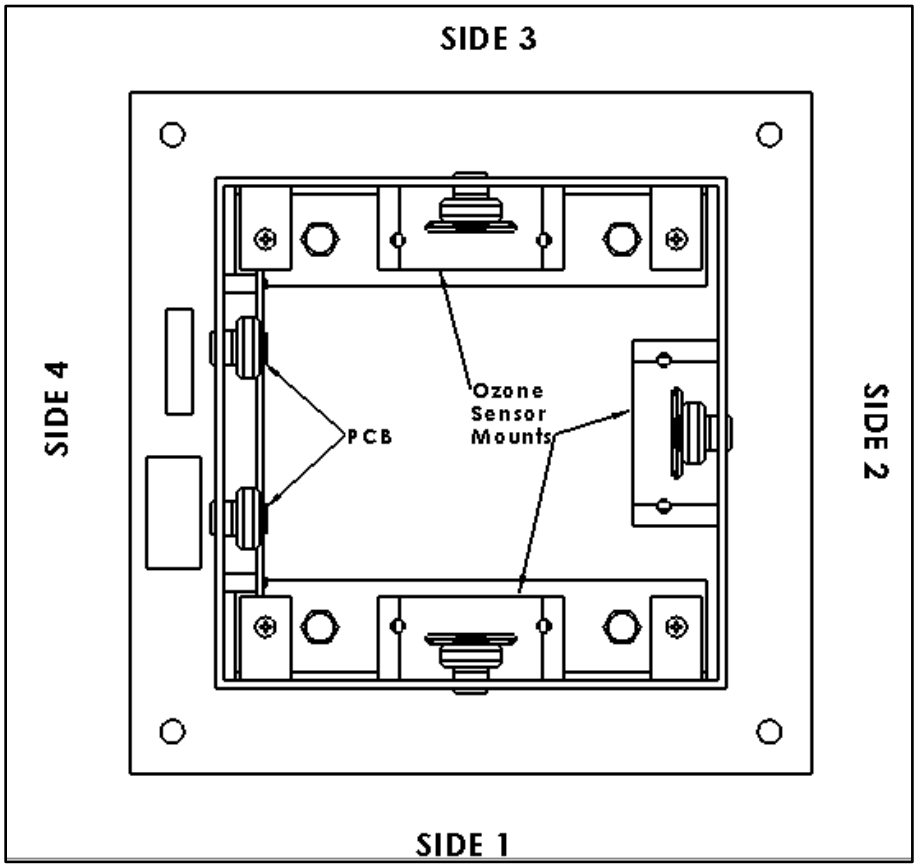

Fig .8 (l) Bottom inside view of the payload

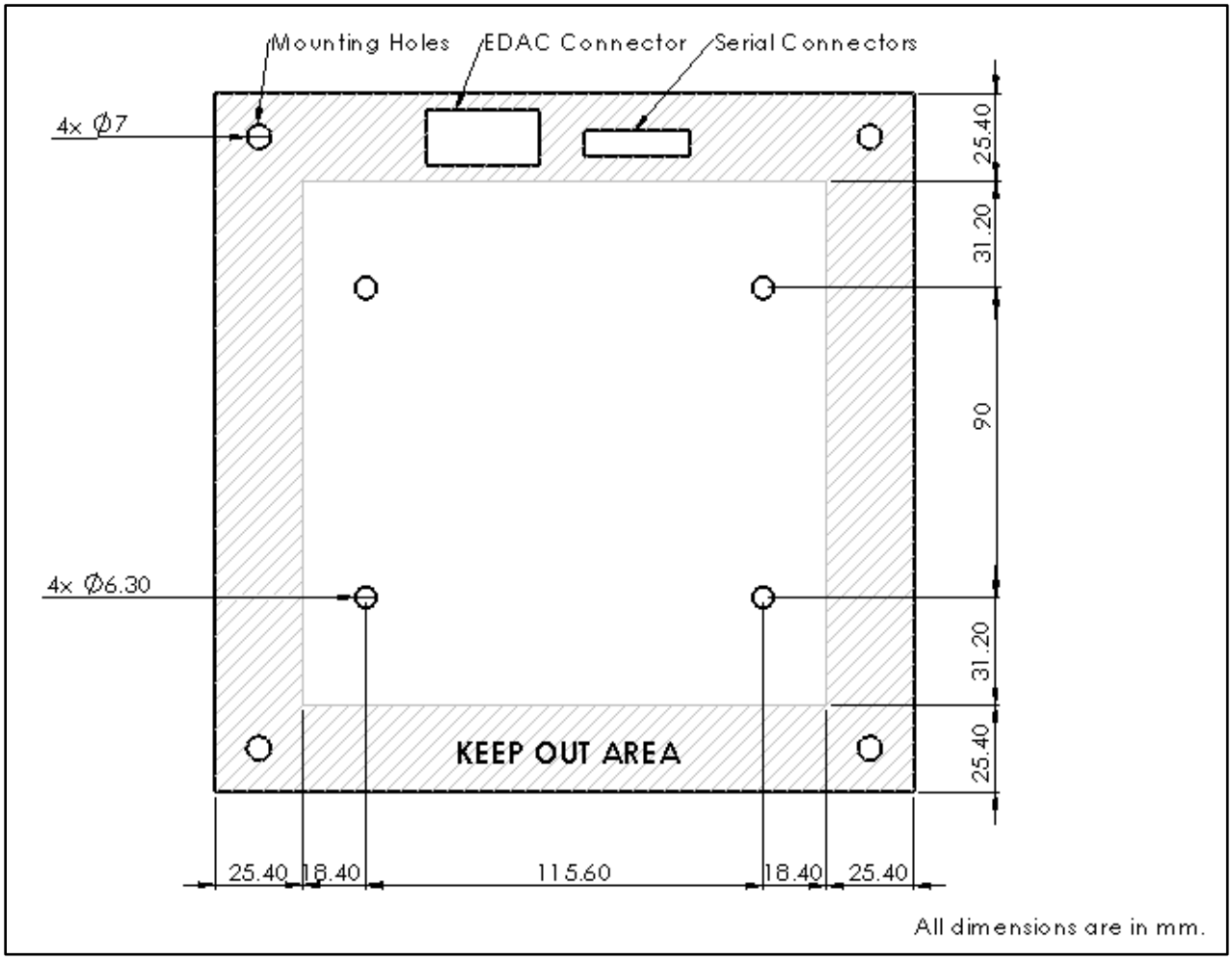

Fig. 8 (m) Design of HASP mounting plate

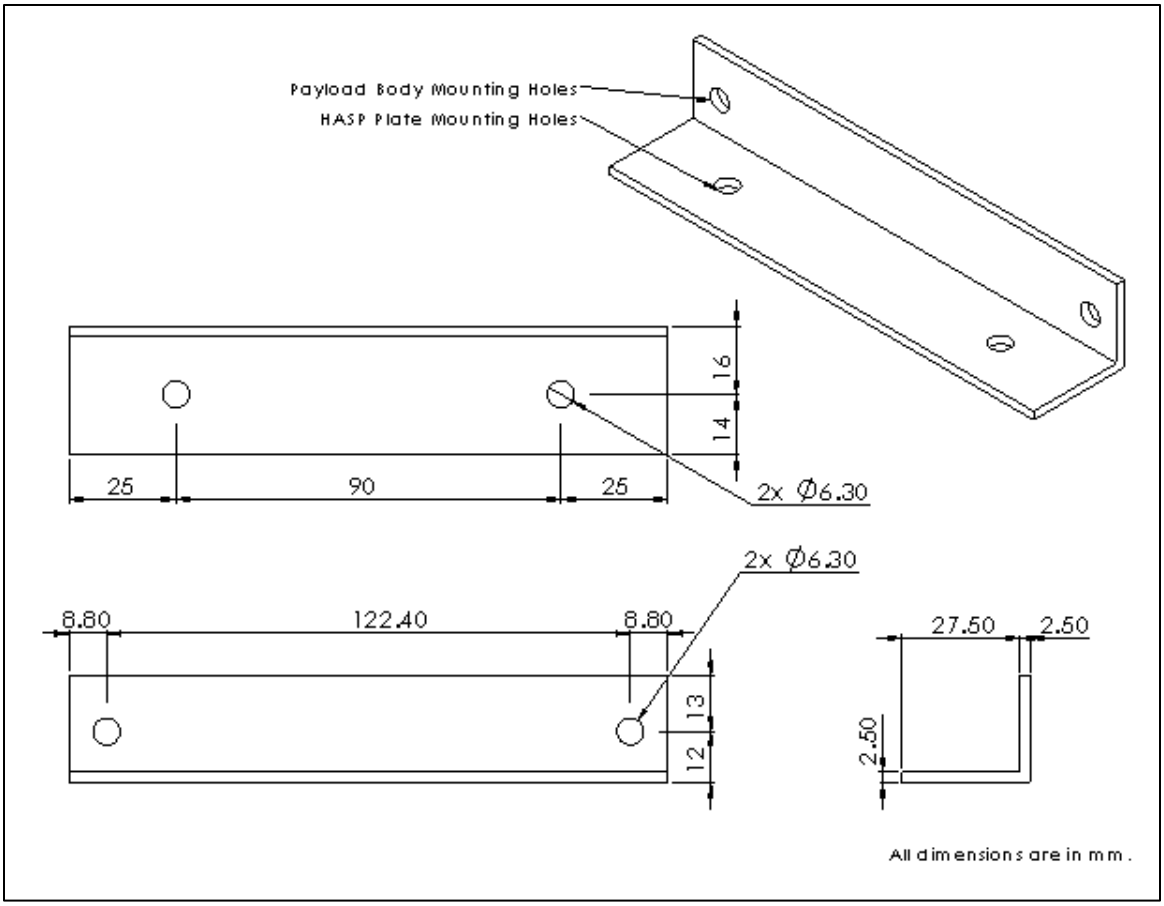

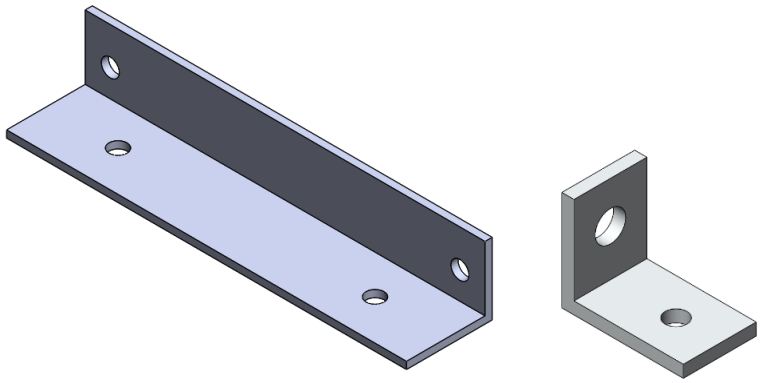

Fig. 8 (n) Design of L-Strip for mounting the HASP plate with payload body and Design of L-Brackets for mounting the top lid on the payload body

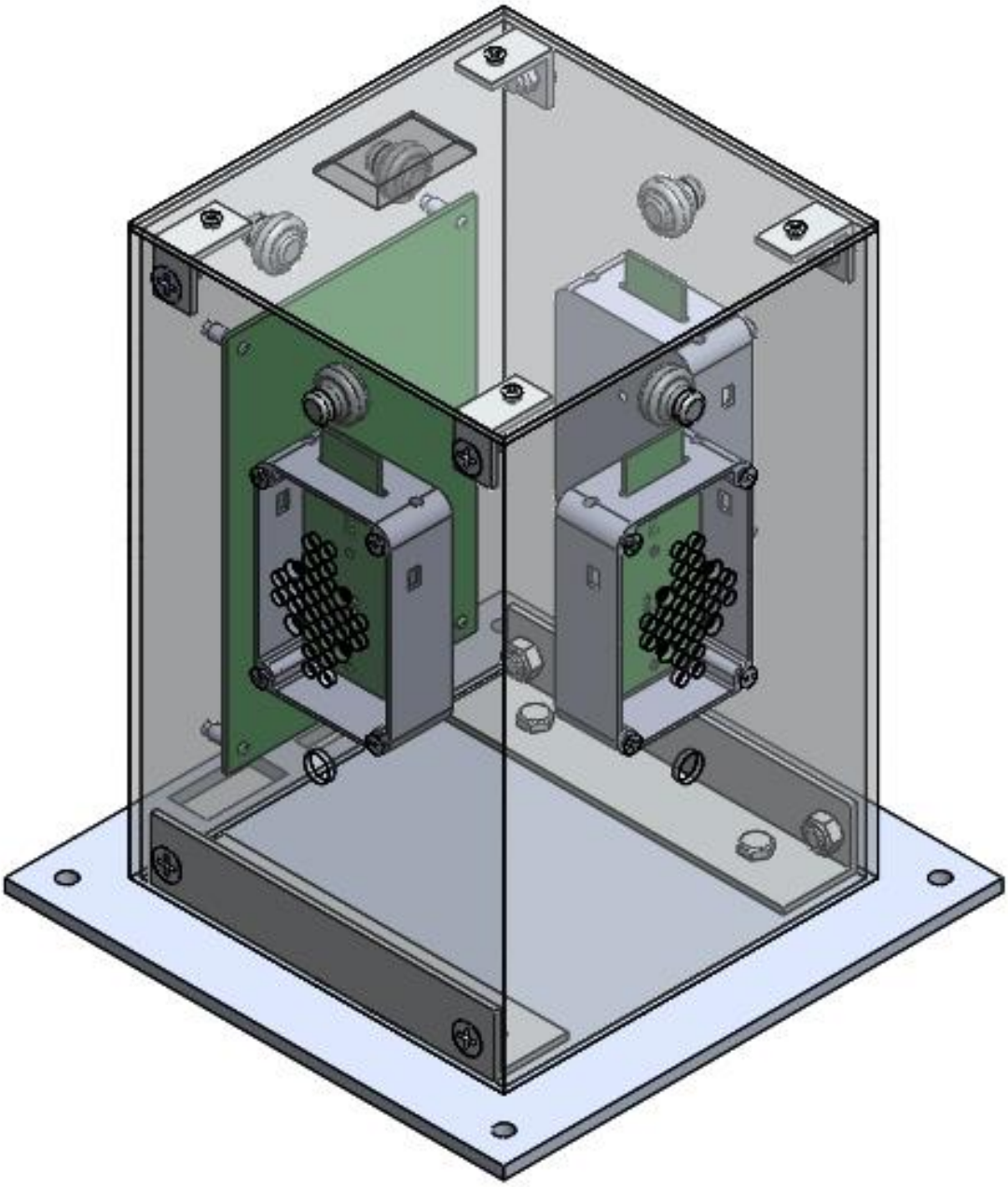

Fig. 8 (o) Design of all sides view of the payload mounted on the HASP plate.

The payload was mounted on the HASP mounting plate using aluminum L-brackets, bolts, washers and nuts.

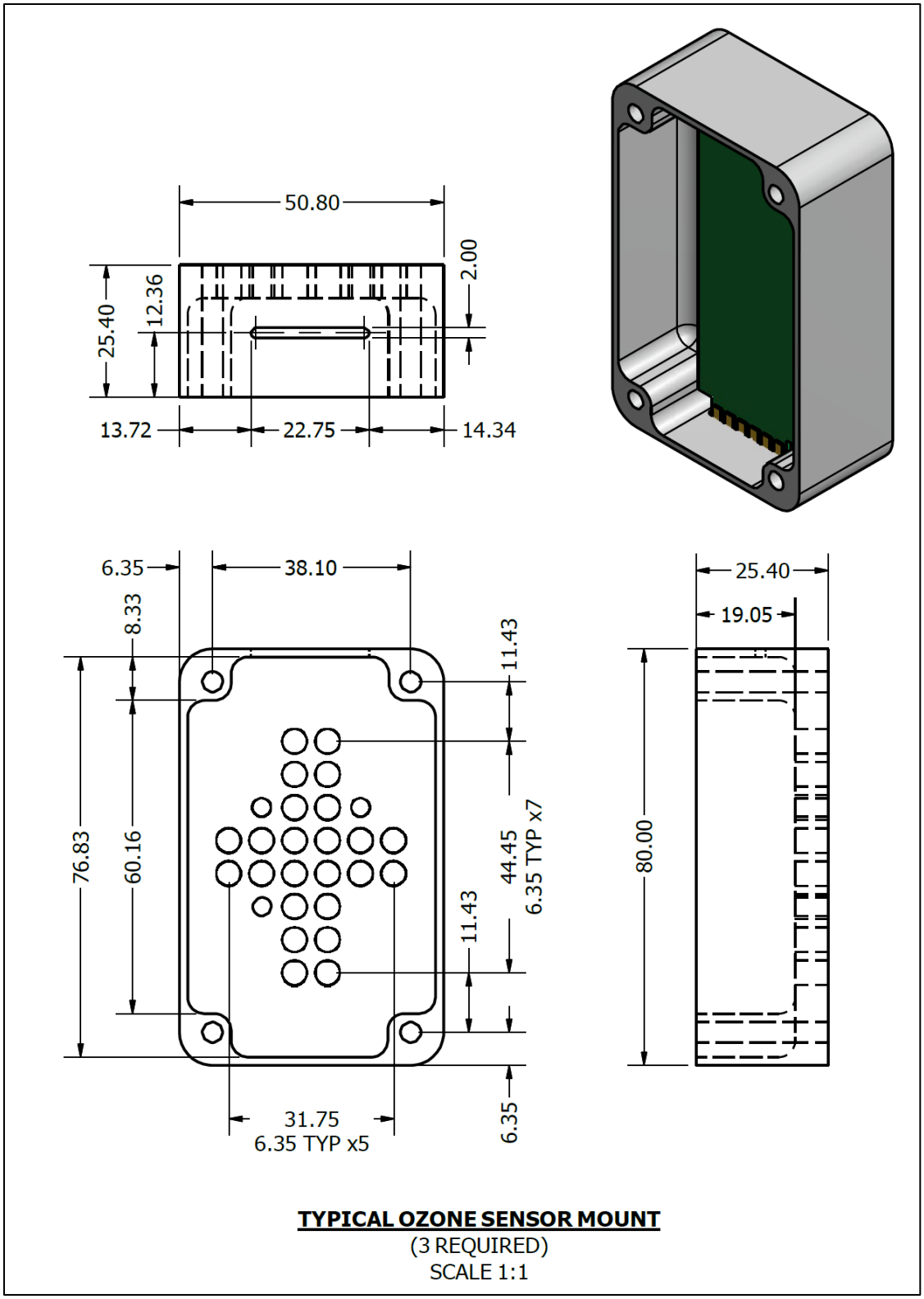

Fig.8 (p) Design of sensor box of the payload
All dimensions are in mm.

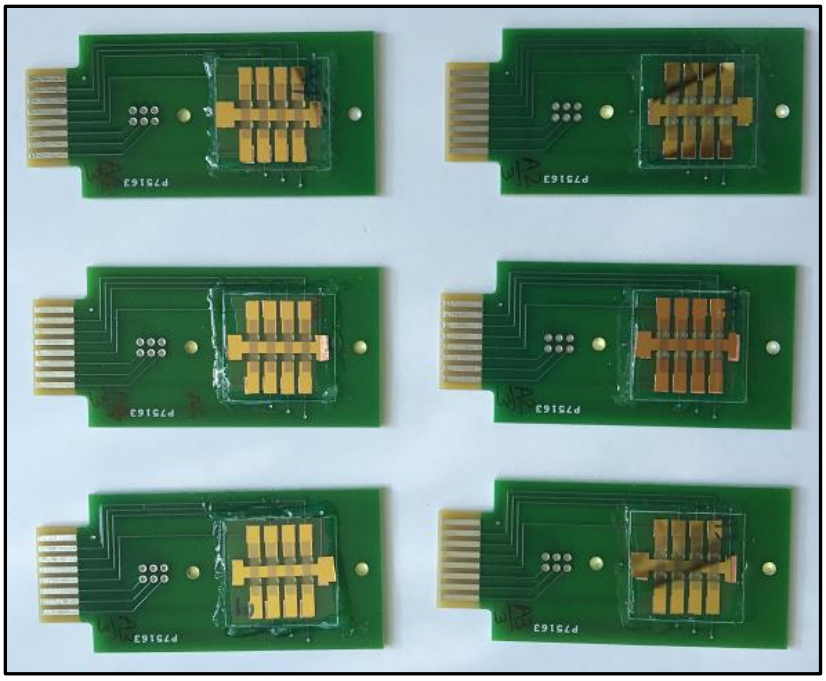

Fig.8 (q) Ozone gas sensor arrays mounted on the PCB

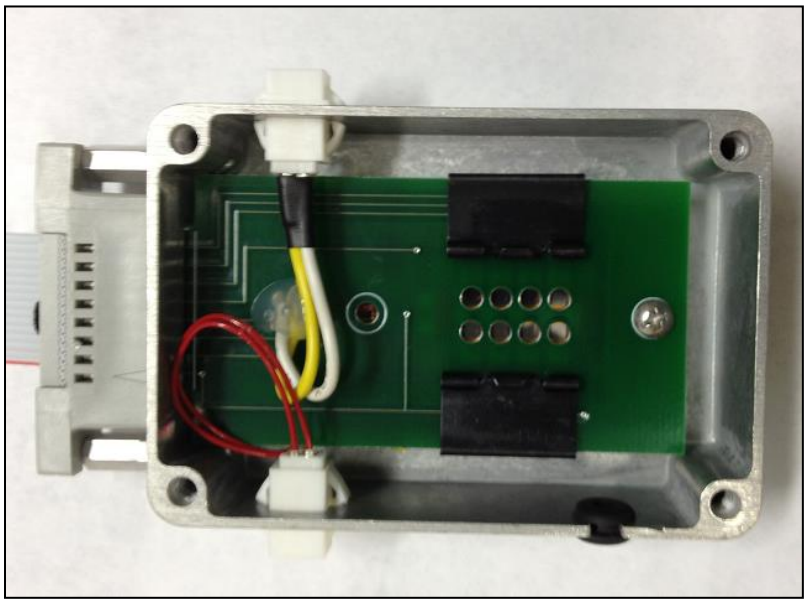

Fig.8 (r) the picture of sensors box of the payload. The sensor box consists of 8 ozone sensors array mounted on the PCB with one heater, miniature fan and a temperature sensor.

Table-1 shows the parts for the payload body from supplier www.onlinemetals.com.

Table-1 Metal parts for the payload body

Name	Size	Purpose
Aluminum Extruded Square Tube Part #6063-T52	height 9” w x d: 6” x6” wall thickness: 0.125”	Payload body
Aluminum Sheet Part#3003-H14	6” X 6” Thickness:1/8”	Top lid

Table-2 shows weight budget of various parts of the payload. The estimated total mass of payload including its base plate was 2.75 kg, which was less than the limit of 3.00 kg + 0.50 kg mass of base plate (total 3.5 kg)

Table-2. The estimated weight budget of the payload.

Item	Dimension	Mass (g)
8 Ozone sensors box #1 (including fan, heater, box)	Each box 3 x 2 x 1 inch =76.2x50.8x25.4 mm	200.0±2.0
8 Ozone sensors box #2 (including fan, heater, box)		200.0±2.0
8 Pollutant sensors box#3 (including fan, heater, box)		200.0±2.0
Microcontroller PCB with mounted components	4x 6 inch =101.6 x152.4 mm	300.0±1.0
Payload body, top plate and thermal blanket	9 x 6 x 6 inch =228.6x152.4x152.4 mm	1000±10.0 g
Few Cables, 1 GPS, 2 LEDs, 3 Photodiodes, nuts and bolts		300±5.0 g
HASP mounting plate	7.9 x 7.9 inch =200.6x200.6 mm	550±3.0 g
Total estimated mass of the payload with HASP mounting plate		**2750±25.0 g**

Thermal Blanket

The outer surface of payload body was covered by the thermal blanket made of silver color aluminized heat barrier having adhesive backed (Part No. 1828) (Make: www.PegasusAutoRacing.com) for the improvement of thermal stability. The high reflective surface of the material is capable of withstanding radiant temperatures in excess of 1000^{o}C. Fig. 9 shows the typical plots of % reflectance at different wavelength of light from the silver, gold, copper and aluminum surfaces. Silver color surface higher reflectance over wide range of wavelength of light compare to gold, copper, and aluminum surfaces.

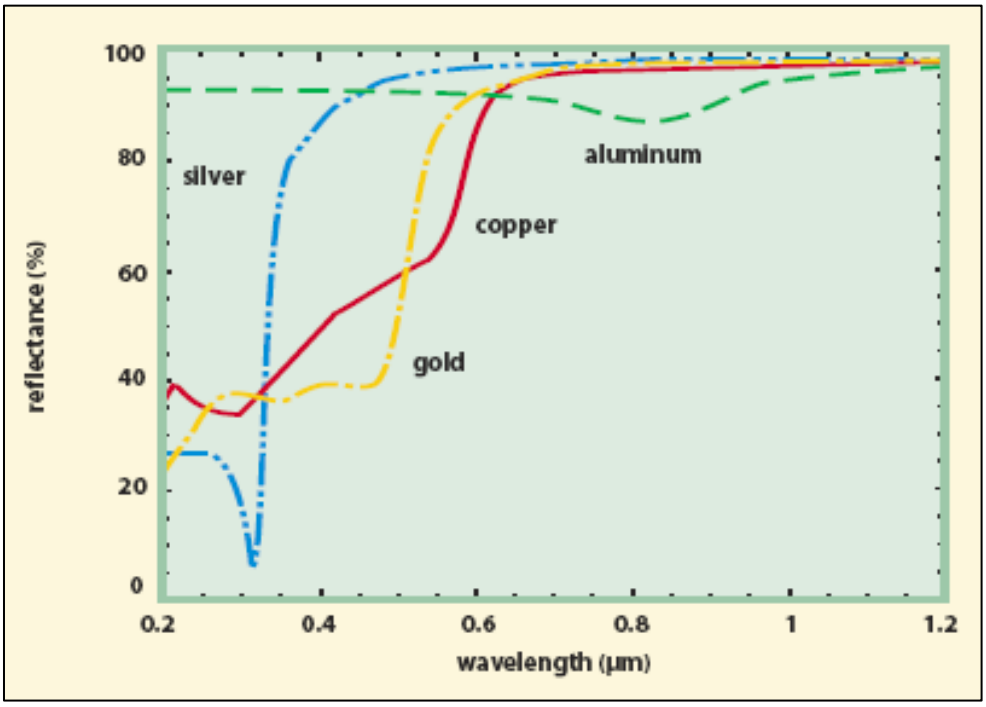

Fig.9. Variation of reflectance with wavelength of light from different color of surfaces. Courtesy: http://www.photonics.com/EDU/Handbook.aspx?AID=25501

6. Electronic Cirucits

The block diagram of circuit is shown in fig. 10 (a), while several sections of circuits are shown in fig. 10 (b) to (h). Two identical microcontroller PCBs were fabricated. The picture of PCB is shown in fig.10 (i). Two identical PCBs were fabricated. One PCB was used for the payload, while for other PCB was used to stimulate software and backup. The original design was made earlier by Jonathan Wade.

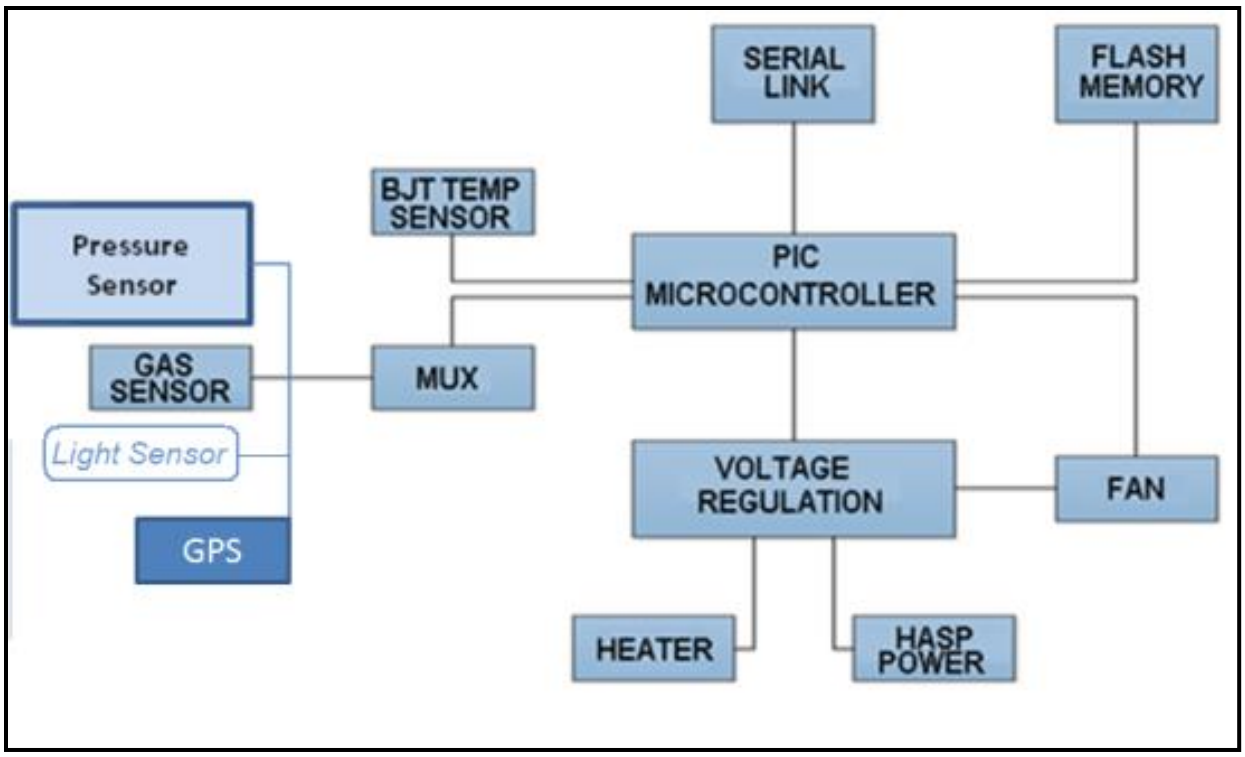

Fig. 10(a) Block diagram of payload ciruct

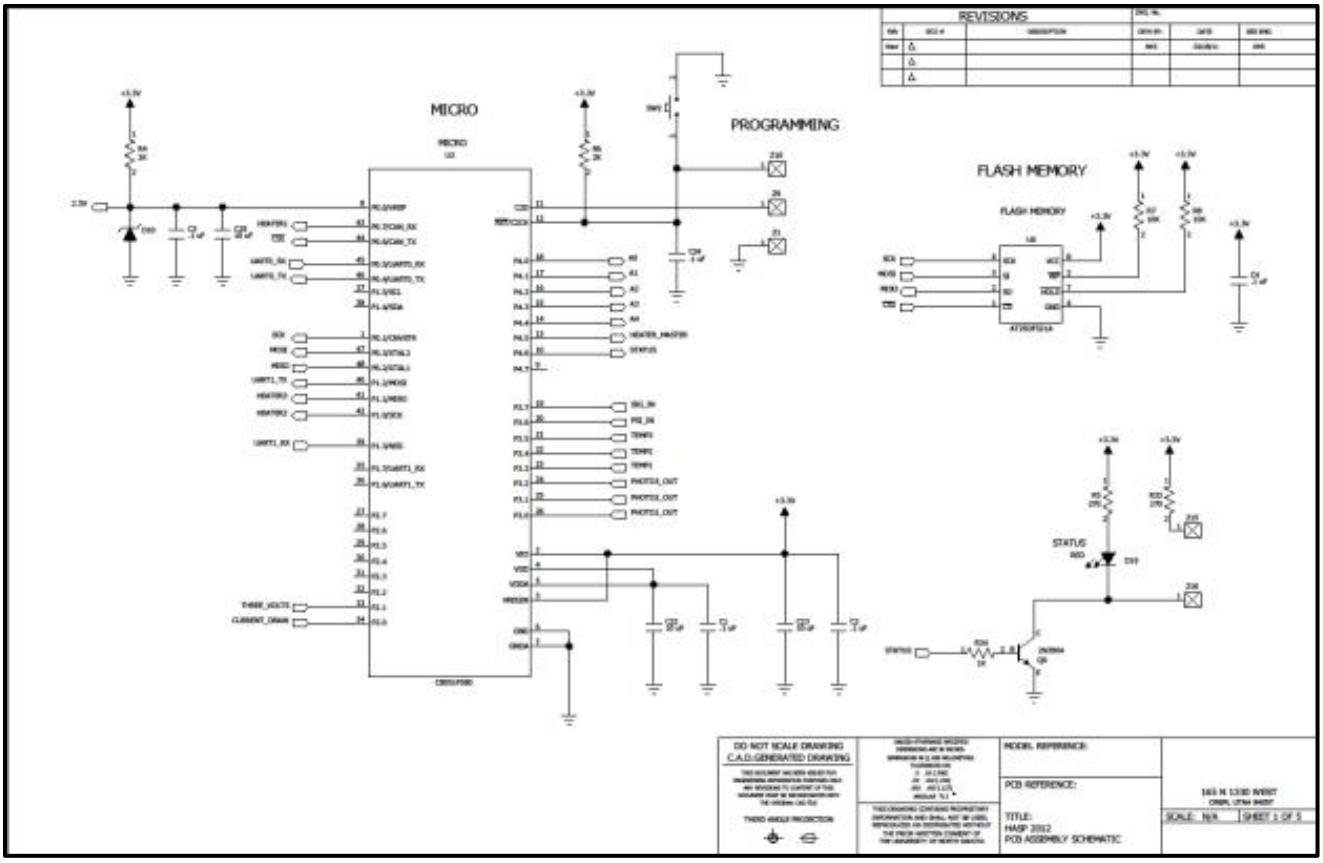

Fig. 10 (b) Circuit for microcontroller and flash memory

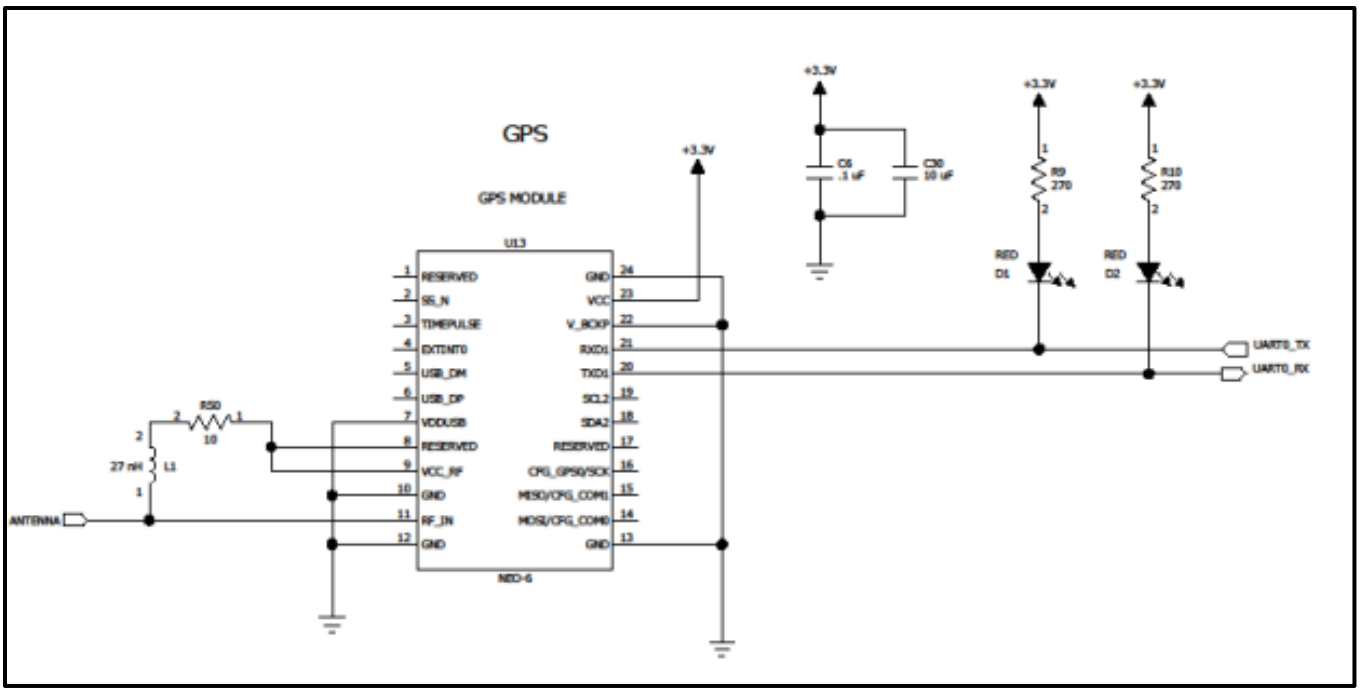

Fig. 10 (c) Circuit for GPS

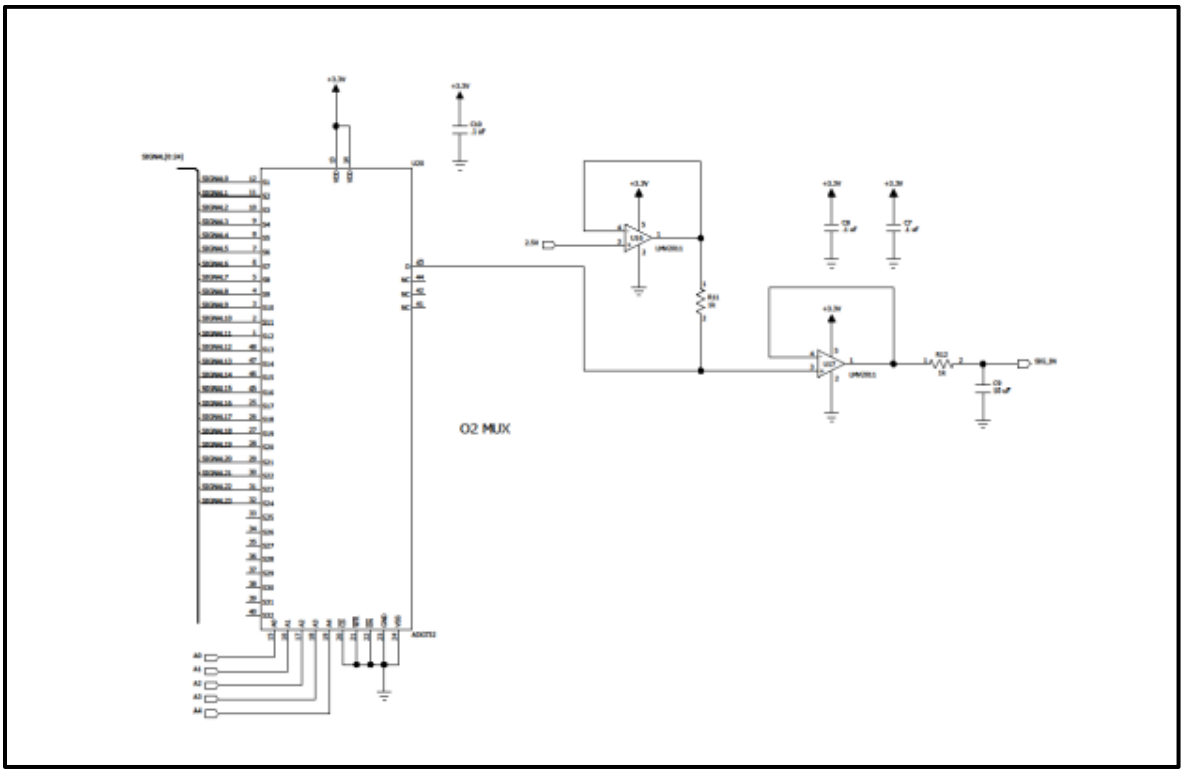

Fig. 10 (d) Multiplexer circuit

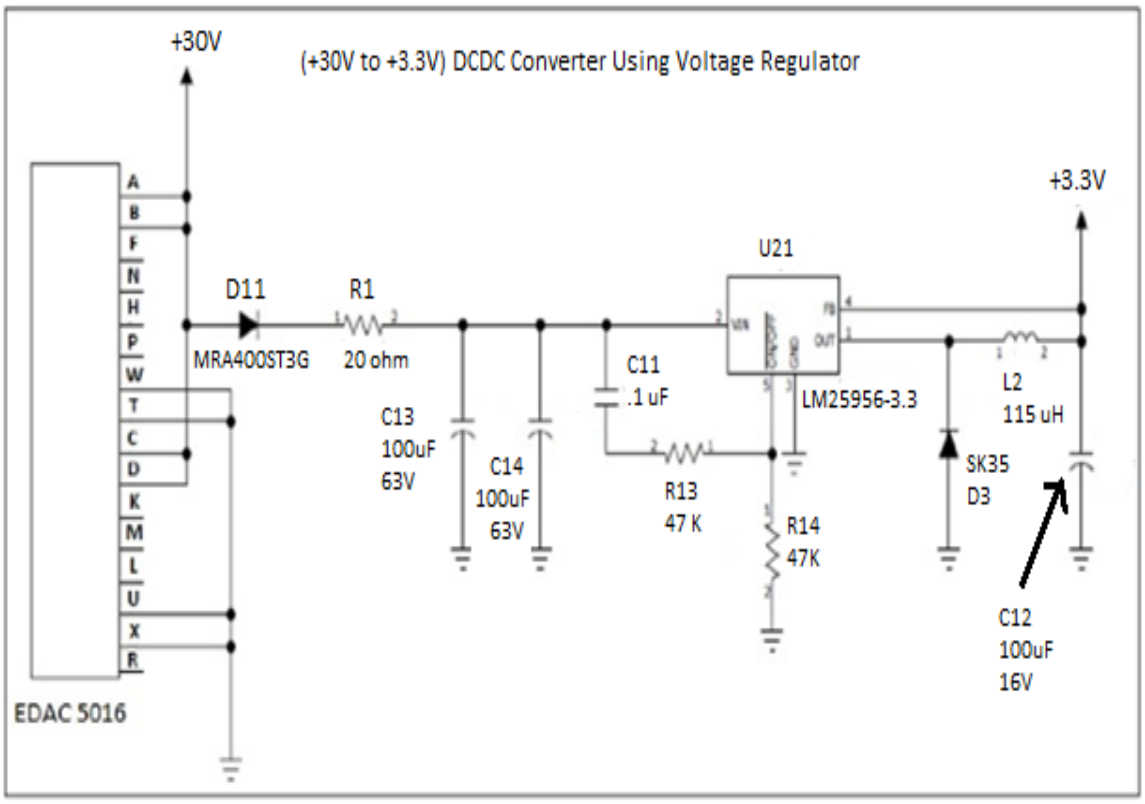

Fig. 10 (e) Voltage regulation circuit

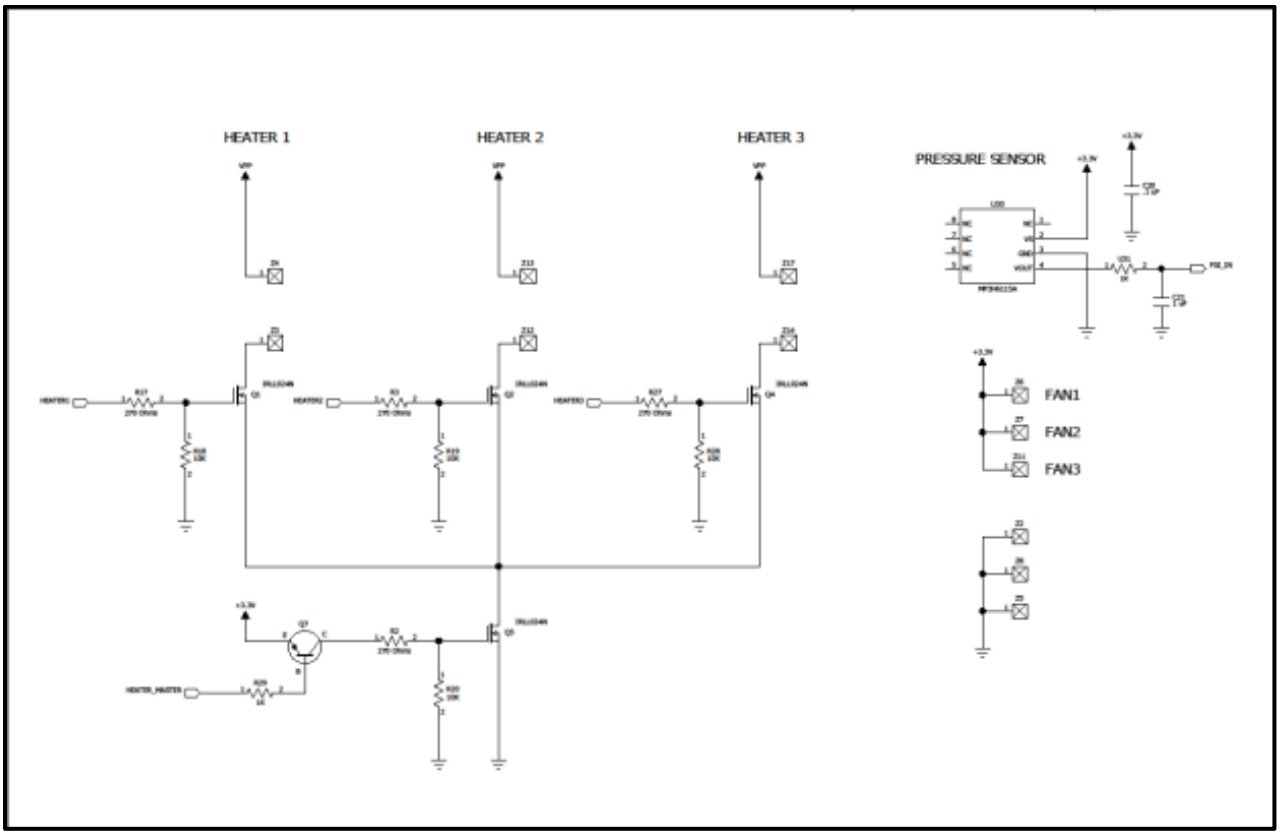

Fig. 10 (f) Circuit for three heaters, three fans and pressure sensor

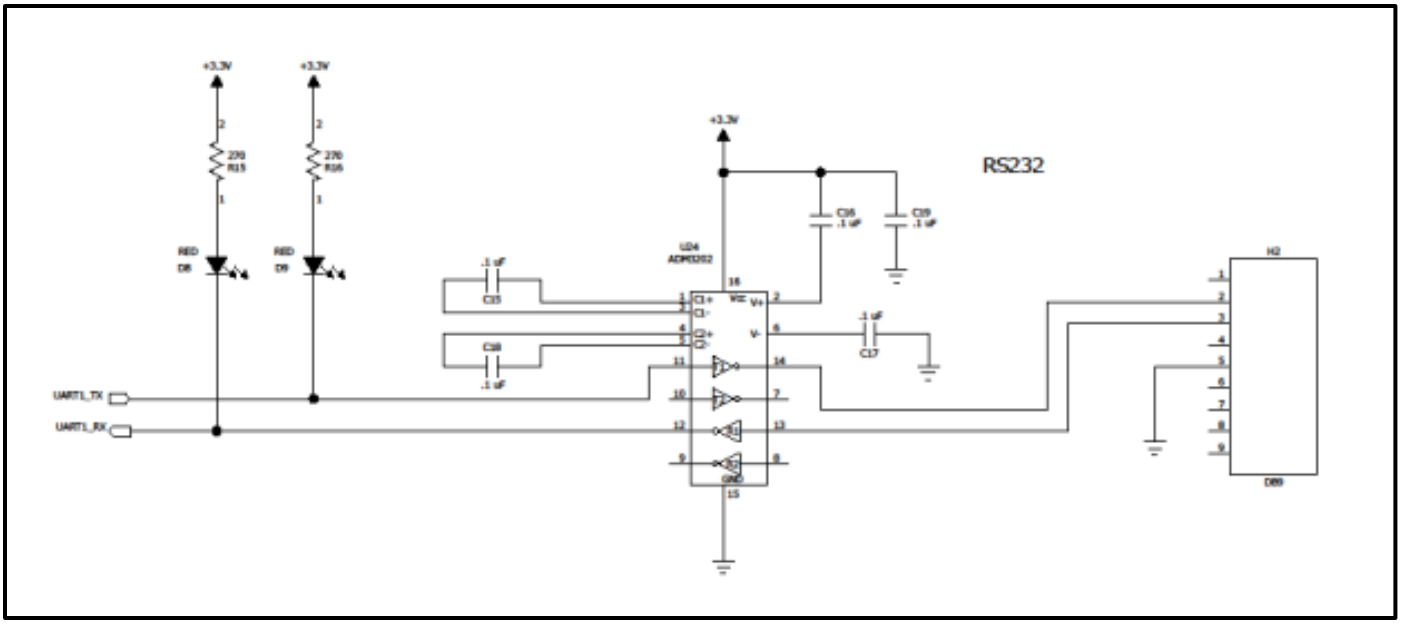

Fig.10 (g) Circuit for RS232

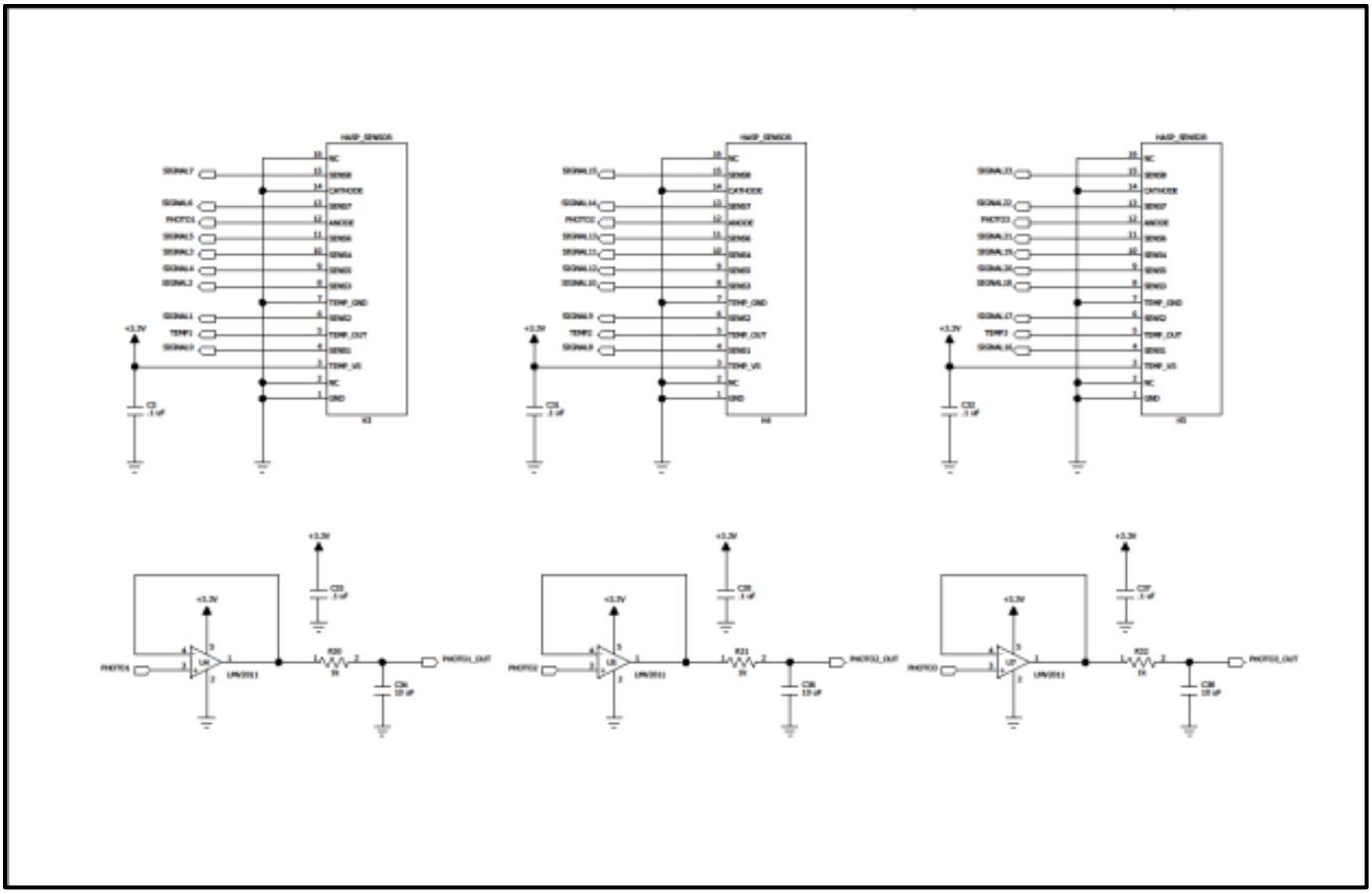

Fig.10 (h) Circuit for three ozone sensors boxes and three photo (light) sensors

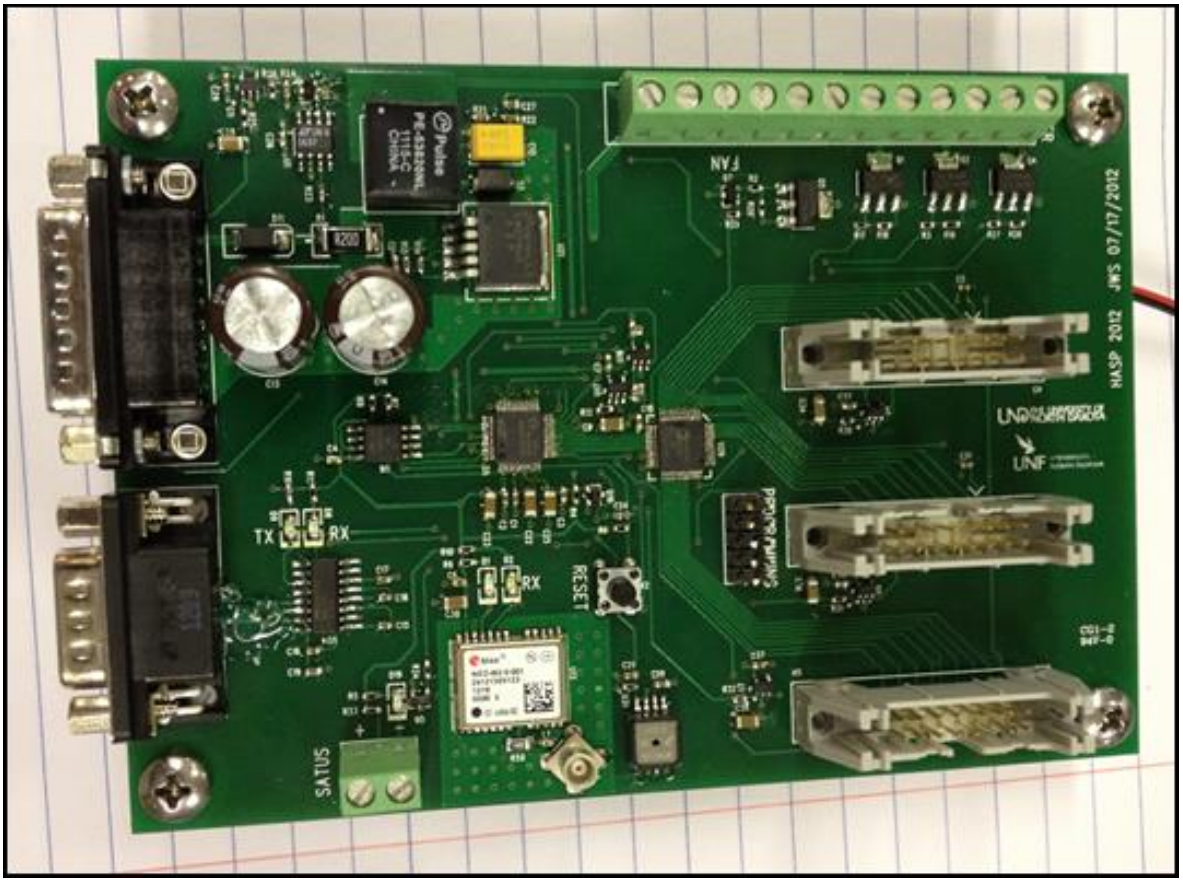

Fig. 10 (i) Picture of microcontroller PCBs

Predicted Power Budget

The expected current and power drawn by the payload at 3.3 applied voltage are given in the following table 3 (a).

Table-3(a) Power budget of the payload

Circuit Function	Current Draw (mA) at 3.3 V	Power (W) draw at 3.3 V
Payload Power ON, ALL heaters OFF	30± 5	0.099±0.017
Payload Power ON, ONE heater ON	140± 5	0.462±0.017
Payload Power ON, TWO heaters ON	250± 5	0.825±0.017
Payload Power ON, Three heaters ON	360± 5	1.2±0.017

The minimum power drawn by the payload will be about 0.099 ±0.017 W, while maximum power drawn will be about 1.2±0.017 W. Most of time power drawn by the payload during the float will be less than 1.0 W.

7. Integration of Payload and Thermal Vacuum Test

The ozone sensors payload was fabricated, assembled and tested at Dr. Patel's lab. Dr. Nirmal Patel (Faculty), Joseph Ward and Trevor Roger from University of North Florida were participated the HASP 2019 integration workshop at the NASA-CSBF, Palestine, TX (fig.11 (a)) during July 14 to 19, 2019.

Fig. 11(a) Trevor Roger, Joseph Ward and Dr. Nirmal Patel at NASA-CSBF, Palestine, TX

The payload was initially tested by Mr. Anthony Ficklin and Mr. Joshua Collins and then by Mr. Dough Granger and Dr. Greg Guzik.

Fig.11 (b) shows weighing of the payload using the digital balance. The total mass of payload including its HASP base plate was 2.760 kg, which was less than the limit of 3.00 kg + 0.50 kg mass of the HASP base plate (total 3.5 kg).

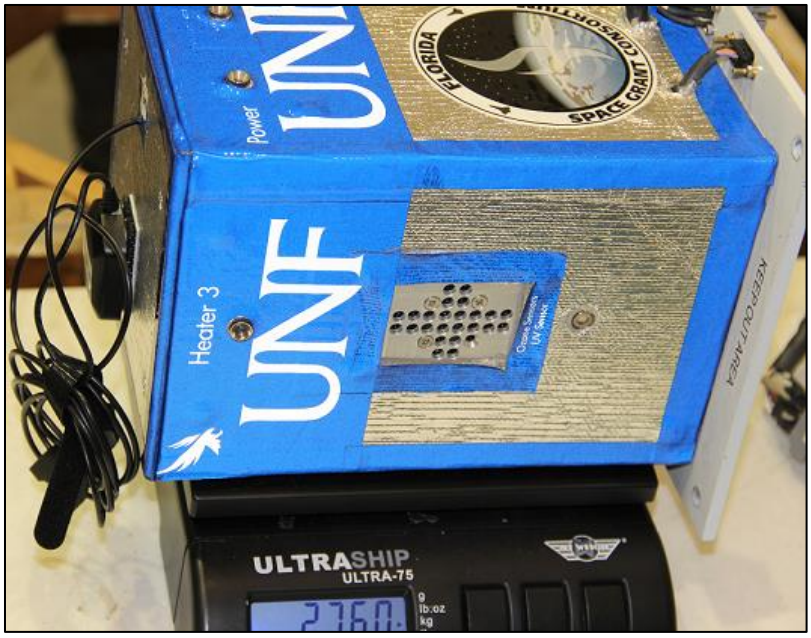

Fig.11 (b) weighing of the payload

The measured current draw at 30 VDC was measured about 70 mA nomal running (all three heaters OFF) and 390 mA maximum (all threeheaters ON) at full load. The current limit was tested for determination of value of a saftey fuse. Fig. 12 (a) shows testing of current by Anthony and Joshua (HASP-LSU), integration of payload with HASP (Fig. 12(b)) and then tested by Dr. Guzik (HASP_LSU)(Fig. 12(c)).

Fig.12 (a) shows Anthony and Joshua are testing of maximum current drawn by the UNF payload.

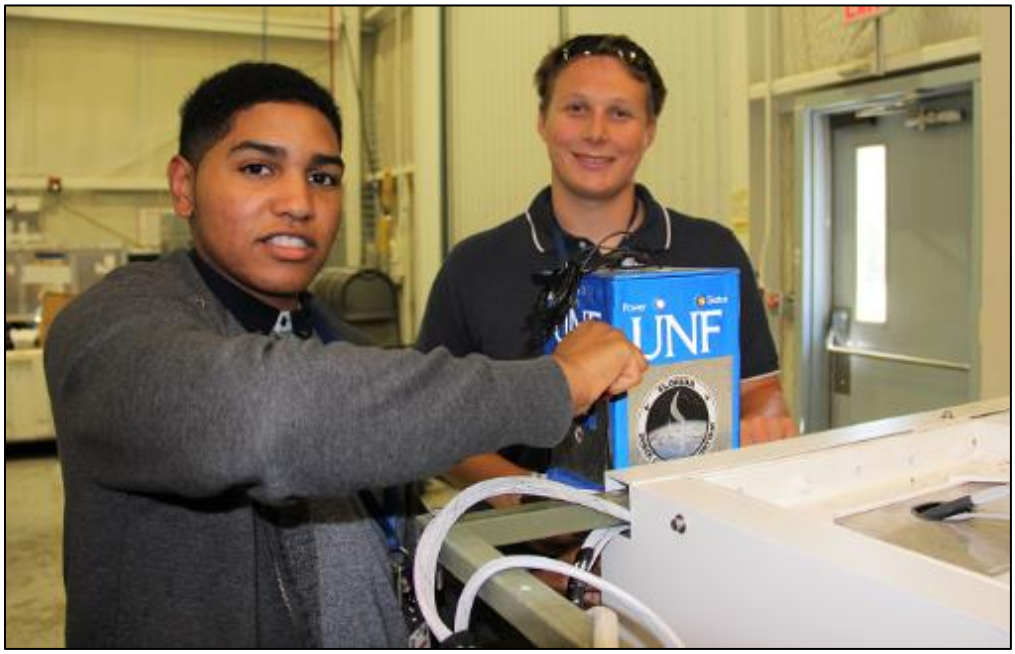

Fig.12 (b) Integration of payload with HASP by Joseph and Trevor

Fig.12 (c) shows Dr. Guzik during testing of UNF payload.

The payload was tested in the BEMCO chamber, which is shown in Fig. 13(a) for high temperature (about 55 ^{o}C), low temperature about (-50 ^{o}C), high pressure (about 950 mbar), and low pressure (about 5 mbar). Fig. 13(b) shows the picture of participants of various teams, Fig.3(c) shows UNF team members during the thermal vacuum test and fig 13(c and d) shows pictures of UNF team with the payload during thermal vacuum testing. The payload successfully cleared all required thermal vacuum test and got the HASP Payload Integration Certification for the HASP balloon flight 2019.

Fig. 13 (b) HASP 2019 Participants from various teams.

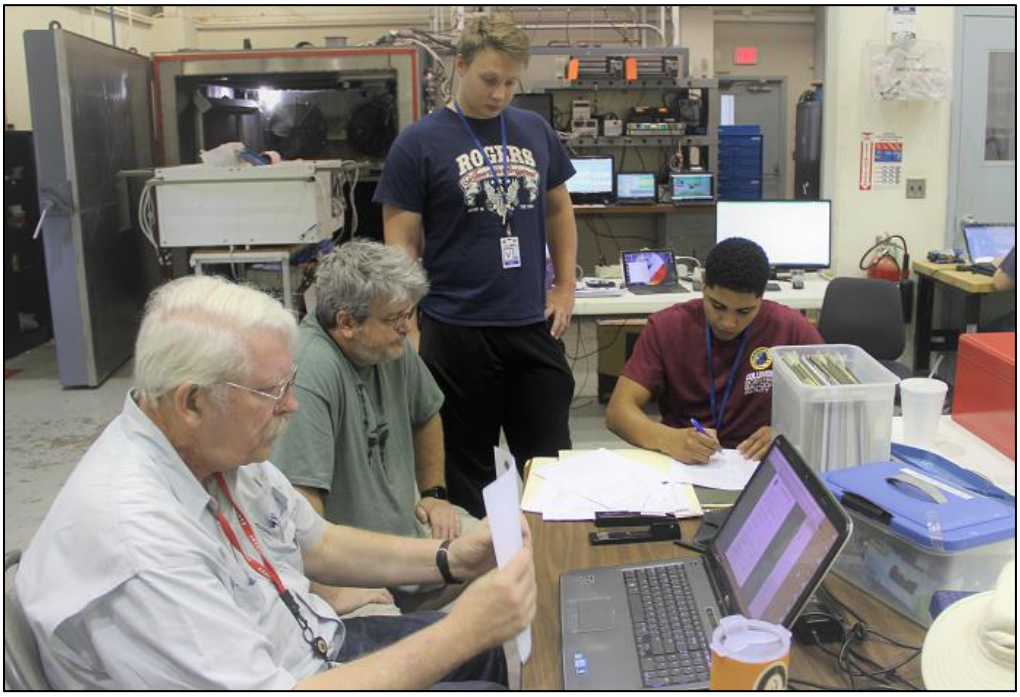

Fig. 13 (d) Dr. Guzik, Dough, Trevor and Joseph (from Left to right) finalizing the paper work for the HASP payload certification for the UNF payload after successful thermal vacuum test.

During the thermal vacuum test, all sensors data, pressure transducer, UV light sensors, temperature on sensors, heaters, GPS, data communication and uplink commands were tested and verified several times. The payload was certified for the HASP 2019 balloon flight after successful completion of the thermal vacuum test.

Fig.14 shows the variation of voltage with time during thermal vacuum test. The voltage level was nearly constant during test period. It was found that the average voltage level was 3329.0 mV with standard deviation of 27.0 mV.

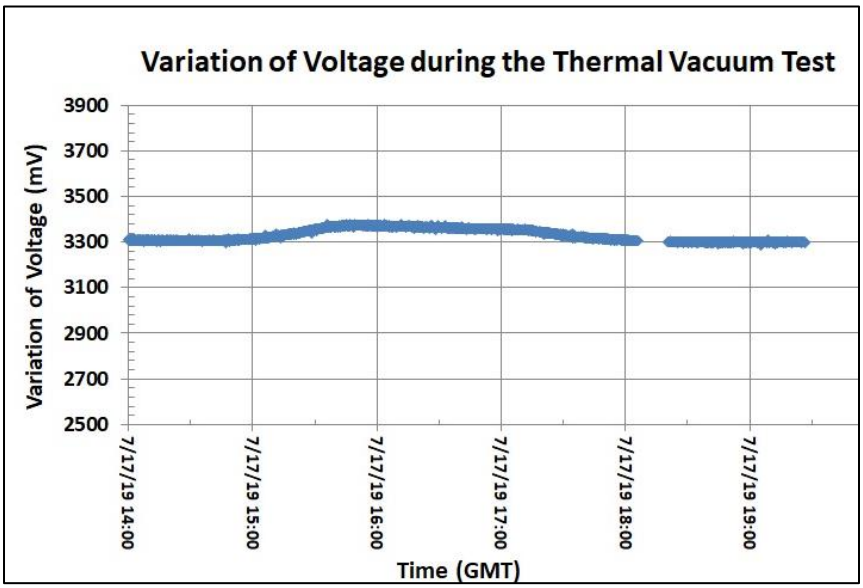

Fig.14 Variation of voltage applied to the payload with time

The current drawn by the payload during the thermal vacuum test is shown in fig. 15 (a). Payload draw (i) 35±4 mA when all three heaters were off, (ii) about 65 ± 5 mA when heater #1 was on, (ii) about 180 ±7 mA when heaters # 1 and 2 were on, and (iv) about 340±6 mA when all the three heaters #1, 2, and 3 were on. Total time duration for all three heaters on is very small compared to one or two heaters on.

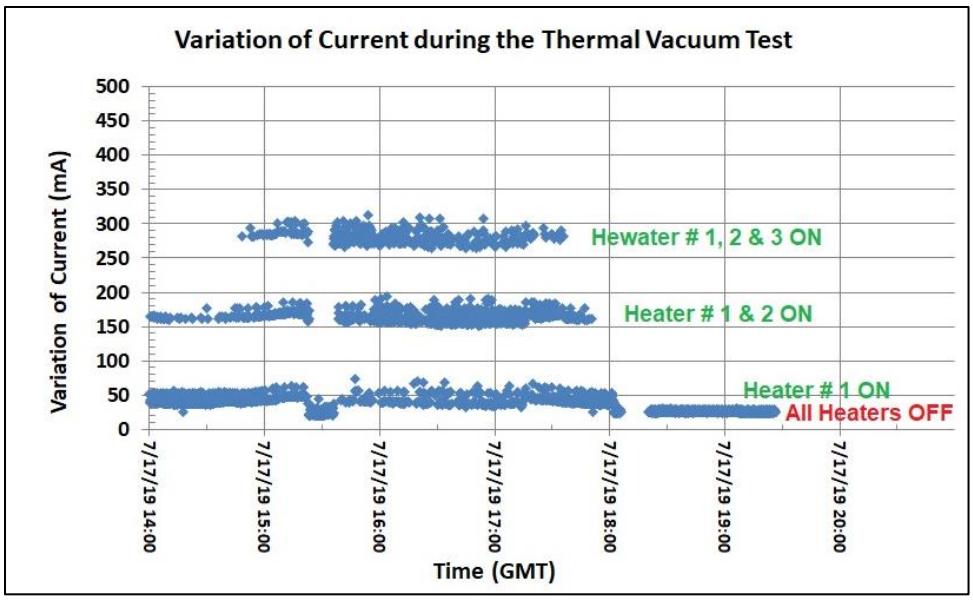

Fig.15 (a)Variation of current consumed by the payload with time.

Fig. 15(b) shows variation of voltage and current of the payload during thermal vacuum test measured by HASP (Data courtesy: Mr. Doug Granger, HASP- LSU). These data and plot for voltage and current (fig.1 5(b) are nearly match with our measured value of voltage and current (fig.14 and 15(a).

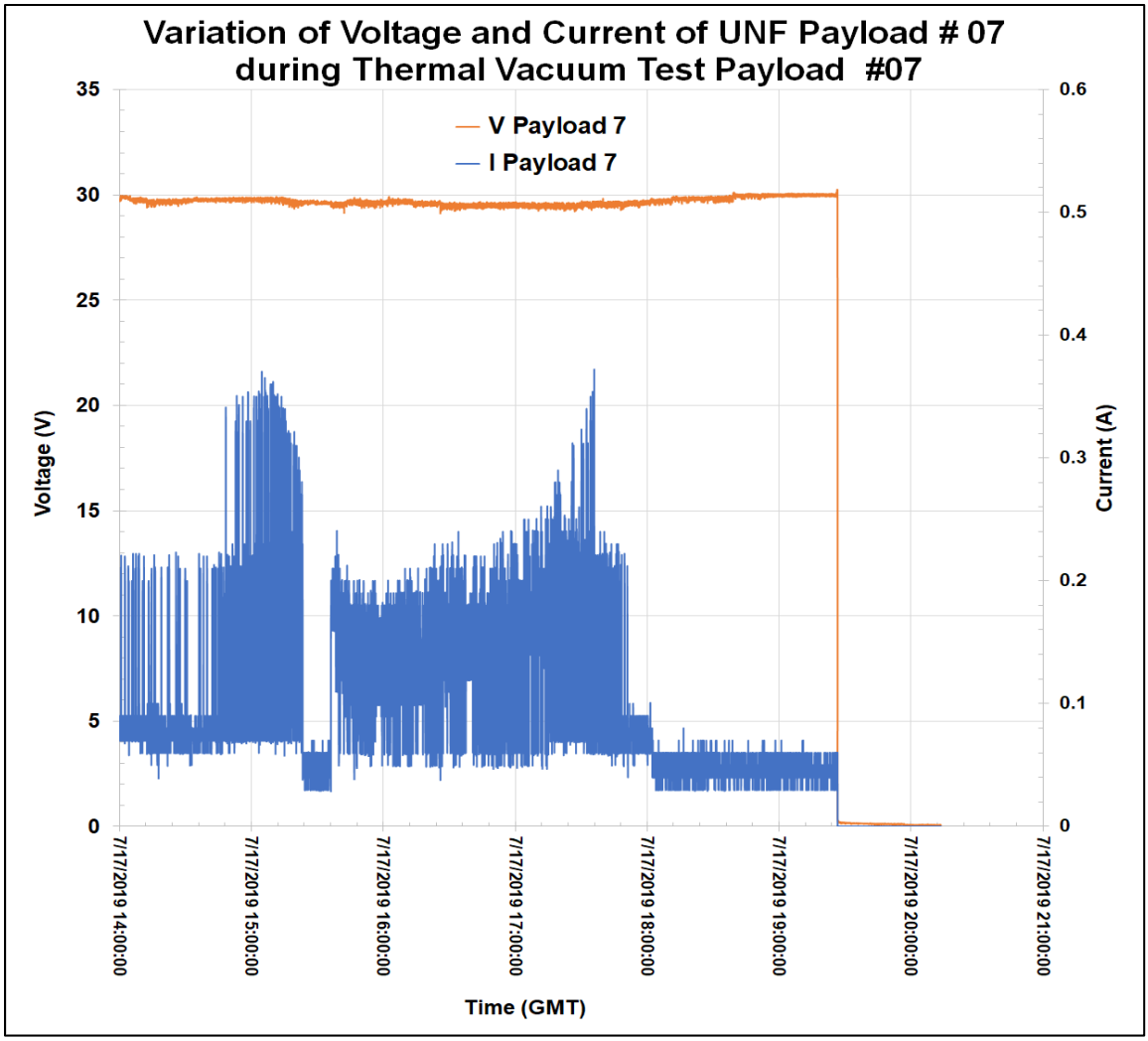

Fig. 15(b) Variation of voltage and current of the payload during thermal vacuum test measured by HASP (Data courtesy: Mr. Doug Granger, HASP- LSU).

The variation of pressure measured by the payload during the thermal vacuum test is shown in the fig. 16(a). Our pressure transducer did not measure the pressure below 100 mbar due to its technical limitation and hence saturated. The measured pressure data were nearly matched with the data measured by the HASP pressure transducer, which is shown in the fig. 16(b). In addition, fig. 16(b) also shows the variation of temperature measured on the outer surface of the payload -7 body with time during the thermal vacuum test.

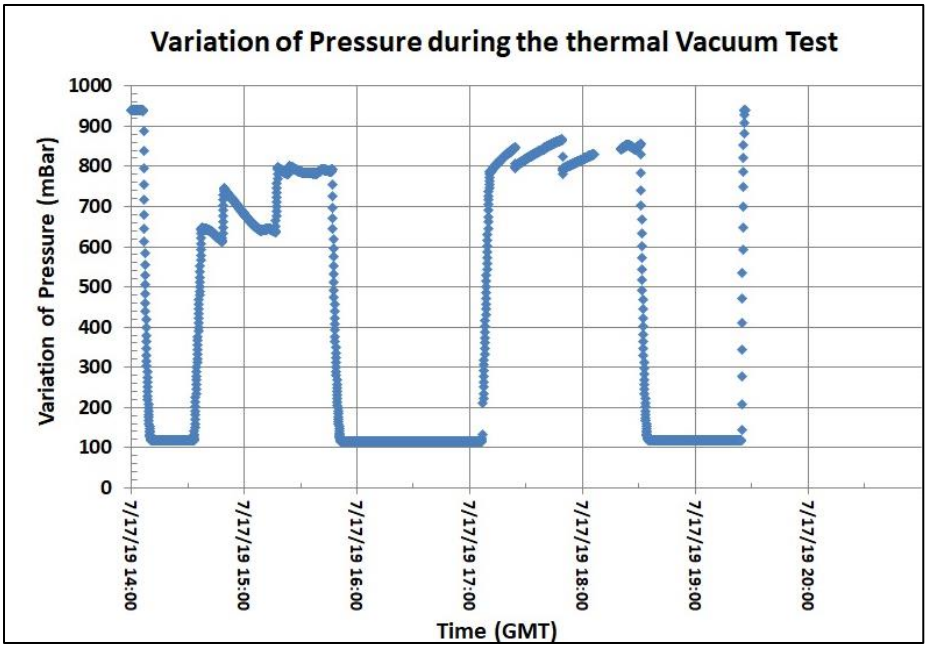

Fig.6 (a) Variation of pressure in the thermal vacuum chamber with time measured by the pressure transducer of UNF payload

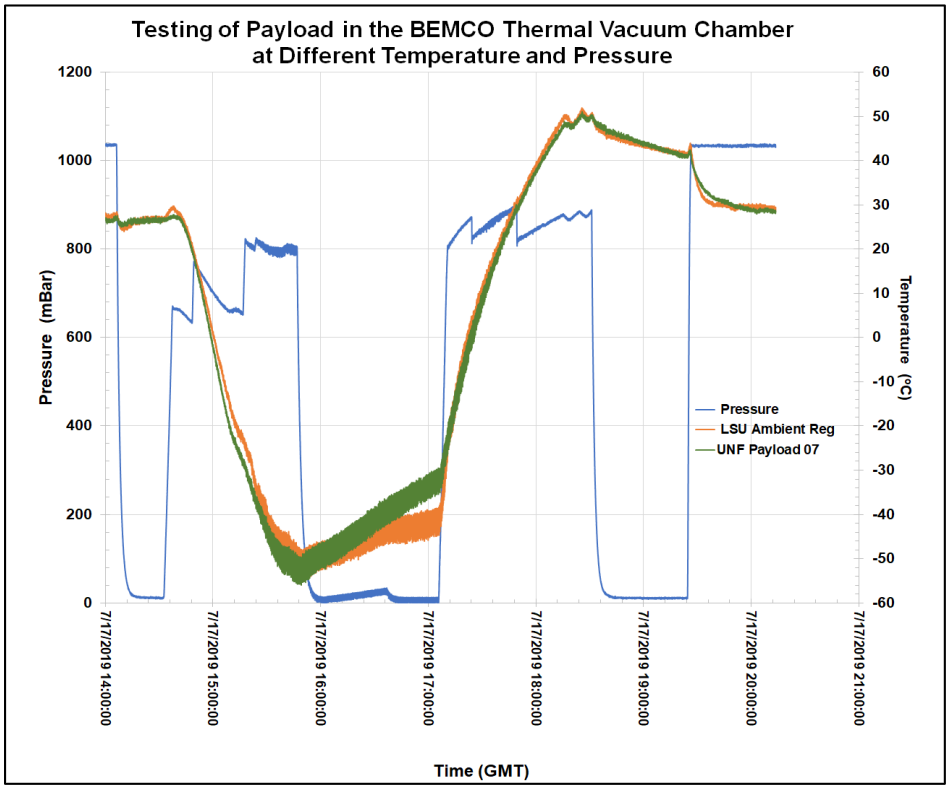

Fig.16 (b) Variation of pressure and temperature in the chamber with time measured by HASP (Data courtesy: Mr. Doug Granger, HASP- LSU).

The resistance of sensors was measured during the thermal vacuum test and are shown in the fig.17 (a), (b) and (c), respectively. The resistance of all sensors was nearly constant during the test. The resistance was slowly decreasing with time after 17:00 GMT. The ambient temperate in the chamber was set to increase at 17:00 GMT for about 2:30 hours. Due to the semiconducting properties of the sensor materials, it was expected that its electrical resistance should decreased with increasing of the ambient temperature as well outgassing from chamber wall, surface of hardware of platform and all payloads. However, that variation was reasonably small.

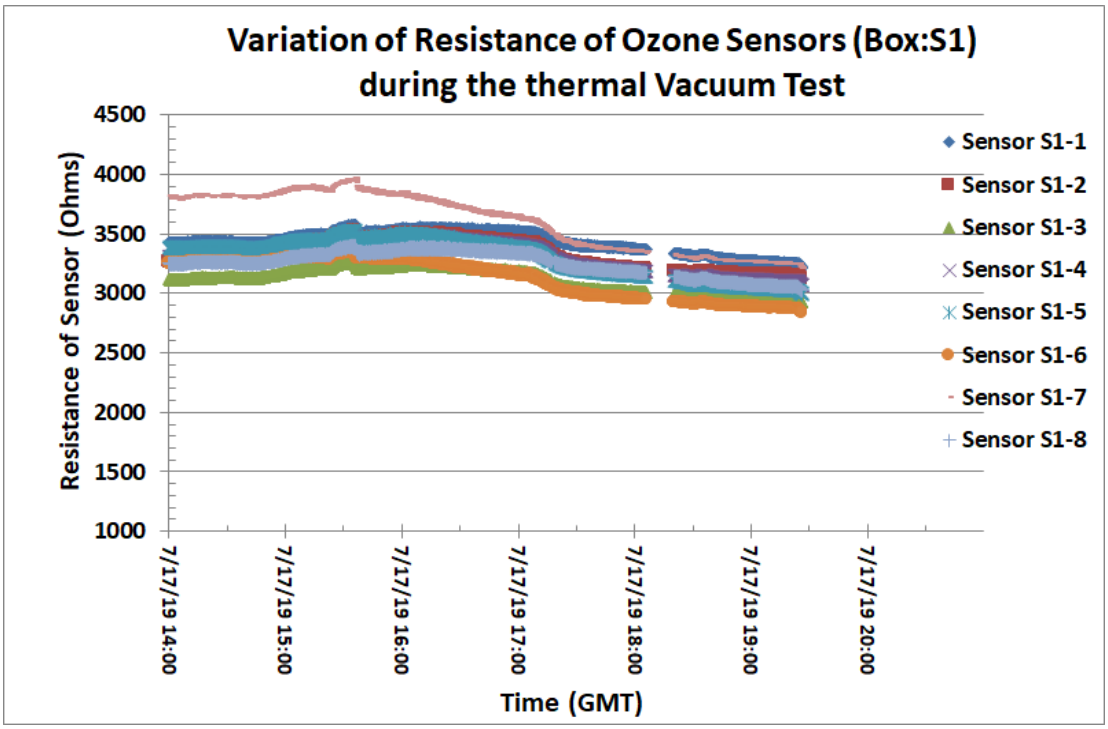

Fig.17 (a) Variation of resistance of gas sensors of sensors box #S1 with time during the thermal vacuum test

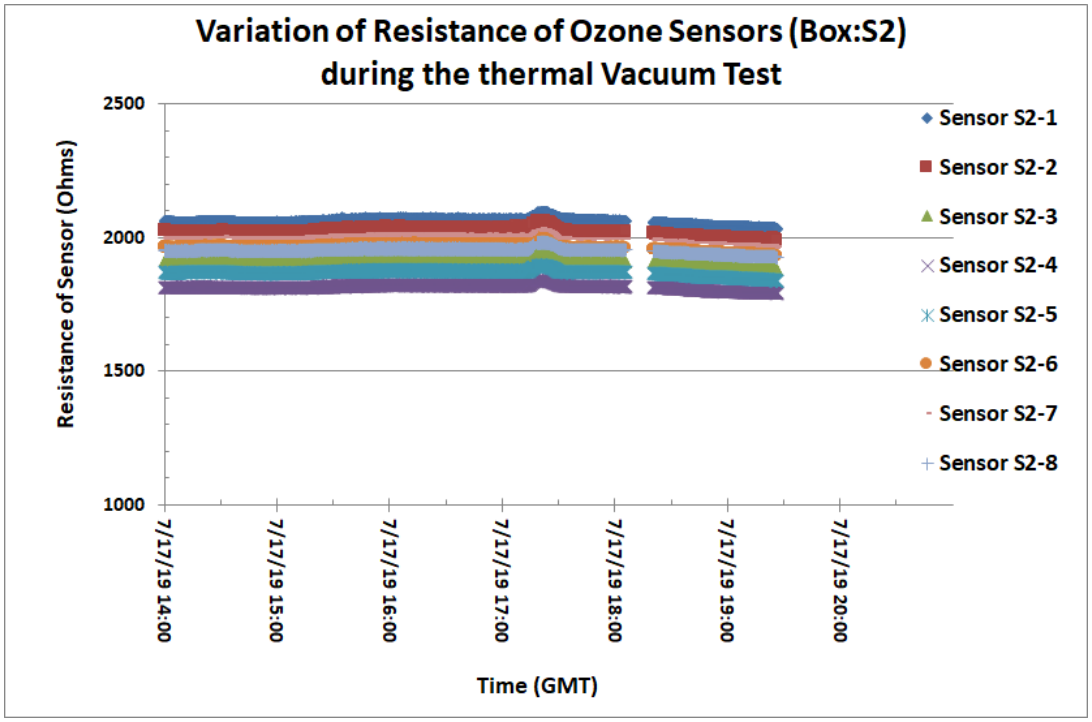

Fig.17 (b) Variation of resistance of gas sensors of sensors box #S2 with time during the thermal vacuum test

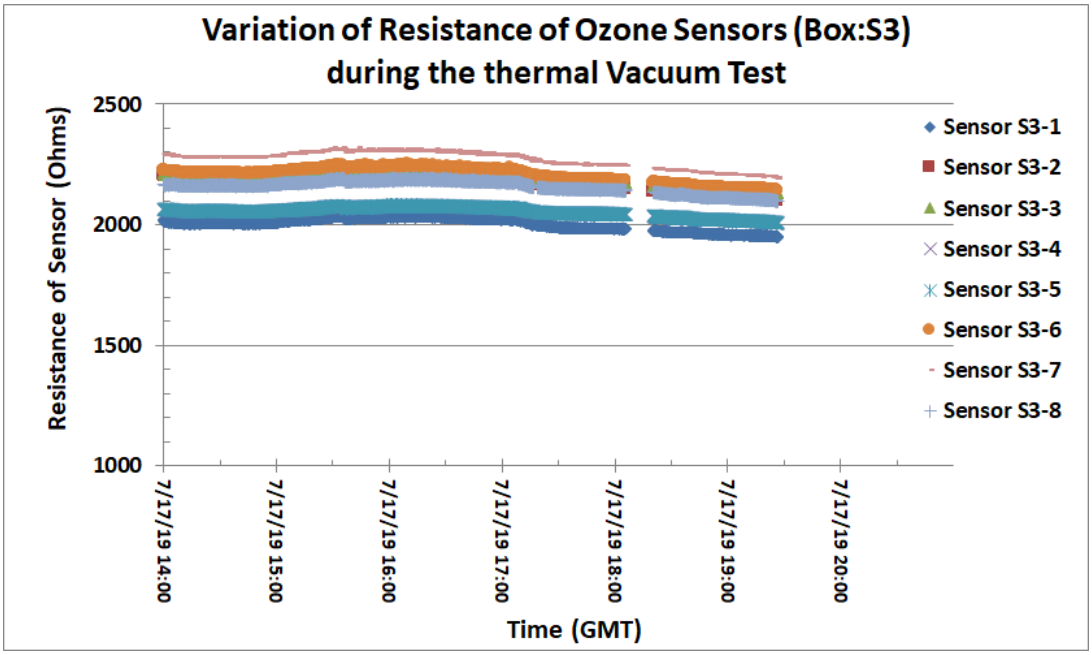

Fig.17 (c) Variation of resistance of gas sensors of sensors box #S3 with time during the thermal vacuum test

It was found that the sensors resistance was quite stable during the low temperature test cycle. A heater mounted on the back side of the sensors array was controlled by the on-off controller and maintained the temperature of sensors array constant during the low temperature test cycle.

Fig.18 shows the variation of temperature of all three sensors arrays with time. It shows all three arrays remain at the constant temperature during the test. A small peak of decrease in temperature was observed around 15:30 GMT due to intentionally turned off all three heaters and then turned on for testing of the uplink command as a part of testing procedure.

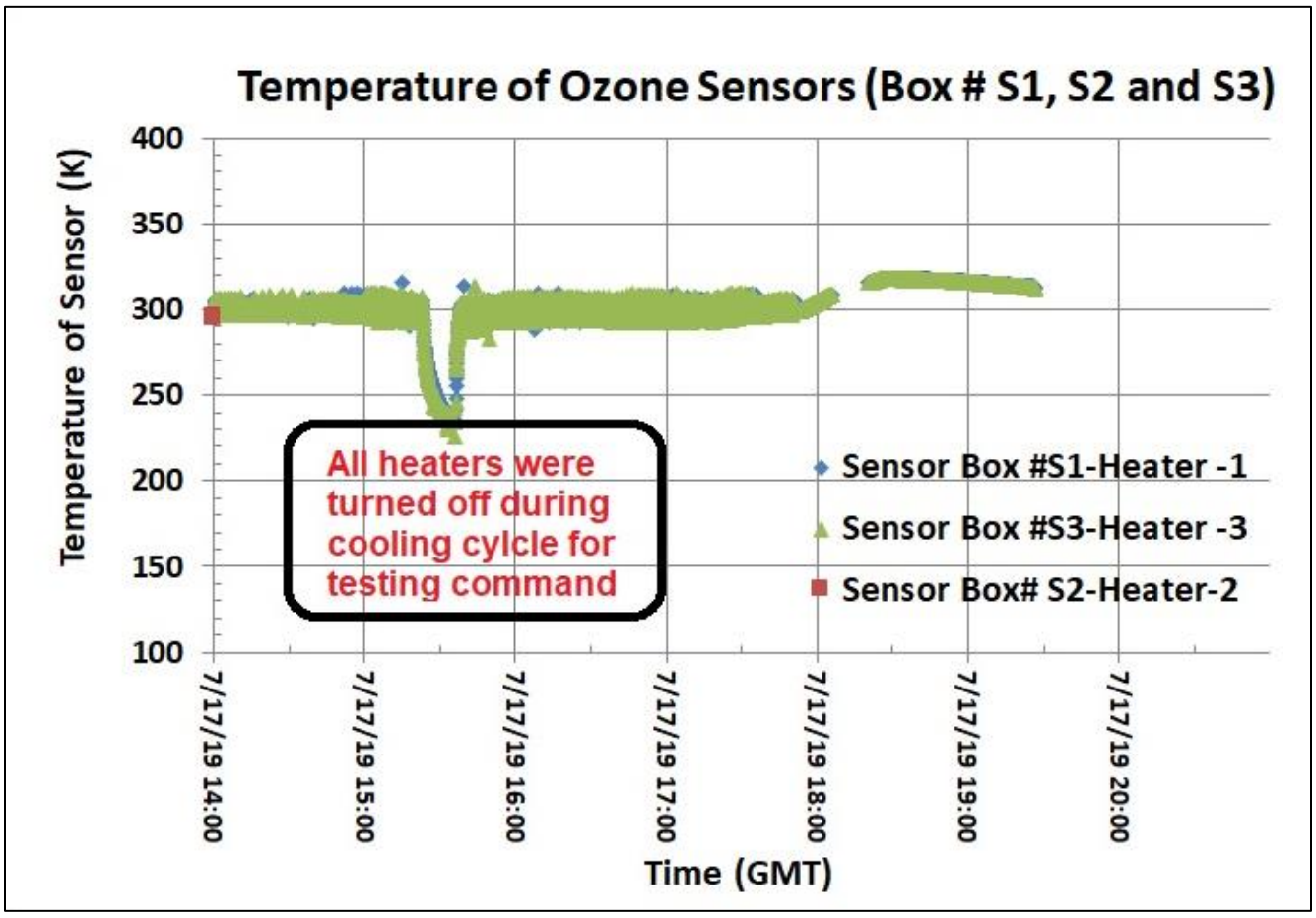

Fig.18 Variation of temperature of gas sensors of sensors box #S1, S2 and S3 with time during the thermal vacuum test

Fig. 19 (a) shows the response of photo diode sensors mounted on sensors boxes with time. It was observed that all three photodiode sensors were in working condition. The variation of photo voltage with time was due to stray light, light bulb and radiation heaters in the test chamber (Fig. 19 (b)).

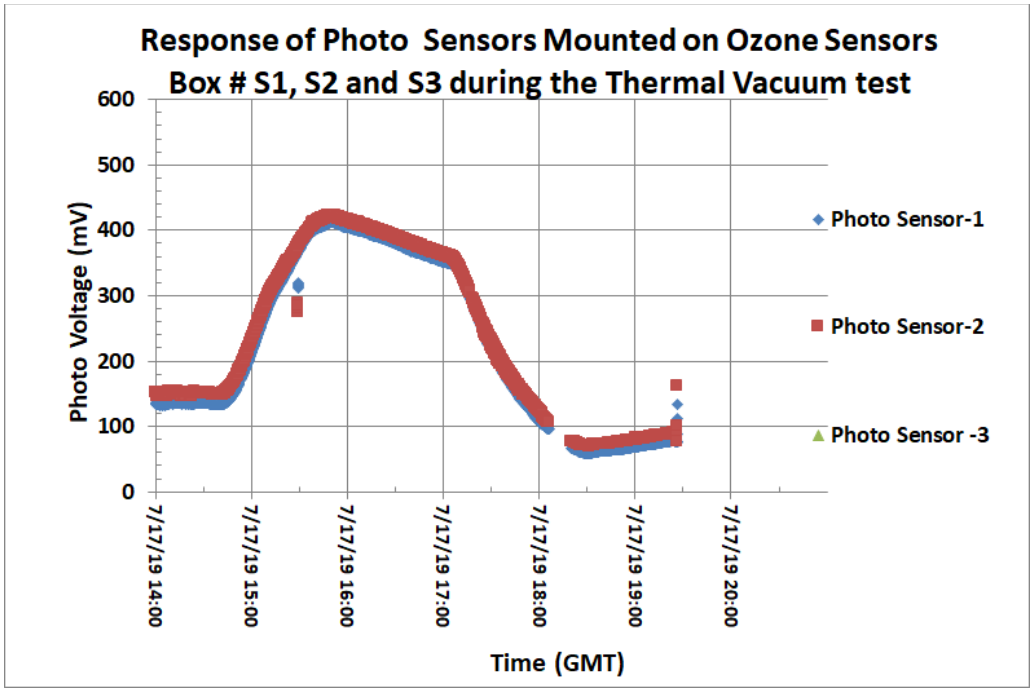

Fig.19 (a) Response of photo sensors mounted on Sensors box #S1, S2 and S3 with time during the thermal vacuum test

Fig. 19 (b) Innner view of a therma vacuum test chamber shows stray light, light bulb, and radiation heaters in the chamber.

During the thermal vacuum test, we have sucessfully tested five uplink commands. These commands were mainly for rest payload system, switching the payload GPS to HASP GPS, switching HASP GPS to the payload GPS, switching OFF all heraters and switching ON all heaters switch. Fig.20 (a) shows how the our data were changed in the EXCEL worksheet due to execution of the uplink commands.

HASP2019 Thermal Vacuum Test # 1, Wednesday, July 17, 2019

Payload # 7, Testing of Uplink Commands

Turn Master Heater Switch OFF

Command: HEAT_ON Hex Code: 7535

GPS Stamp	Time (UNIX/GMT)	Time (CST)	Time (GMT)	VOLT(mV)	CURRENT (mA)	PRESSURE (mBar)	Heater Status
HASP2013 UBLOX	152255	10:22 AM	15:22:55	3339	288	782	111
HASP2013 UBLOX	152300	10:23 AM	15:23:00	3341	173	781	11
HASP2013 UBLOX	152305	10:23 AM	15:23:05	3341	38	781	10
HASP2013 UBLOX	152310	10:23 AM	15:23:10	3344	161	781	110
HASP2013 UBLOX	152315	10:23 AM	15:23:15	3344	21	783	1110
HASP2013 UBLOX	152320	10:23 AM	15:23:20	3344	22	786	1110
HASP2013 UBLOX	152325	10:23 AM	15:23:25	3343	22	788	1110

Turn Master Heater Switch ON (Default)

Command: HEAT_OFF Hex Code:7636

GPS Stamp	Time (UNIX/GMT)	Time (CST)	Time (GMT)	VOLT(mV)	CURRENT (mA)	PRESSURE (mBar)	Heater Status
HASP2013 UBLOX	153555	10:35 AM	15:35:55	3366	37	783	1110
HASP2013 UBLOX	153600	10:36 AM	15:36:00	3366	24	783	1110
HASP2013 UBLOX	153605	10:36 AM	15:36:05	3379	278	783	111
HASP2013 UBLOX	153610	10:36 AM	15:36:10	3365	282	783	111
HASP2013 UBLOX	153615	10:36 AM	15:36:15	3366	272	783	111

Changing our payload GPS (HASP UBLOX) to HASP GPS (HASP)

Command: HASP_STREAM Hex Code: 7A3A

GPS Stamp	Time (UNIX/GMT)	Time (CST)	Time (GMT)
HASP2013 UBLOX	180535	1:05 PM	18:05:35
HASP2013 UBLOX	180540	1:05 PM	18:05:40
HASP2013	1563386752	1:05 PM	18:05:52
HASP2013	1563386762	1:06 PM	18:06:02

Changing HASP GPS (HASP) to our payload GPS (HASP UBLOX) (Default)

Command: UBLOX_STREAM Hex Code: 7939

GPS Stamp	Time (UNIX/GMT)	Time (CST)	Time (GMT)
HASP2013	1563387612	1:20 PM	18:20:12
HASP2013	1563387622	1:20 PM	18:20:22
HASP2013 UBLOX	182025	1:20 PM	18:20:25
HASP2013 UBLOX	182035	1:20 PM	18:20:35

"Reset System" shown by "Hello" in the data string

Command: RESET Hex Code: 7131

GPS Stamp	Time (UNIX/GMT)	Time (CST)	Time (GMT)	S1-1(Ohm)	S1-2(Ohm)	S1-3(Ohm)	S1-4(Ohm)
HASP2013 UBLOX	191350	2:13 PM	19:13:50	2040	1997	1883	1797
HASP2013 UBLOX	191355	2:13 PM	19:13:55	2040	1997	1885	1797
HASP2013 UBLOX	191405	2:14 PM	19:14:05	HELLO			
HASP2013 UBLOX	191415	2:14 PM	19:14:15	2040	1997	1881	1797
HASP2013 UBLOX	191420	2:14 PM	19:14:20	2040	1999	1883	1797

Fig.20 (a). Testing of uplink commands during the thermal vacuum test

Our GPS has also measured the altitude during the thermal vacuum test. The measured values of altitude with time is shown in the Fig.20 (b). It shows that the plot has lot of variation and noise due to closed chamber in the building. The measured of values may not be correct as it was measured in side the chamber. But looking into average altiude of about 130 m, we can conclude that our GPS as well as HASP GPS both were worked well. There was some noise or minor data communcation issue. We will check the data of altitude and other data too again during the hang test and before launching of the payload.

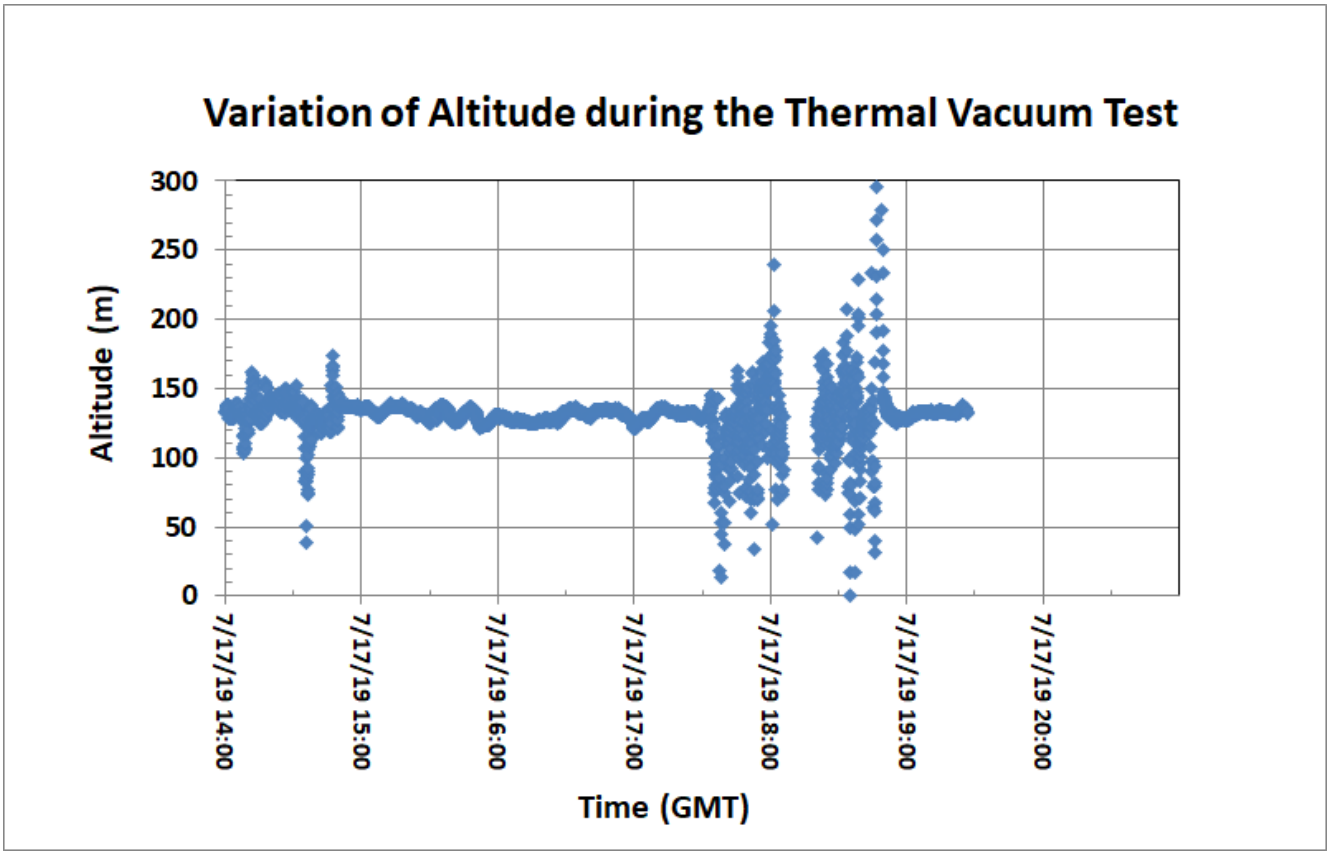

Fig. 20(b) Measured altitude with time during the thermal vacuum test.

After sucessful completion of the thermal vacuum test, the payload was disintegrated from the HASP platform. The payload was packed in the shipping box having FedEx prepaid shippinmg label (Fig. 20(c)). The payload box was transported to the CSBF, Fort Summner, NM by HASP-LSU.

Fig. 20(c) Trevor and Joseph packed the payload.

8. Launching of Payload

The payload was again mounted on the HASP platform and performed the power ON and data communication tests at the CSBF, Fort Sumner. The HASP with all payloads was undergone the hang test and FRR during September 1 to 4, 2019. Fig. 21 (a) to (c) shows the pictures of launch preparation at the CSBF, Palestine, TX, starting of launch and structural view of balloon attached with HASP.

Fig.21(a) Preparation of launch.

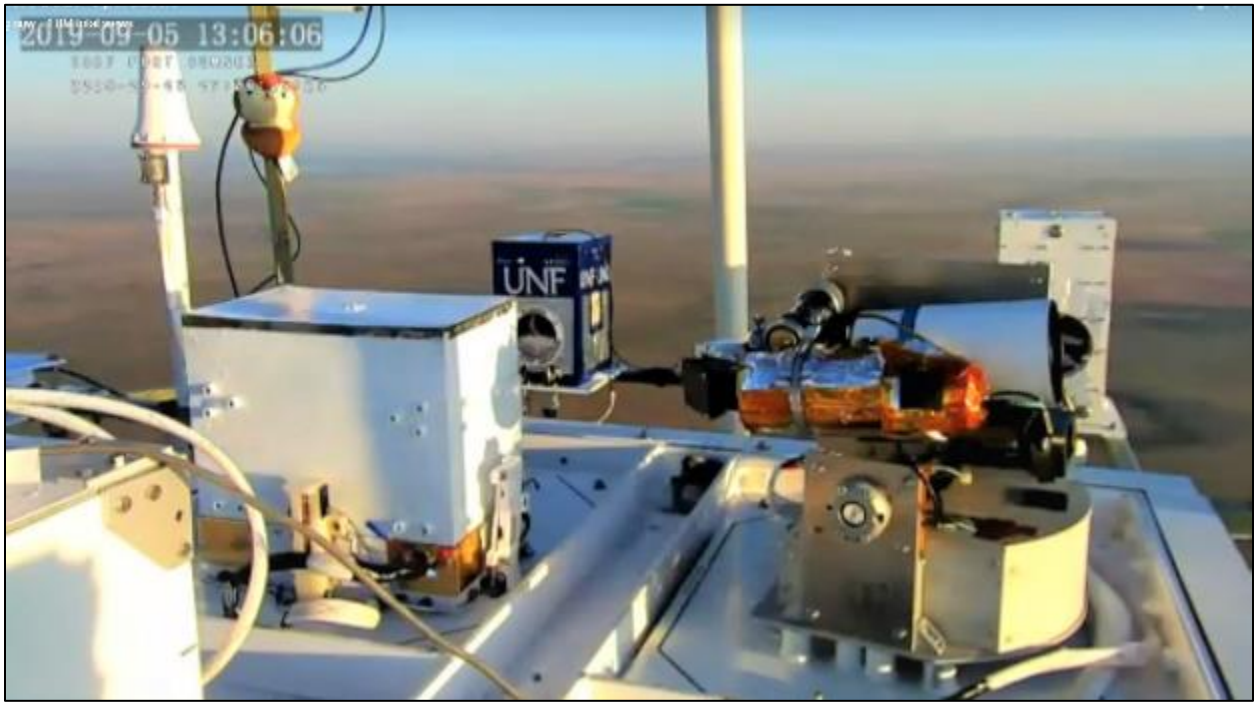

Fig.21(b) Just launching of HASP 2019 flight from Fort Sumner.

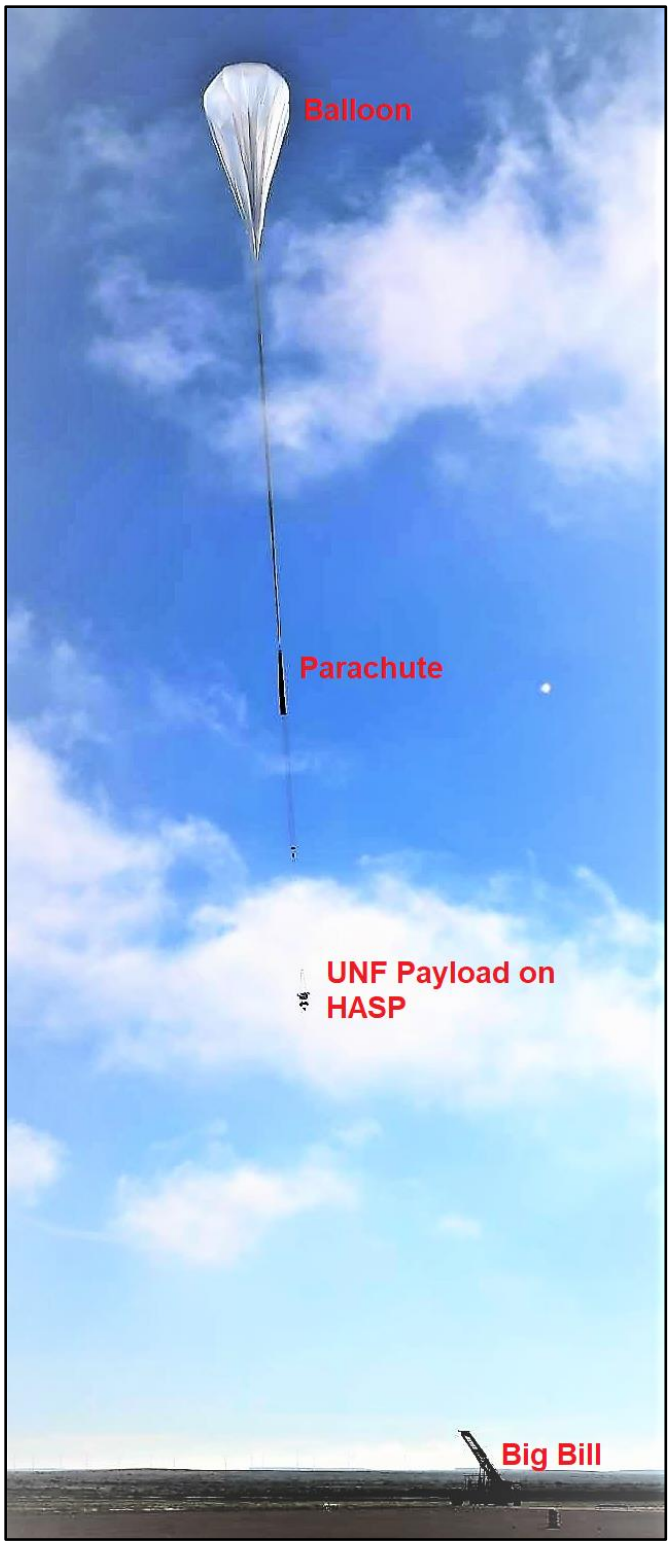

Fig. 21(c) Structural view of ballon and parachute attached to HASP at the time of launch.
(Picture Courtesy: Doug Granger, HASP-LSU)

HASP2019 flight was sucessfully launched into the startosphere at an altitude of about 125,000 feet from the NASA- CSBF, Fort Sumner, NM on September 5, 2019 at 13:03:15 UTC.

A video camera mounted on HASP delivered video stream during the flight. HASP in starosphere is shown in fig. 22(a) and (b).

Fig. 22(a) HASP in stratosphere during daytime

Fig. 22(b) HASP at the time of termination of balloon flight. Enough sunlight was available during sunset time.

Fig. 23 shows the flight path of the balloon on the Google map.

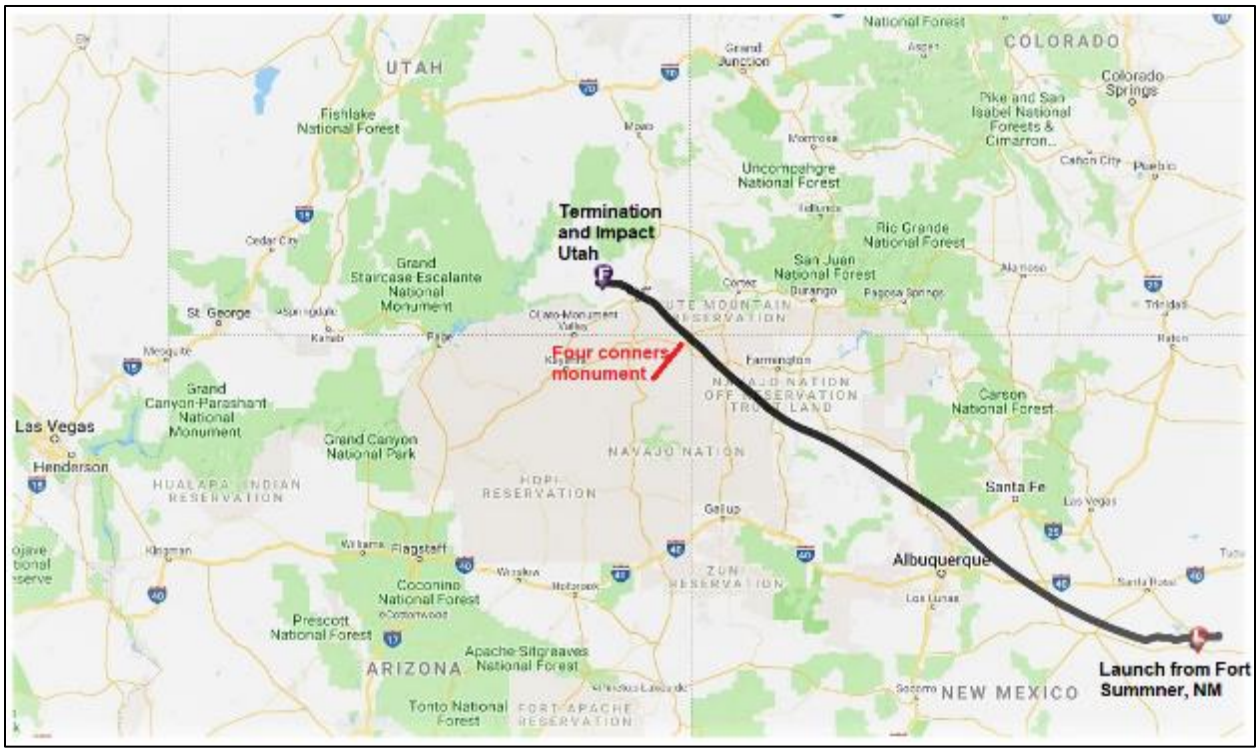

Fig.23 Flight path of the balloon flight on the Google map. The flight path crossed the four states corner monument.

After spending 7 hour and 37 minutes at float altitude, the flight was terminated on September 5, 2019 at 23:17:56 UTC. The HASP was impacted in rugged terrain West of White Mesa, Utah on September 5, 2019 at 23:53:03 UTC. The CSBF recovery truck has not be able to find a route that can be used to drive up to or near the payload and helicopter was used to retrieve the gondola. During the flight, the UNF ozone sensors array detected and measured ozone in the stratosphere. The payload sent out the data files during the flight without any problem. Our payload was recovered with minor damage.

9. Results and Discussions:

9.1 How ozone profile measured in the Starosphere?

Fig. 24 shows various steps for the detection of ozone by the sensors payload during the flight.

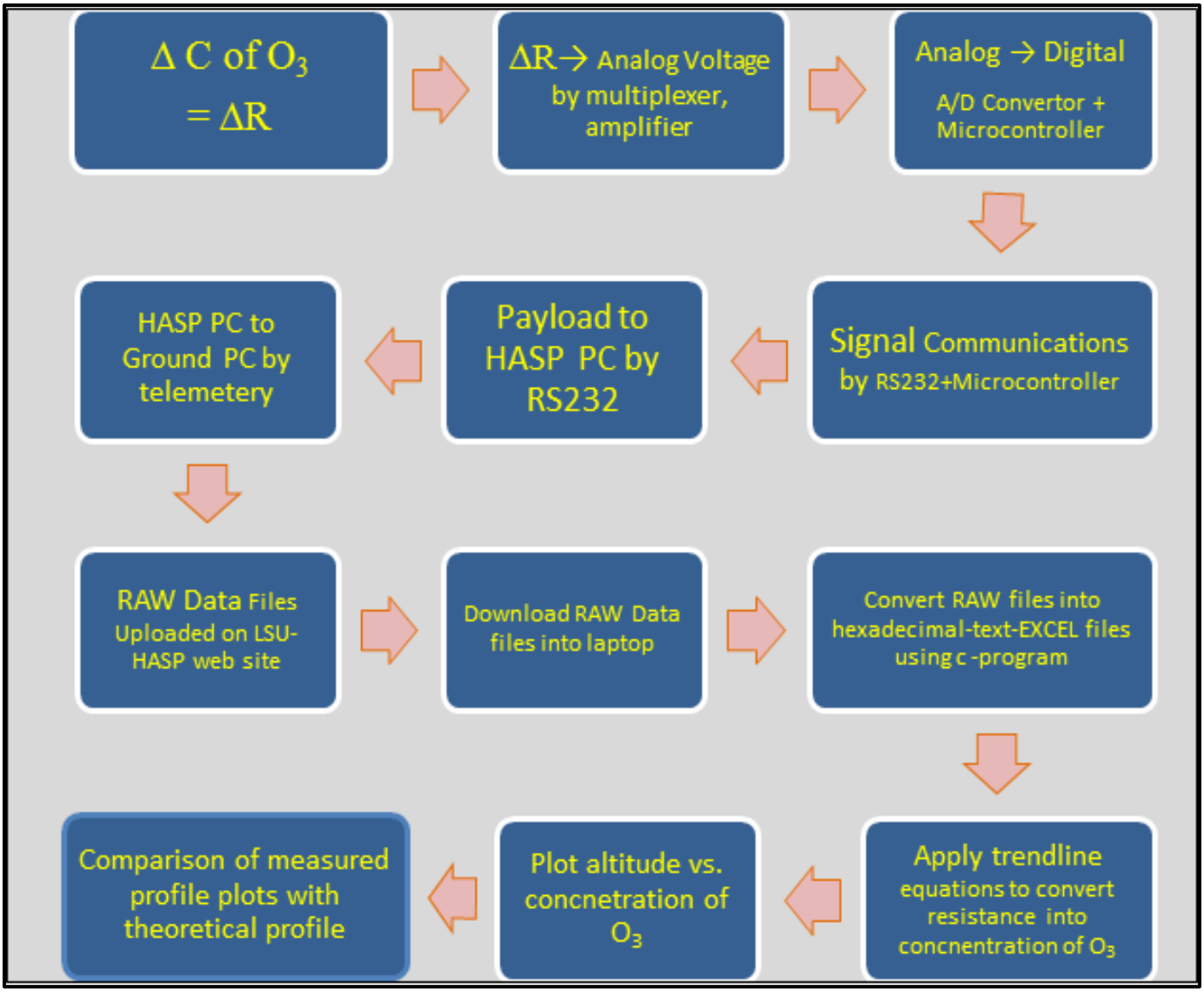

Fig.24 Steps for the detection of ozone by the payload

During the flight, UND-UNF sensors payload measured the ozone profile. The payload sent data files of 25 KB every 18 minutes during the flight time through the NASA-HASP computer and was uploaded on the HASP website. We downloaded all the RAW data files, and converted RAW files into one EXCEL file using the software program. The payload worked very smoothly.

9.2 Uplinks commands

Uplink commands shown in table-4 for reset, switching the HASP GPS to UBLOX GPS, heater ON and heater OFF were applied to operation of the payload.

Table-4 Uplink commands

Command	Hex Code	Description	Importance
RESET	**7131**	Reset System	Critical
HEATER OVERRIDE_ON	**7535**	Turn Master Heater Switch Off. The main heater switch is disabled so no individual heaters will be able to turn ON.	Critical
HEATER OVERRIDE_OFF	**7636**	Turn Master Heater Switch On (default). The main heater switch is enabled and thus each individual heater can turn ON or OFF as needed by the temperature controller.	Critical
UBLOX_STREAM	**7939**	Stream GPS via Embedded GPS (default)	Critical
HASP_STREAM	**7A3A**	Stream GPS via HASP GPS	Critical

Fig. 25 Communication templet on Google.

During hang test at CSBF, Fort Sumner, NM and during the balloon flight, we used the Google account for communications with Mr. Doug Granger, HASP-LSU. The Google account templet is shown in fig. 25. We can inform about the payload status, receive the flight information and send request to uplink the command. The advantage of this method for communications is no need to use cell phone to call Mr. Doug Granger.

9.3 Balloon Flight Profile and Response of Pressure Sensor

Fig. 26 shows the HASP 2019 balloon flight profile. The altitude profile was measured by our payload GPS. Our UBLOX GPS worked very well during the flight and not blocked at higher altitude by FAA. We did not need to switch to HASP GPS. The average altitude was around 36,500 m during the float. The float time was 7 hours and 37 minutes.

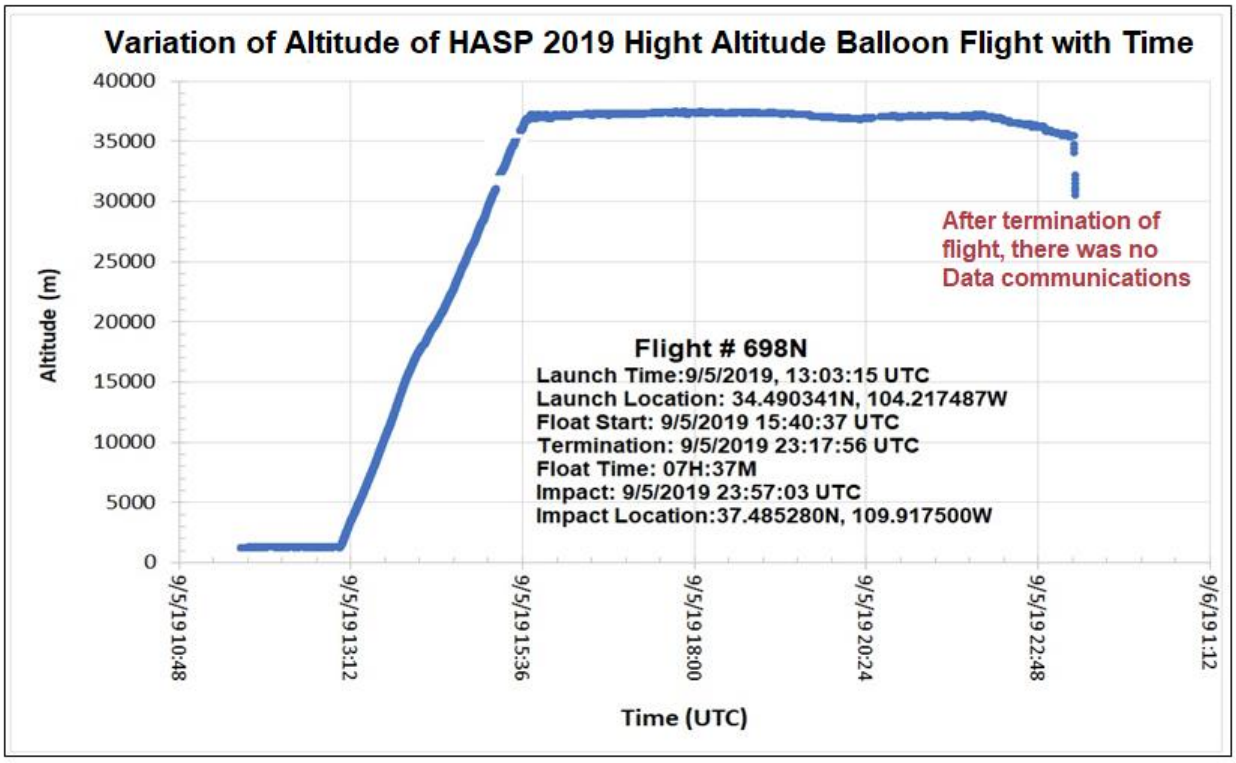

Fig.26 HASP2019 flight profile.

Fig.27 (a) shows the variation of pressure with the altitude during the flight. Pressure was measured by a pressure sensor mounted on the PCB of the payload measured the ambient pressure during flight. The pressure was decrease with increase of the altitude up about 18 km and then nearly saturate with increase of altitude up to the float. The saturation of pressure around 100 mbar was due to the technical limitation of our pressure sensor.

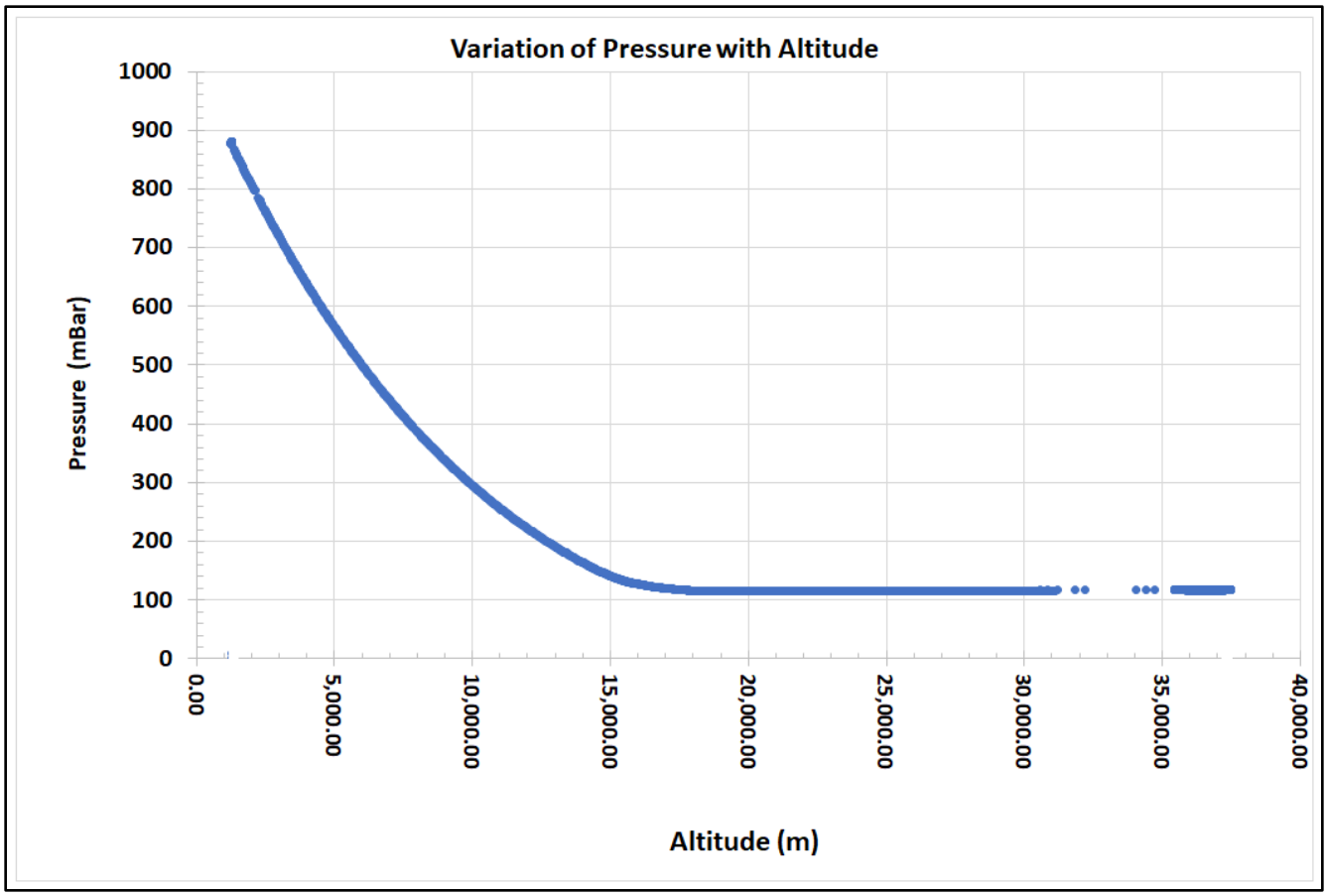

Fig.27 (a) Variation of pressure with altitude

Fig. 27 (b) shows the variation of pressure measured by the payload with the flight time (UTC). It shows change of pressure with time during flight.

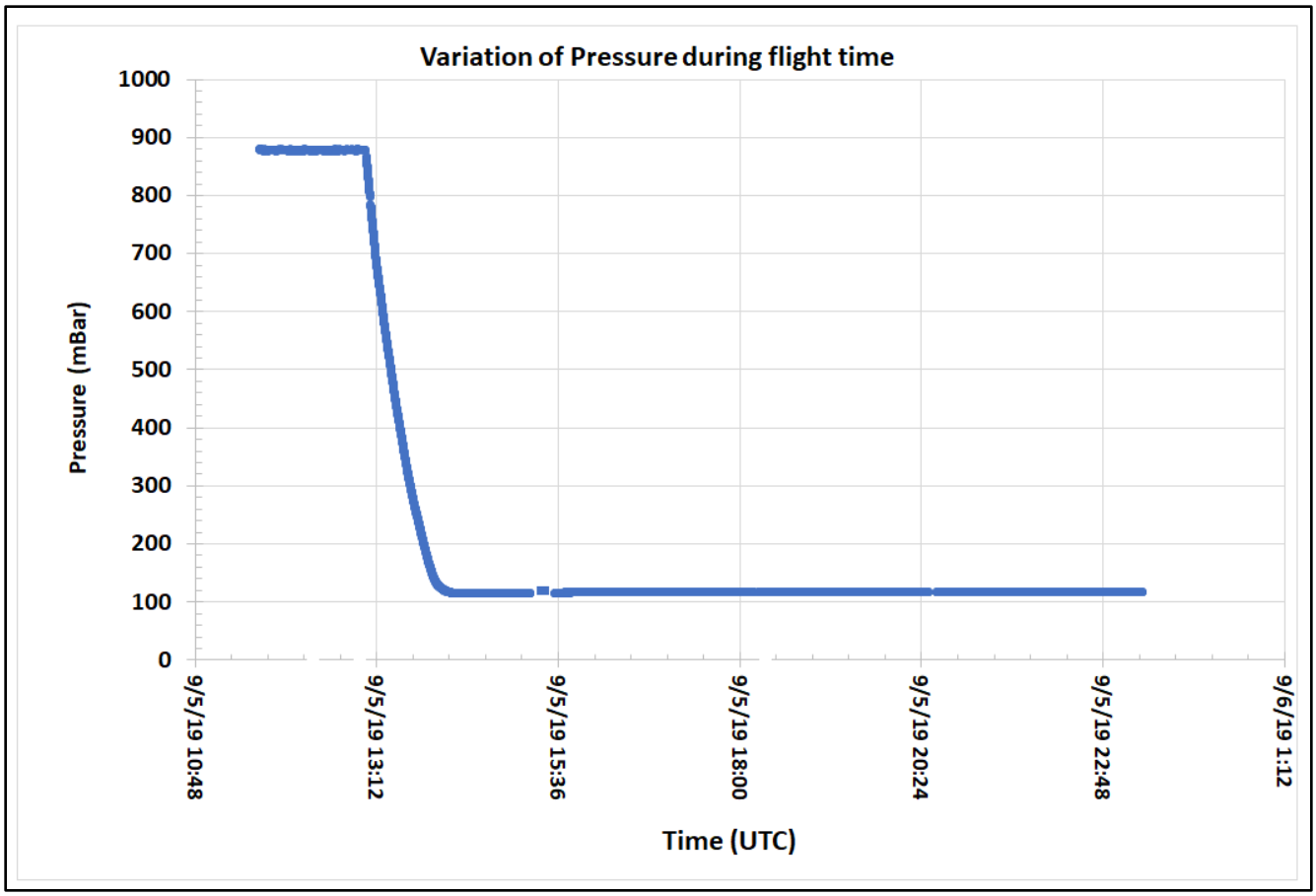

Fig.27 (b) Variation of pressure with time.

Fig. 27 (b) shows the variation of pressure measured by the payload with the flight time (UTC). It shows change of pressure with time during ascending and float. We did not get the data after termination of the flight due to no data communications.

9.4 Power budget during the flight

Fig.28 (a) shows the voltage applied to the payload during the flight. It was found that applied average voltage remain nearly constant about 3300 ±25 mV.

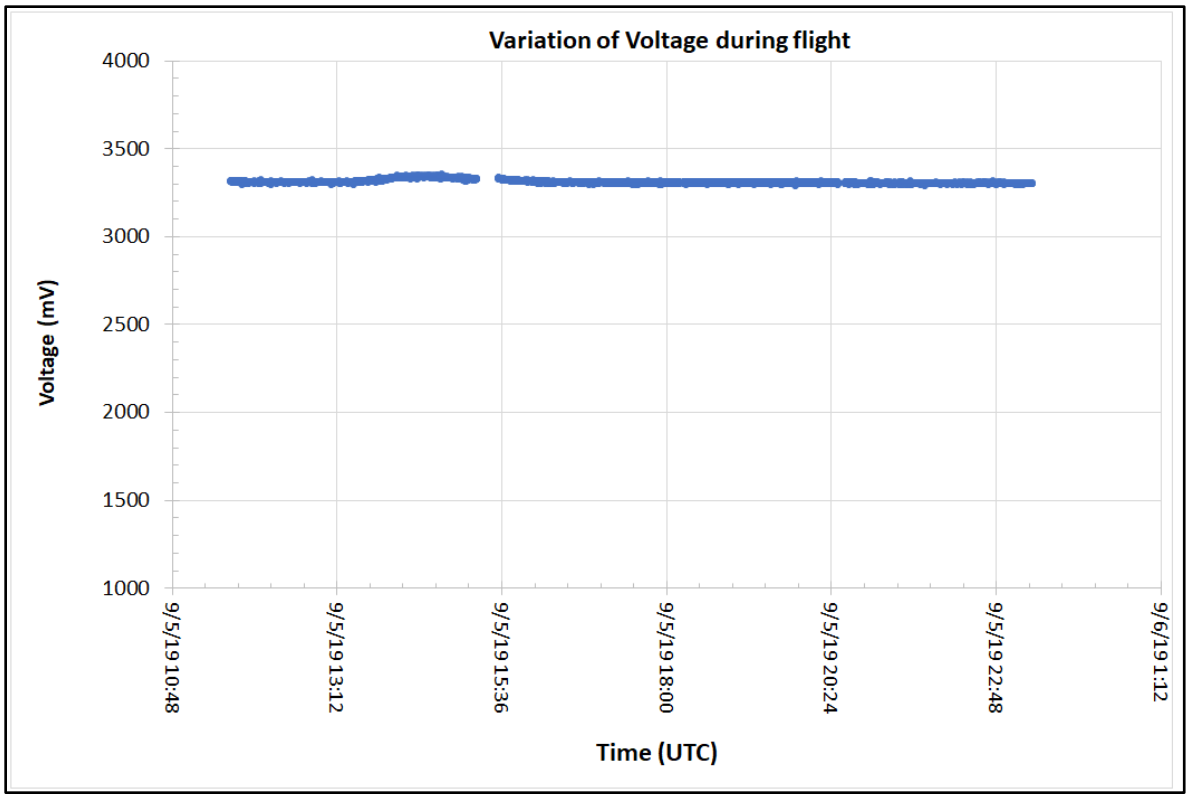

Fig.28 (a) Voltage applied to the payload during the flight.

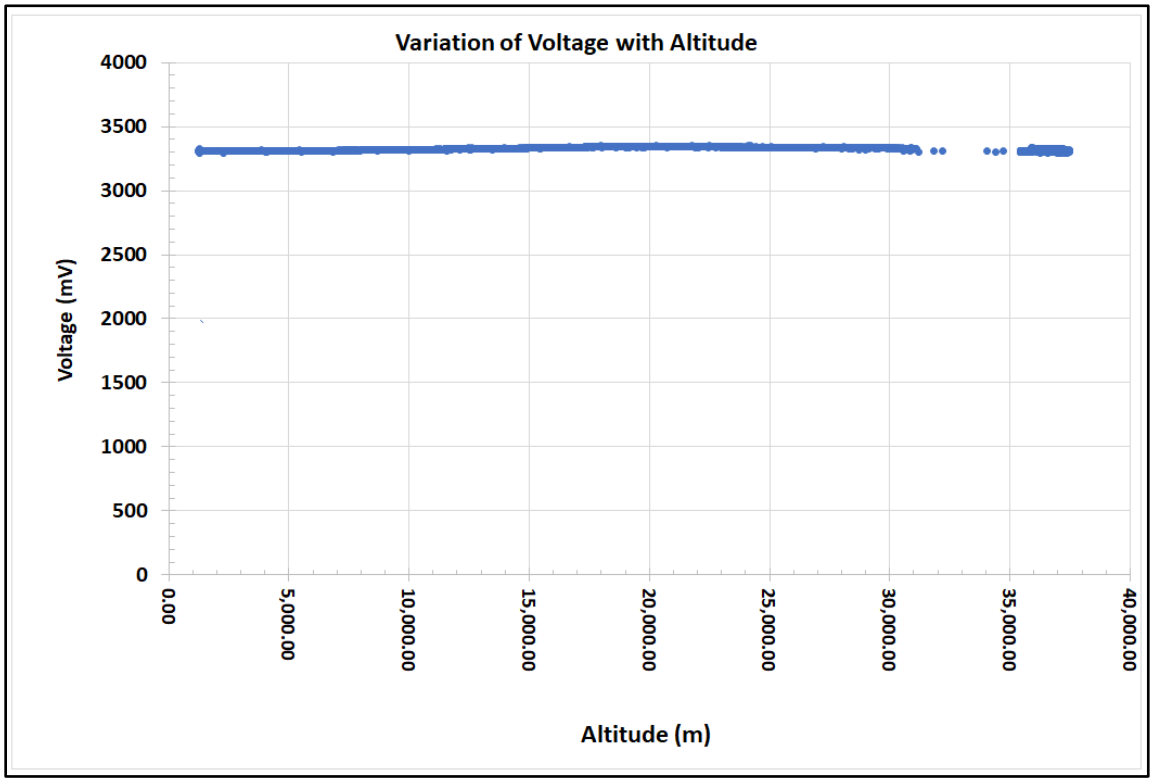

Fig.28 (b) Variation of voltage drawn by the payload with altitude

The current drawn by the payload during the flight is shown in fig. 29.

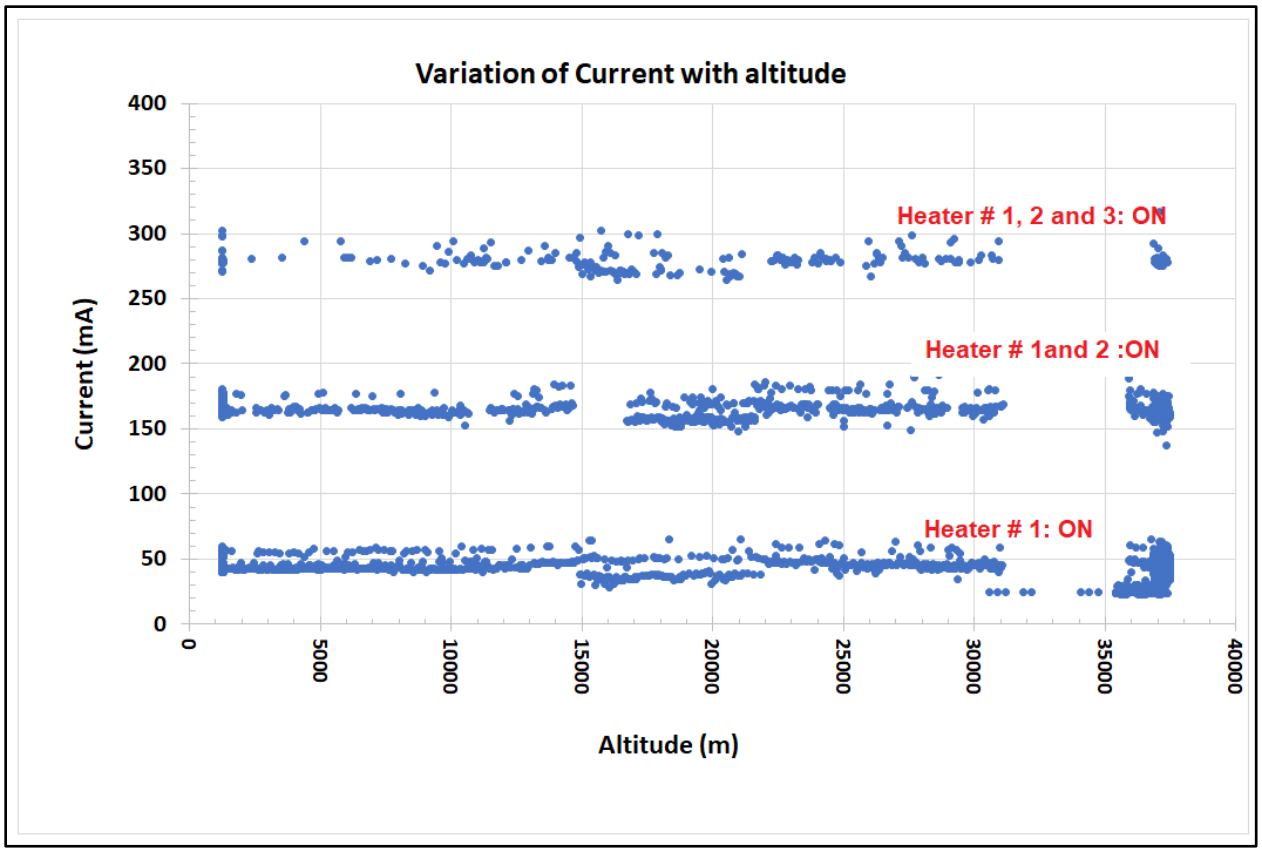

Fig.29 Current drawn by the payload during the flight.

The current drawn by the payload during the flight was

(i) About 30 ±5 mA when all three heaters were off,
(ii) About 60± 20 mA when Heater #1 ON,
(iii) About 170 ± 20 mA when Heater # 1 and 2 ON and
(iv) About 290 ± 25 mA when all three heaters were ON.

The power budget was maintained under the upper limit of HASP requirement during the flight.

9.5 Thermal stability of the payload

Fig. 30 (a) to (c) shows the variation of temperature of ozone sensors box #1, 2 and 3 with altitude during the flight. The digital temperature controller controlled the temperature of ozone sensors in the range of 303 ± 10 K during the flight. The digital temperature controller consisted on an On-Off controller, a polyimide flexible heater (MINCO make) and a temperature sensor (TMP 36). Temperature of sensors was nearly stable and controlled during the most of time of the flight.

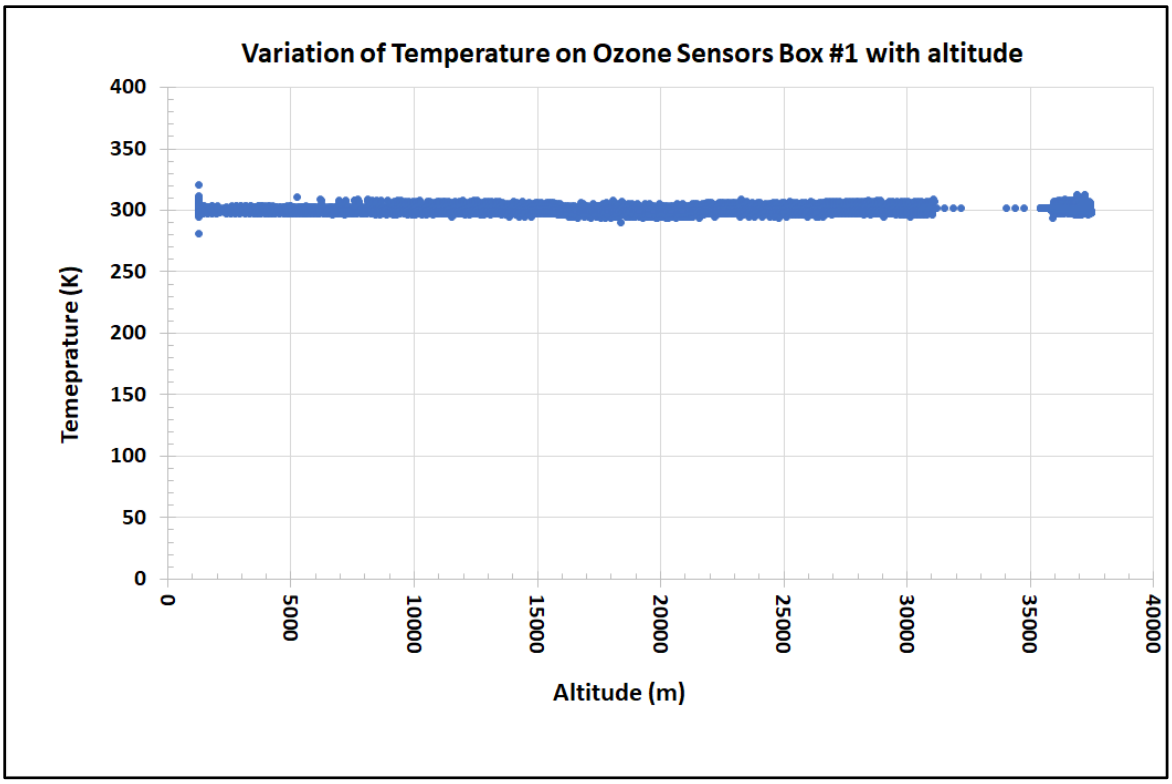

Fig.30 (a) Variation of temperature of ozone sensors in box#1 with altitude

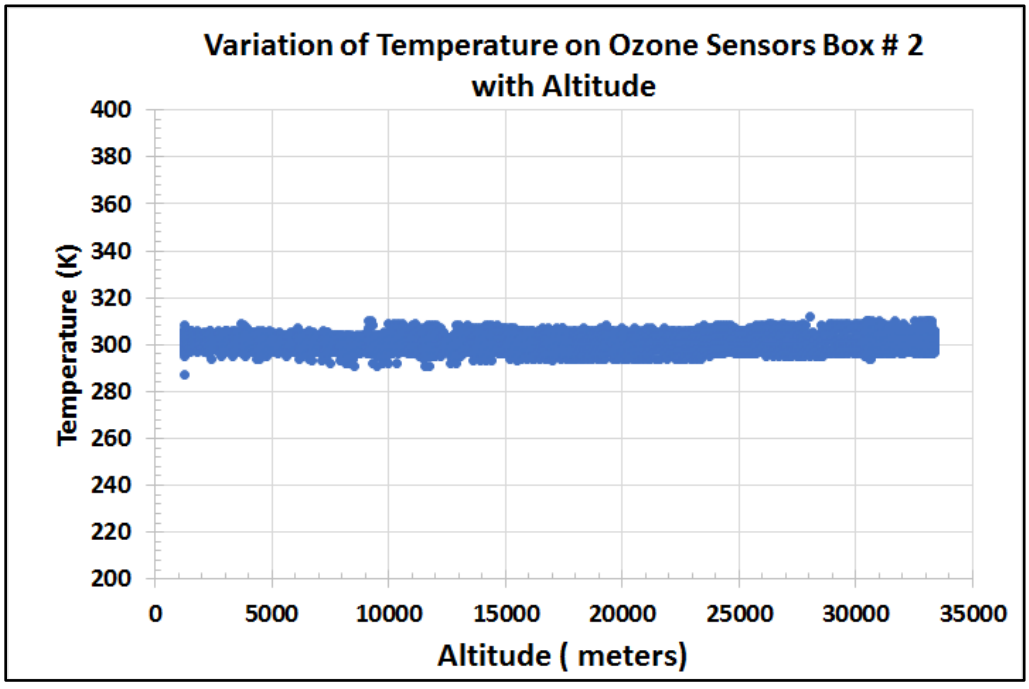

Fig.30 (b) Variation of temperature of ozone sensors in box#2 with altitude

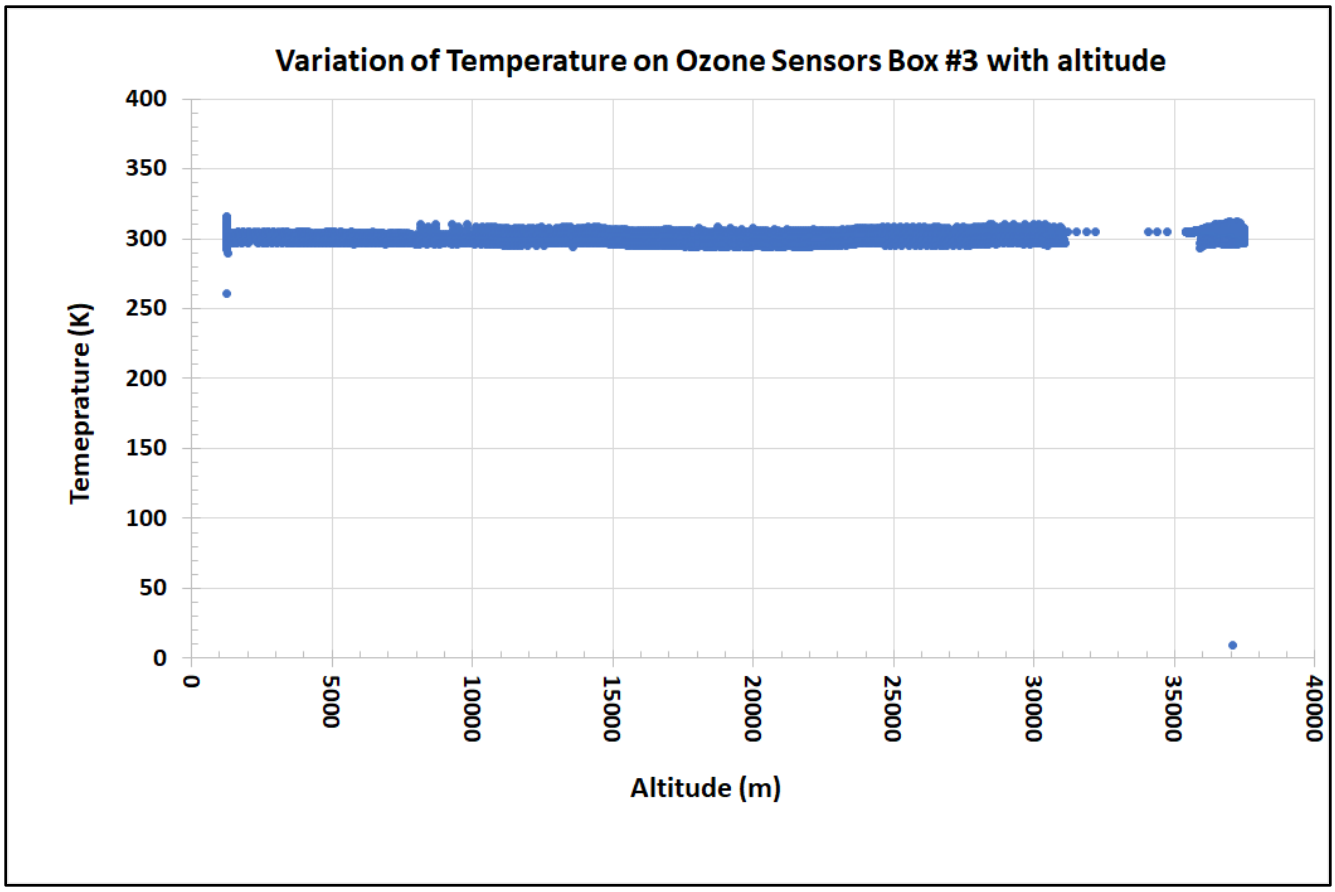

Fig.30 (c) Variation of temperature of ozone sensors in box#3 with altitude

Fig. 31 shows the comparison of measured average temperature on sensors Box # 1, 2 and 3 with standard deviation as error bar. All three columns are overlapping each other within their standard deviation and hence no statistical significance difference.

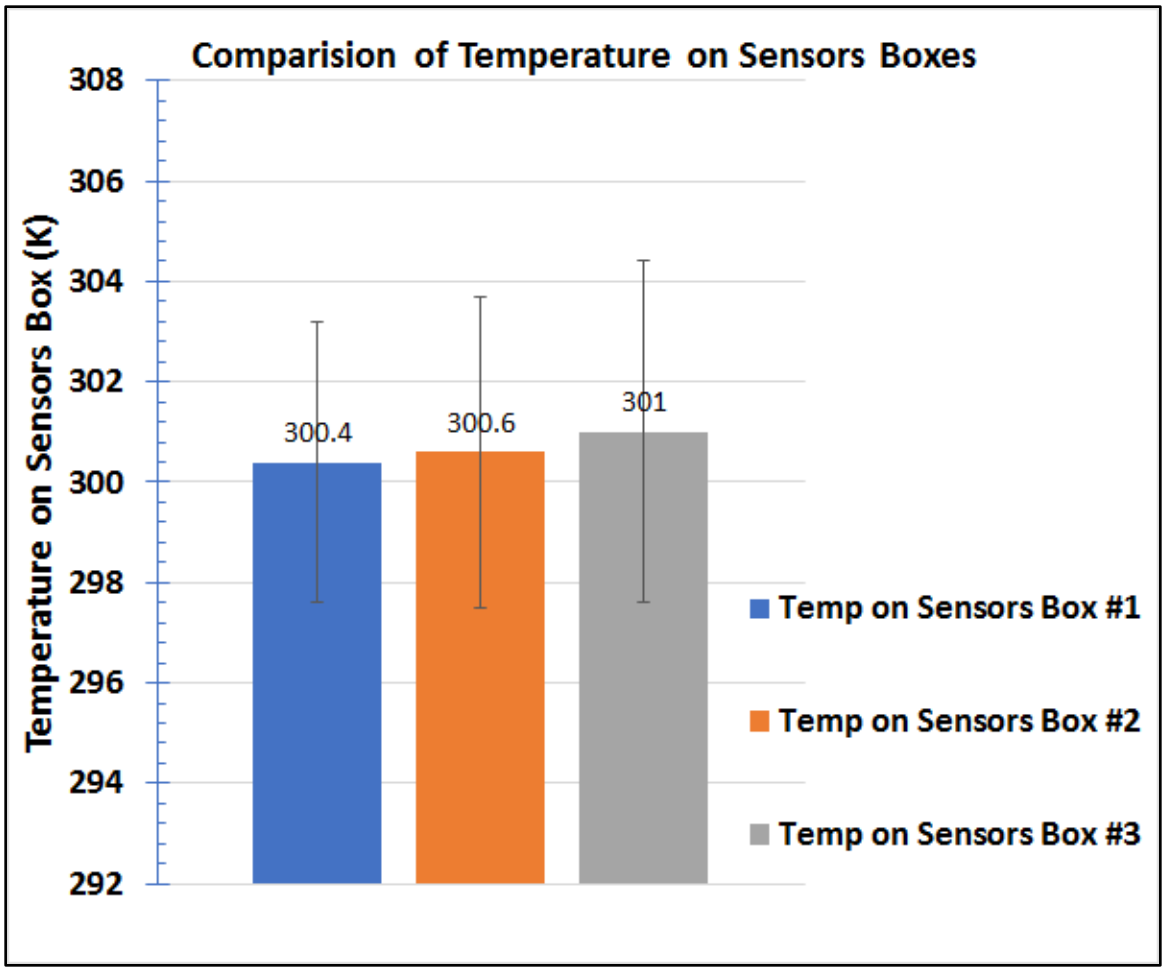

Fig 31. Compression of average temperature and standard deviation of temperature of sensors array box# 1, 2 and 3 during the flight.

Variation of temperature of ozone sensors in box#1, 2 and 3 with time (UTC) is shown in the fig. 32(a) and (b) respectively. All three plots shows the reasonable stability of temperature of ozone sensors in the box # 1 and 3.

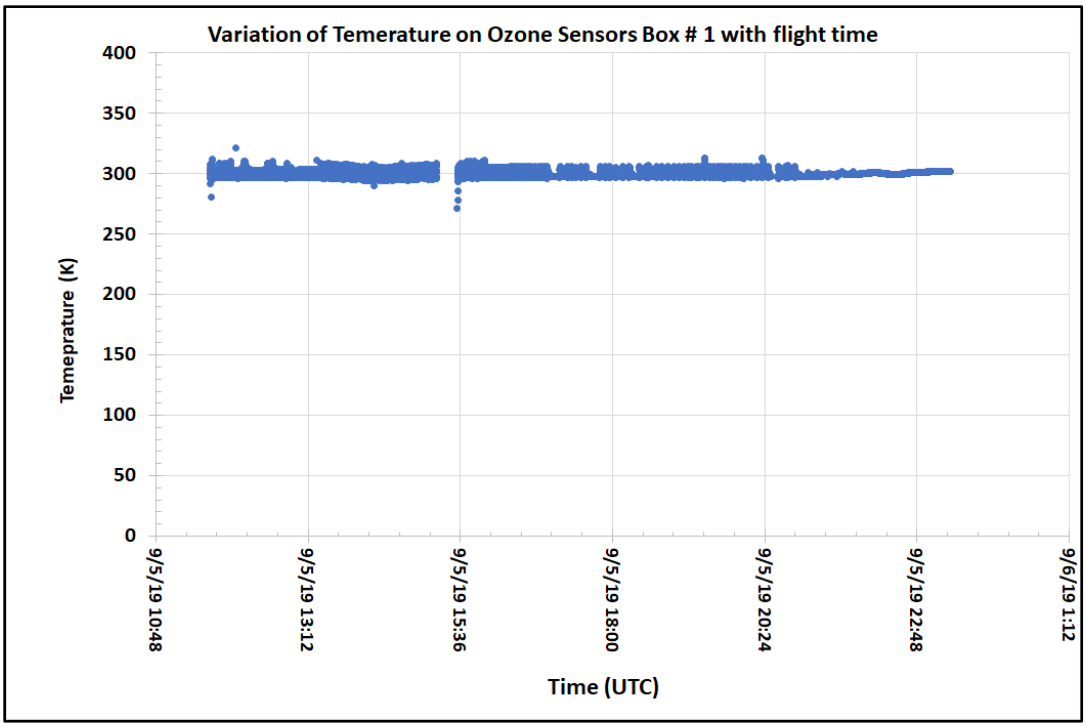

Fig.32 (a) Variation of temperature of ozone sensors in box#1 with time (UTC)

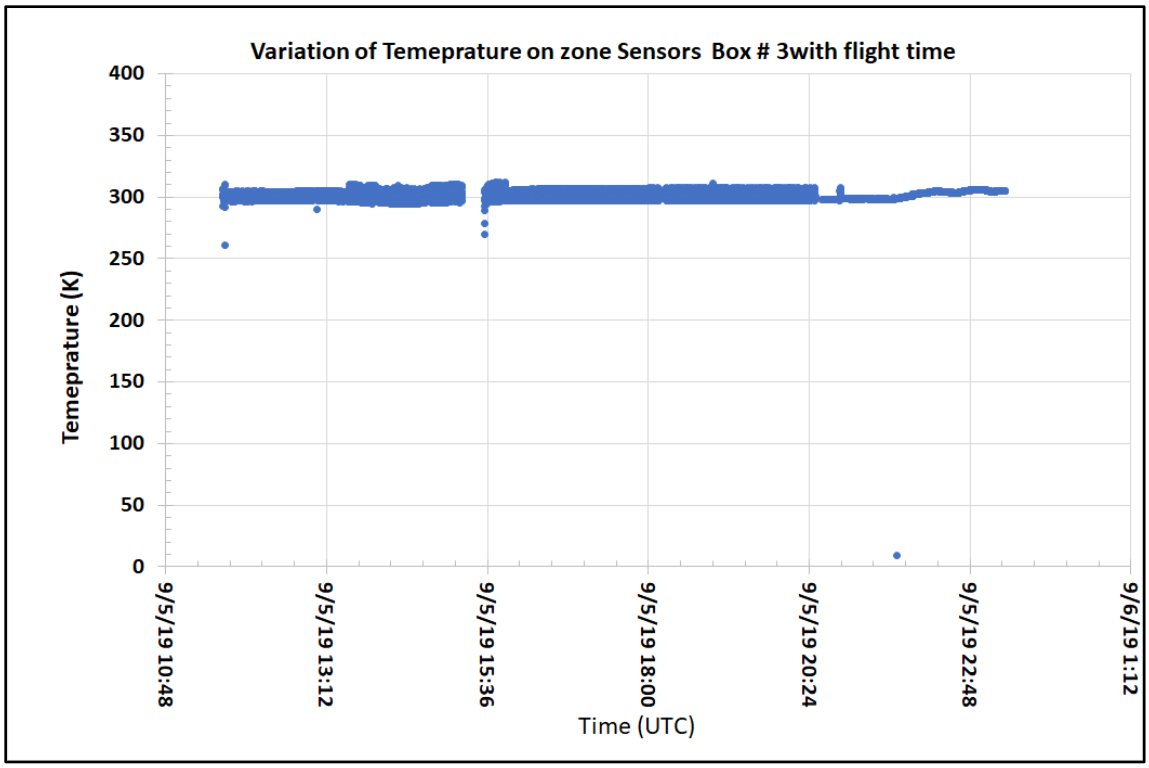

Fig.32 (b) Variation of temperature of ozone sensors in box#3 with time (UTC)

Fig. 32 (c) shows variation of ambient temperature outside of HASP with time. It was varied from about -60 to 50 ^{o}C (= 213 to 323 K). We are thankful to Mr. Douglas Granger, HASP-LSU for sharing ambient temperature data.

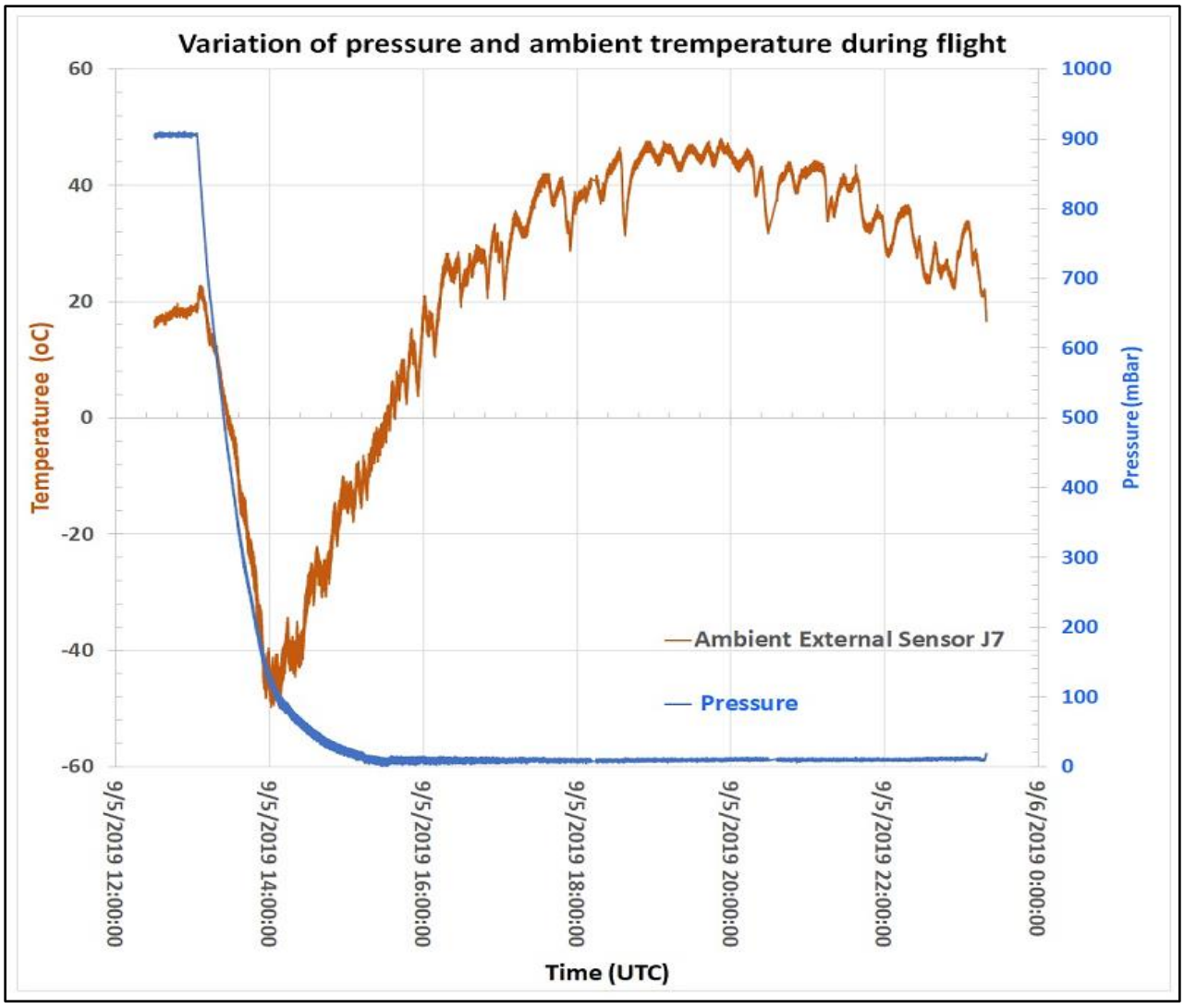

Fig. 32(c) Variation of ambient temperature outside of HASP
(Data Courtesy: Mr. Doug Granger, HASP-LSU)

The temperature controller on sensors was maintained constant temperature in the range 303±10 K when temperature dropped down by turning on heater. We did not apply a solid-state Peltier cooling device on the backside of sensors array to cool down sensors array when temperature increase higher than 313 K. We can add a Peltier-cooling device on the backside of sensors array in future but it will certainly increase the power consummation and need to change the power budget. Dr. Patel had developed p-Sb_2Te_3 - n- Bi_2Te_3 thin film thermoelectric cooling Peltier device earlier [4].

9.6 Measurements of photovoltage profile during the flight

The variation of photovoltage generated by the photo diodes mounted on sensor box #1 and 2 during the flight are shown in fig 33 (a) and (b), respectively. The measured photovoltage was larger in the altitude range from 15,000 to 25,000 m. The larger photovoltage confirmed the presence of ultra violet Sun light. In the presence of UV light oxygen converted into ozone gas. The larger photovoltage confirmed the presence of ultra violet Sun light. In the presence of UV light oxygen converted into ozone gas.

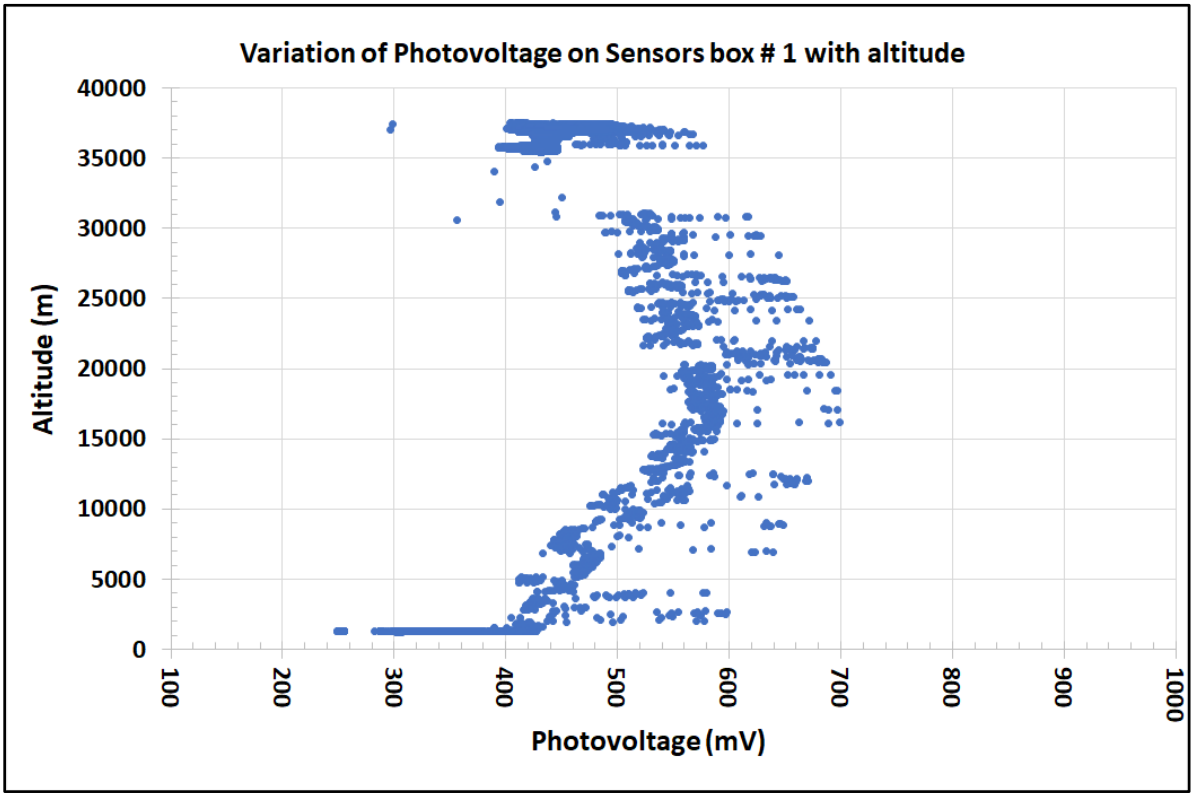

Fig.33 (a) Variation of photovoltage on sensor box#1

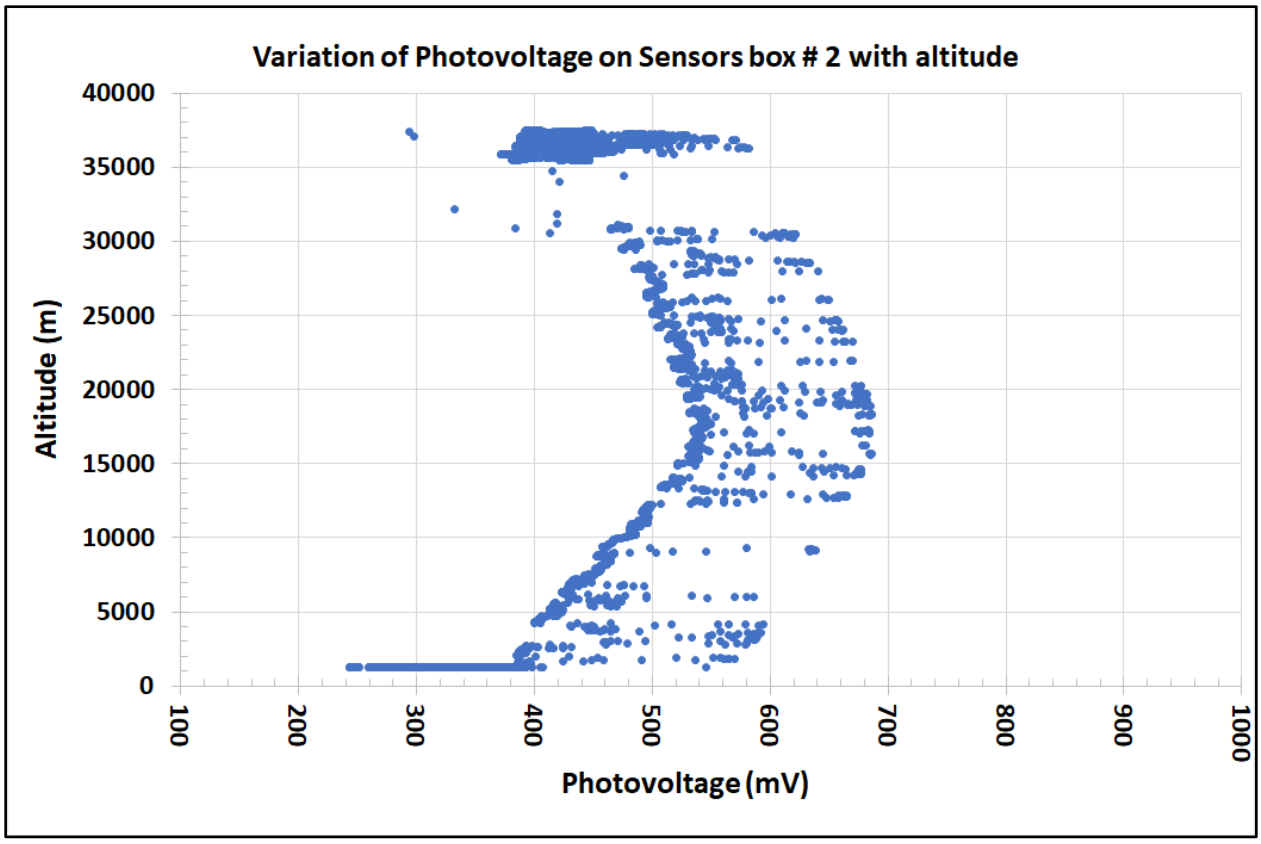

Fig.33 (b) Variation of photovoltage on sensor box#2

The variation of photovoltage generated by the photo diodes mounted on sensor box #1 and 2 with the flight time (UTC) are shown in fig 34 (a) and (b), respectively.

Photo sensor #3 has similar response of photovoltage as photo sensors # 1 and 2.

Fig. 34(a) and (b) shows three major zones:

(i) Ascending during day

The photovoltage voltage was maximum and shown a broad peak in the upper troposphere to middle of stratosphere.

(ii) Float during day

The photovoltage was nearly stable but several small spikes during float in daytime due to the balloon flight was traveling towards northeast direction.

(iii) Float during sunset time and then termination

The photovoltage was fluctuating with time and several spikes during beginning of sunset time due to up and down of reflection of sunlight.

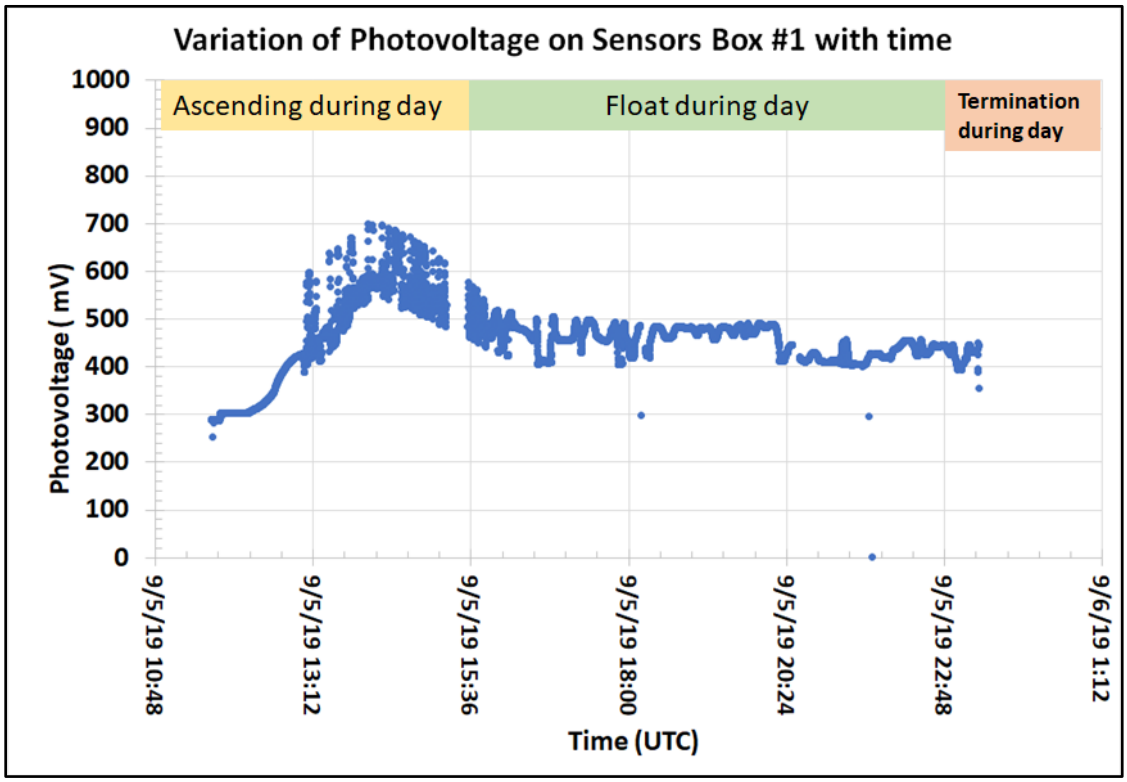

Fig.34 (b) Variation of photovoltage on sensor box#1 with time (UTC)

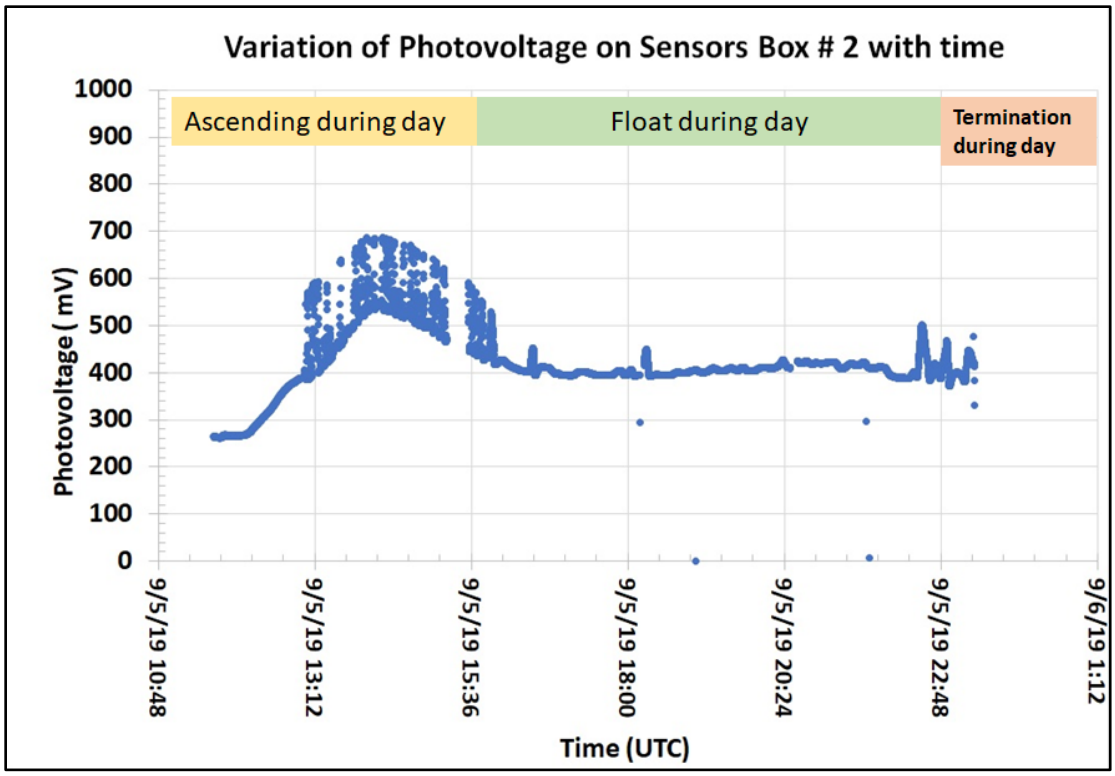

Fig.34 (c) Variation of photovoltage on sensor box#3 with time (UTC)

Important Note:
Question asked by Dr. Guzik during teleconference: Is there any effect of cold temperature in troposphere on response of UV light sensor?

Answer:

Usually response of semiconductor photodetector may change with temperature due to change in dark current and wavelength of incident light. We used a UV light sensor made by Gallium Phosphate (FGAP 71). https://www.thorlabs.com/drawings/fa30bfd7d0f7d907-2D354CB6-F36C-18BA-2AE7DC749EBC1531/FGAP71-SpecSheet.PDF

We tested response of UV light sensor at low and high temperature ranges few years before and found that there was slight decrease in response at low temperature and slight increase in response at higher temperature due to change in thermally generated carries. We are not able to find those results from our old desktop computer, but we will do it again and will update results to Dr. Guzik.

The spectral response of photodiode is show in fig. 34(d).

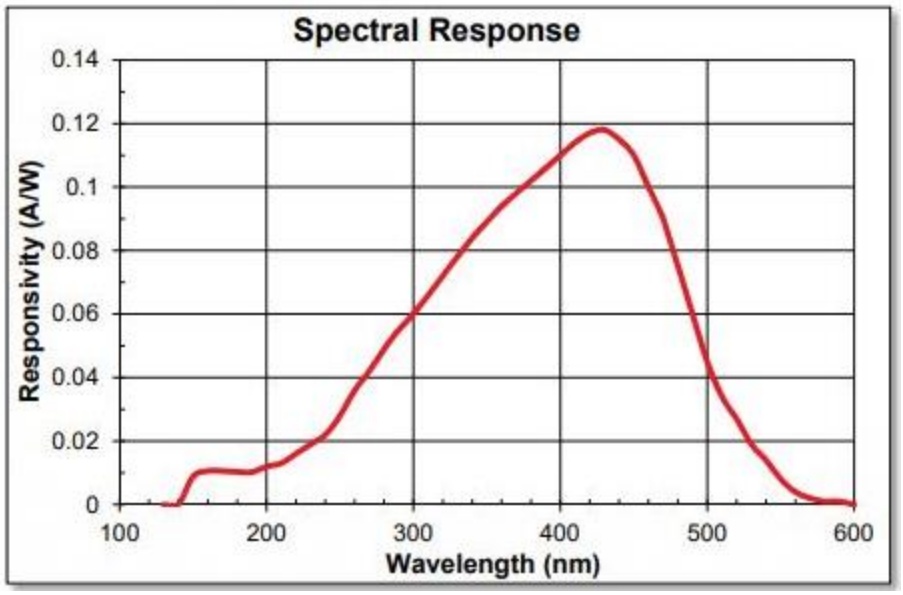

Fig. 34(c) Spectral response of UV light sensor - GaP photodiode FGAP 71.

Table # 3(b) shows the specifications of UV light sensor. Operating temperature range is about - 40 to 125 ^{o}C.

Table # 3(b) Specifications of UV light sensor.

Specifications

Specifications[a]		
Wavelength Range	λ	150 - 550 nm
Peak Wavelength	λ_P	440 nm
Responsivity	$\Re(\lambda)$	0.12 A/W
Active Area	-	2.2 mm x 2.2 mm
Rise/Fall Time (R_L=50 Ω, 5 V, 405 nm)	t_r/t_f	55 ns / 55 ns (Typ.)
NEP, Typical (440 nm, 5V)	W/√Hz	1.3×10^{-14}
Dark Current (5 V)	I_d	15 pA (Typ.) 40 pA (Max)
Capacitance (0 V)	C_j	1000 pF (Typ.)
Package	-	TO-39
Sensor Material	-	GaP

a. Unless otherwise noted, all measurements are performed at 25 °C ambient temperature.

Maximum Rating	
Max Bias (Reverse) Voltage	5 V
Reverse Current	2 mA
Operating Temperature	-40 to 125 °C
Storage Temperature	-40 to 125 °C

9.7 Discussion of Response of Gas Sensor Profile

Sensor # S1-4 was picked for the discussion of response of ozone sensor with the entire altitude range of balloon flight. An array of eight ozone sensors of Box-S1 was made of improved version of nanocrystalline ITO thin films compare to our previous balloon flights. These sensors have better selectivity and sensitivity with ozone gas. Fig. 35 shows the variation of resistance of ozone sensor S1-4 with time during entire flight, while fig.36 shows the variation of concentration of ozone measured by sensor S1-4 with time during entire flight. Note that there was no data available immediate after termination of flight due to no data communications.

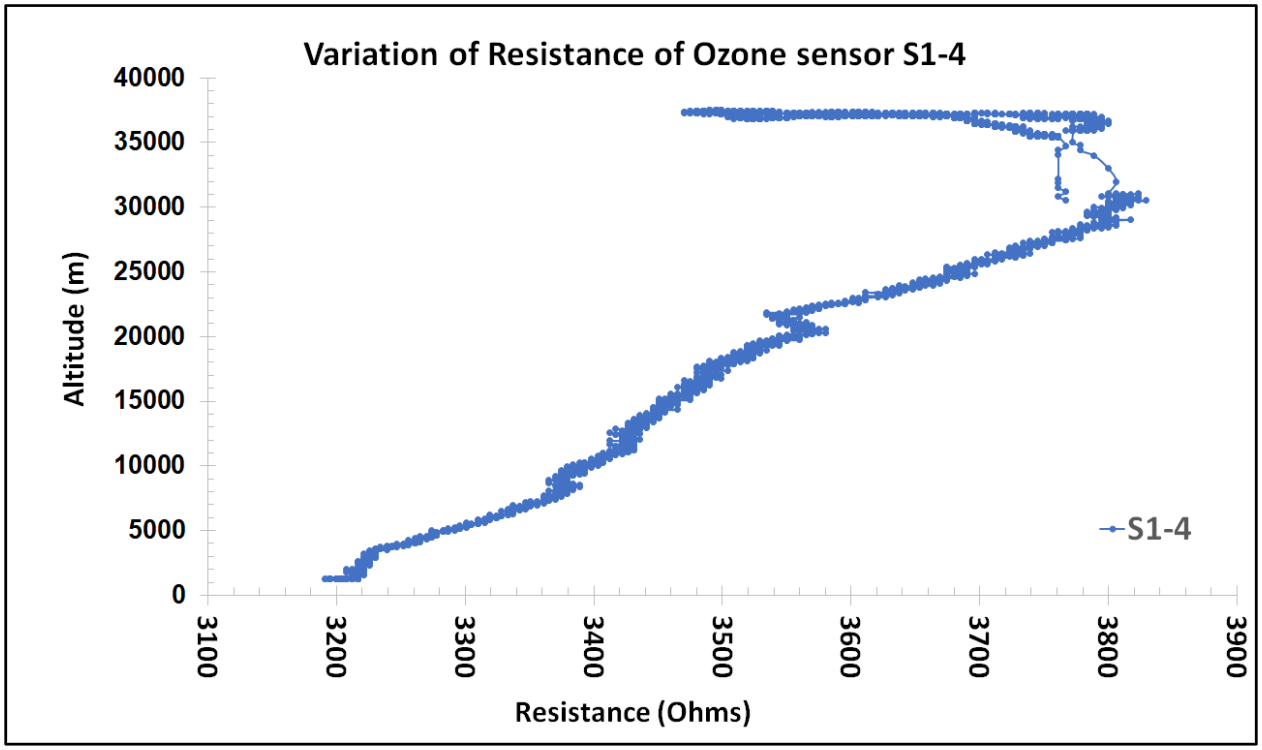

Fig. 35 Variation of resistance of ozone sensor S1#4 with time during entire flight.

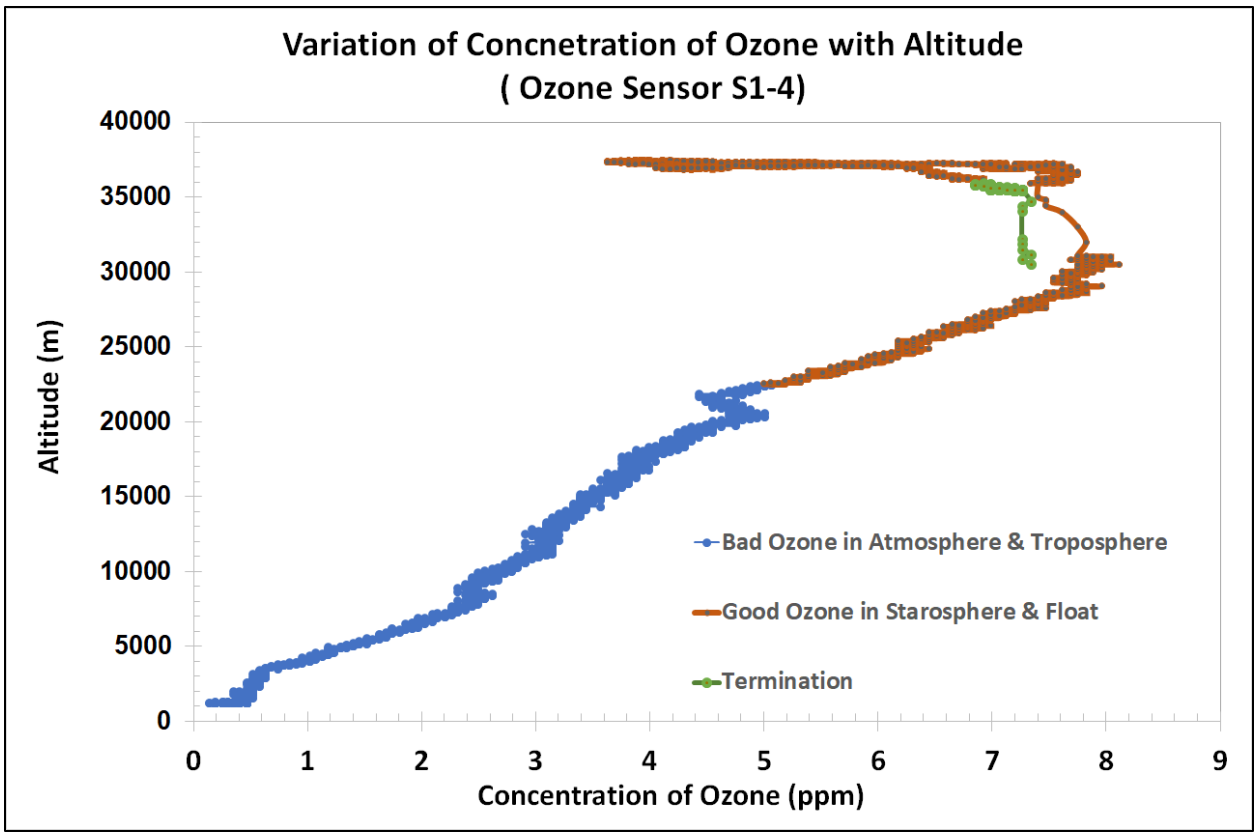

Fig.36 Variation of concentration of ozone measured by sensor S1#4 with flight time.

A small peak of ozone (blue color part in fig. 36 was observed during ascending of balloon flight at the altitude around 20,000 m. This range of altitude is from atmosphere to the troposphere. This small ozone peak is called as the bad ozone, which is mainly due to the generation of smog in the early morning due to pollutant gases from the automobile vehicles and industries. Due to low ambient temperature, pollutant gases were not able to disperse and diffuse. These pollutant gases and air particulates form the smog and hence form bad ozone. The bigger peak of ozone is observed at altitude above 20,000 to 37,000 m (orange color part in fig.36. This is due to the ozone in the stratosphere. This ozone is called as good ozone. In the presence of ultra violet light from Sun, oxygen converted into ozone gas. The concentration of ozone is higher in the middle to upper level of stratosphere in the presence of ultra violet light. Ozone is oxidizing gas and its concentration depends on amount of available Sun light. Upon adsorption of charge accepting molecules at the vacancy sites from ozone oxidizing gas, the electrons are effectively depleted from the conduction band of n-type Indium tin oxide (ITO) semiconductor sensor. Thus, this leads to an increase in the electrical resistance of n-type ITO gas sensor. During float of the balloon, the concentration of ozone should be constant, but it may vary due to variation of altitude, mixing ratio and availability of ultra violet rays from the sun during flight time. The concentration of ozone decreased slowly during float. It fluctuate several times due to dropping of altitude of balloon as well as less availability of UV light during beginning of sunset time.

After termination of balloon from float (green color part in fig.36) at the beginning of sunset, the payload again descending through the middle of stratosphere, then troposphere, and finally atmosphere. Due to no data communications, we were not able to get any data during descending. We were not able to find any possibility of ozone peak due to nocturnal ozone or formation of

Fig. 37 shows variation of concentration of ozone of measured by ozone sensor # S1-4 with time.

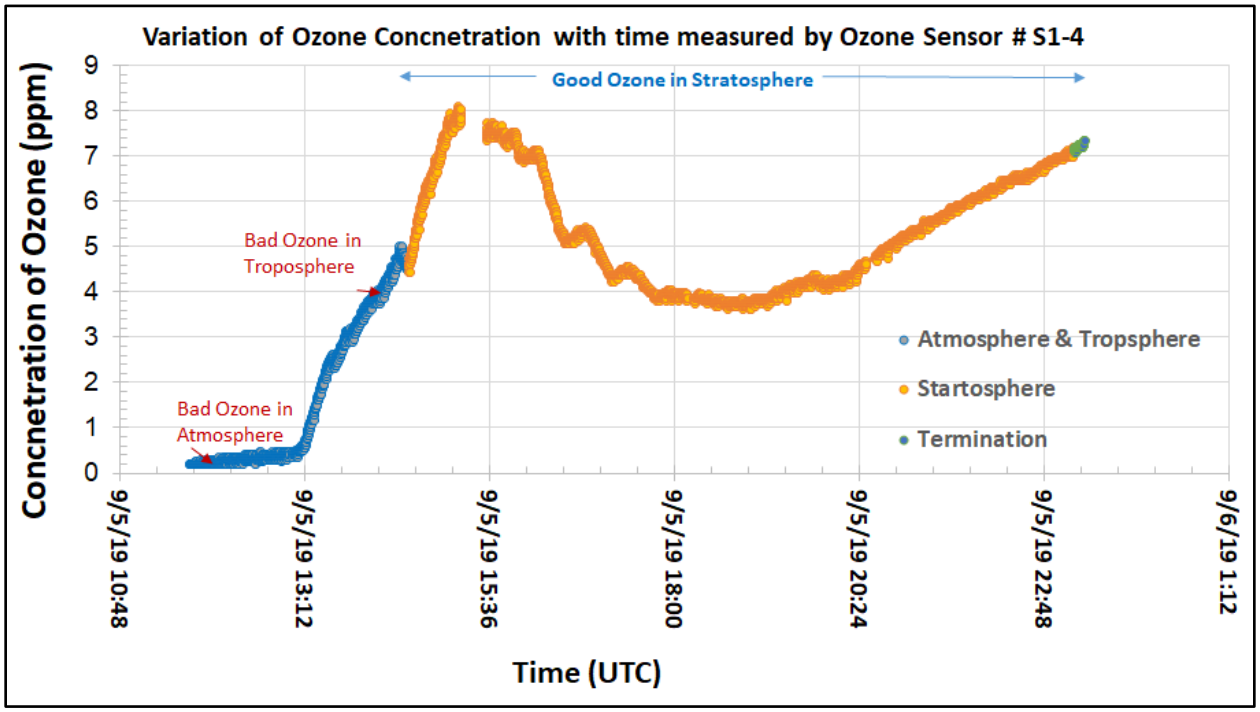

Fig. 37 Variation of concentration of ozone of measured by ozone sensor #S1-4 with time/

Response of other sensors in stratosphere was nearly similar to that of sensor #S1-4.

9.8 Response of ozone sensors during the flight

Response of all eight ozone sensors of box #1 (S1) and box # 2 (S2) in the stratosphere are shown in Fig. 38 (a) and 38 (b), respectively.

Ozone sensors of box #3 (S3) worked in the stratosphere during float. Fig. 38 (f) shows response of ozone sensors in limited altitude range of stratosphere.

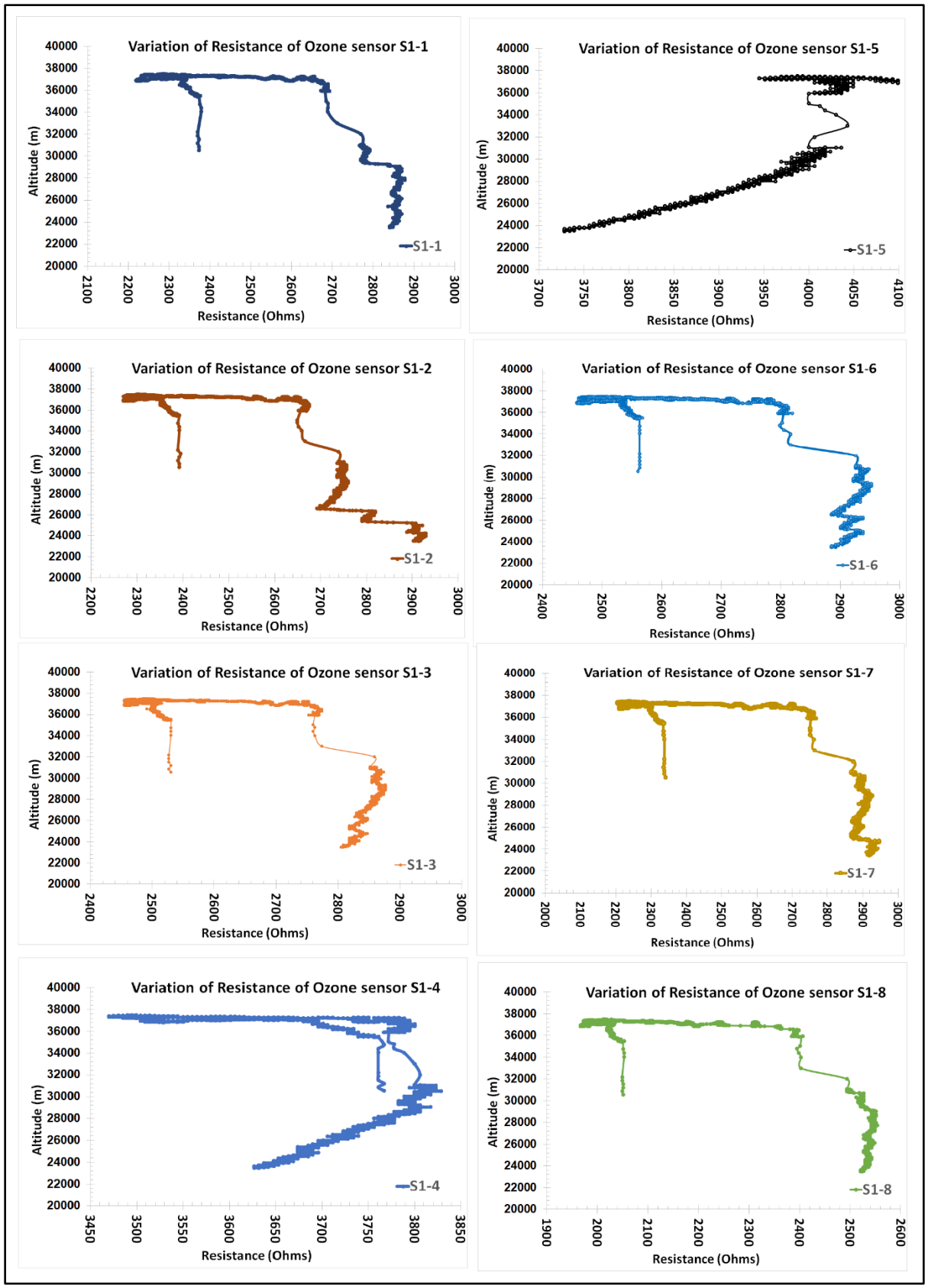

Fig.38 (a) Response of all ozone sensors of box #1 (S1) in the stratosphere altitude range

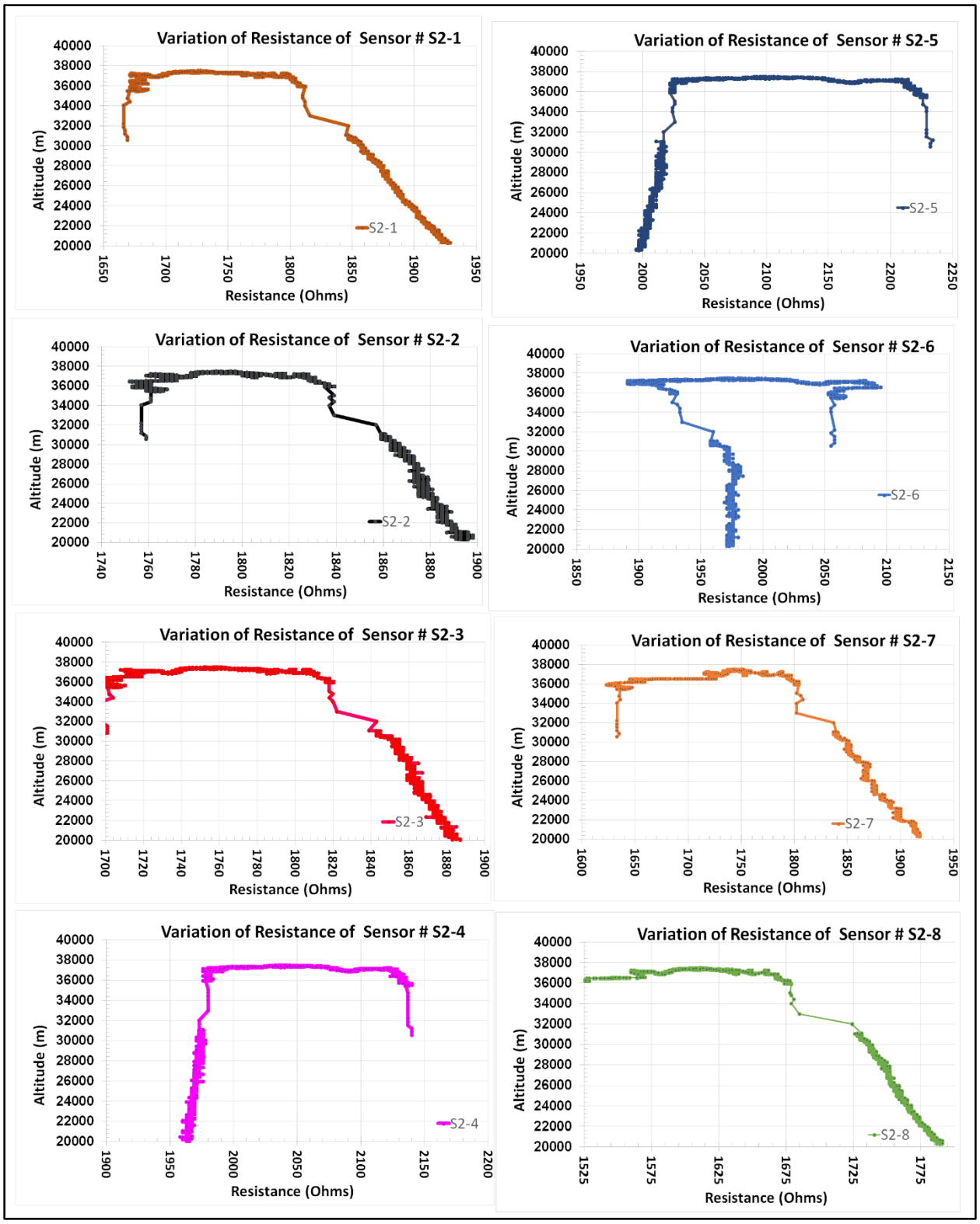

Fig.38 (b) Response of all ozone sensors of box #2 (S2) in the stratosphere altitude range

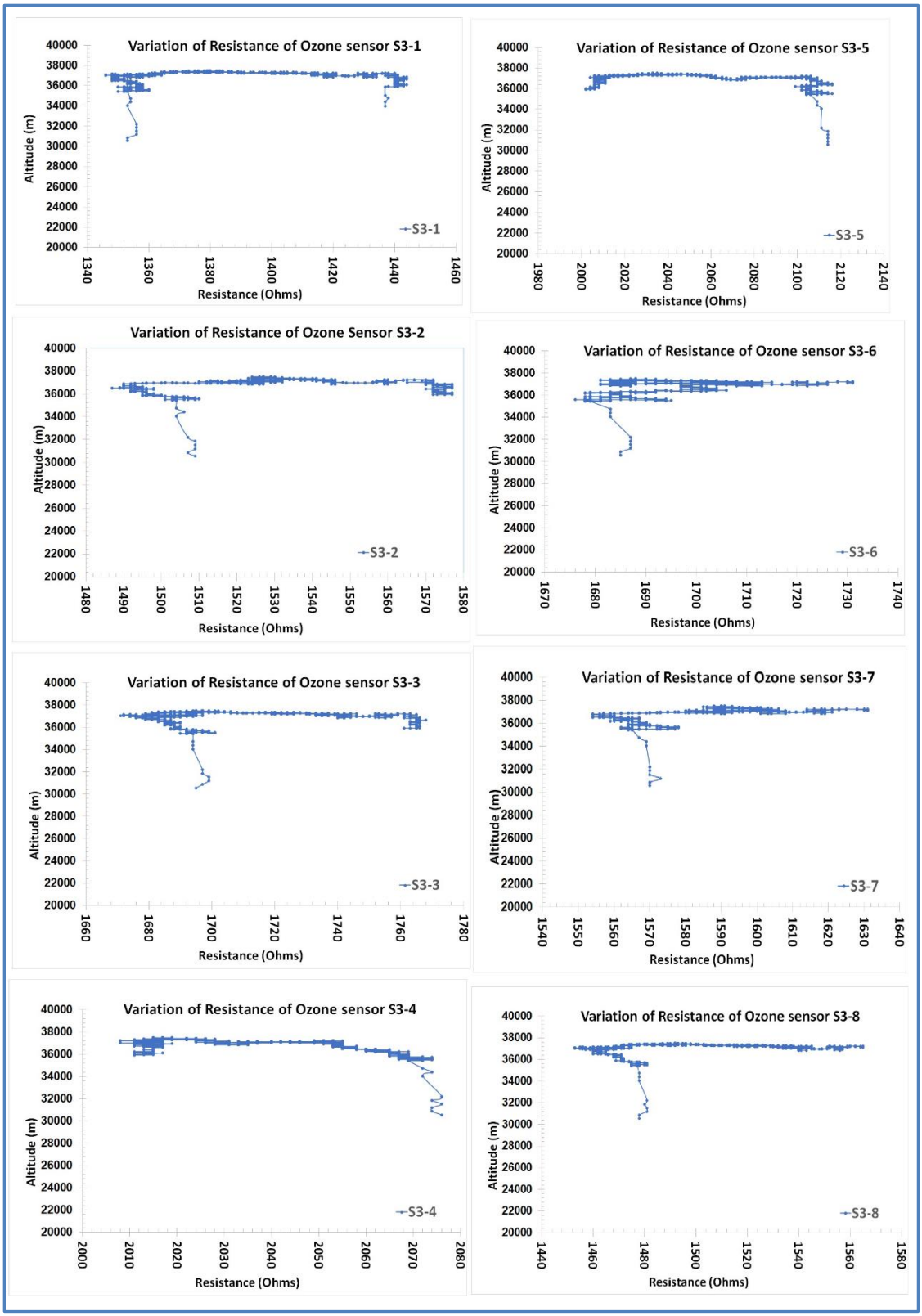

Fig.38 (c) Response of all ozone sensors of box # 3(S3) during **float time in the stratosphere**.

9.9 Measrements of ozone profile in the starosphere and comparision with the theorectical profile

We focused mainly on good ozone in stratosphere and hence measured the ozone profile in the stratosphere. Using calibration plots shown in fig. 7(a) and (b), the trend line equation of plot of each sensor was applied to convert the resistance values of the sensors into concentration of ozone gas in ppm. Note that the calibation was made in the low pressure, which can be applied mainly to starosphere range. It may be different for atmosphere and tropsphere data. The ozone concentration measured from 0 to 10.0 ppm may have slight different value of slope and y intercept due to experimental error due to the variation of sensors thickness, doping and oxidation and variation in chamber pressure due to minor leakage in the chambe with time.

The trend line equation of the calibration plot is given as:

$\boldsymbol{y}$ (sensor resistance, ohms) = [$\boldsymbol{m}$ (slope). $\boldsymbol{x}$ (concentration of ozone, ppm)] + $\boldsymbol{b}$(y intercept)

The concentration of ozone gas can be determined by: $\boldsymbol{x = (y - b)/m}$

The trendline equations for each sensors were listed in the following table-5.

Table-5 Fit parameters of trend line equations determined from the calibration plots shown in fig.7 (a) and (b) of sensor box # S1 and S2.

Ozone Sensor Box # S1				Ozone Sensor Box # S2			
Sensor Number	Slope (m)	y interecept (b)	Coreleation Coefficent (R^2)	Sensor Number	Slope (m)	y interecept (b)	Coreleation Coefficent (R^2)
S1-1	74.96	2278.3	0.9999	S2-1	35.10	1680.6	0.9999
S1-2	80.09	2250.5	0.9999	S2-2	25.08	1749.7	0.9997
S1-3	52.81	2466.5	0.9997	S2-3	25.08	1699.7	0.9997
S1-4	80.62	3177.0	0.9996	S2-4	25.09	1949.7	0.9997
S1-5	80.18	3599.4	0.9999	S2-5	35.06	1949.9	0.9999
S1-6	70.26	2399.0	0.9998	S2-6	37.10	1799.7	0.9998
S1-7	80.26	2299.1	0.9999	S2-7	49.83	1610.5	0.9997
S1-8	72.18	1999.3	0.9999	S2-8	25.09	1599.8	0.9997

With these equation fit parameters, we obtained the following the ozone profile plots shown in fig.39 (a) and (b):

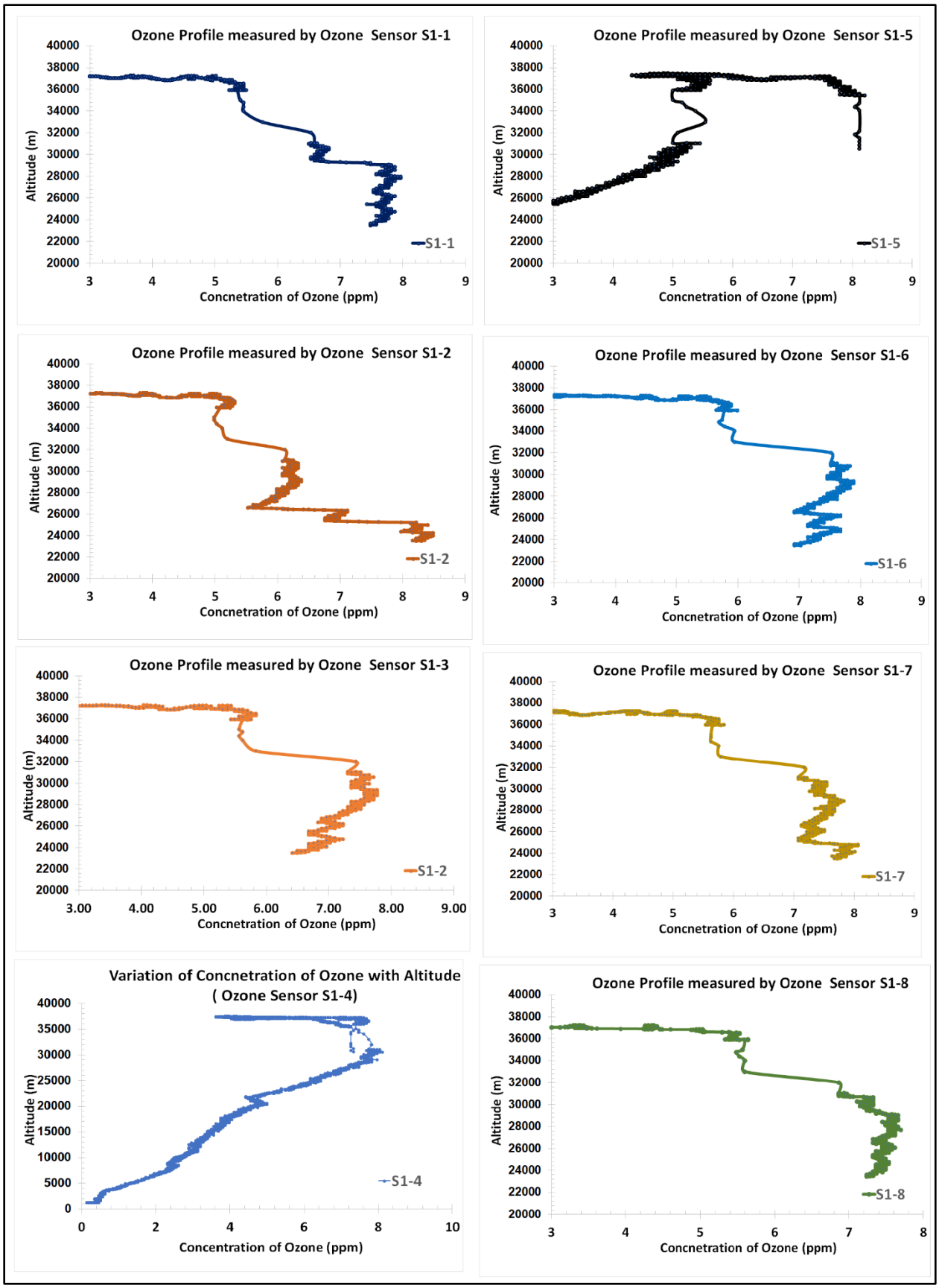

Fig. 39 (a) Ozone profile measured by sensors # S1-1 to S1-8.

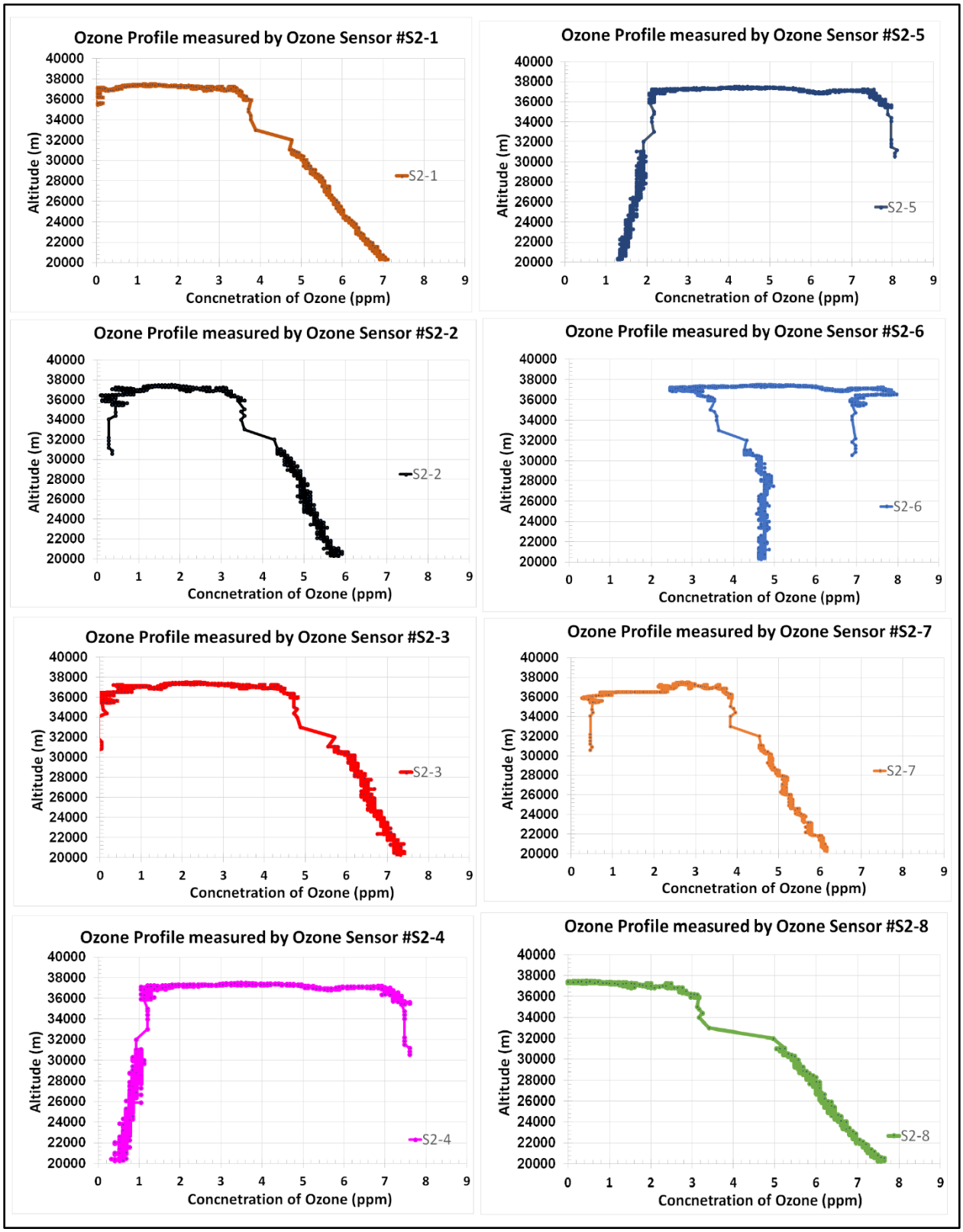

Fig. 39 (b) Ozone profile measured by sensors # S2-1 to S2-8.

The nature of ozone profiles measured by ozone sensors box # S1and S2 are nearly matched with the theoretically profile measured and quoted by various research groups, which are shown in Fig. 40(a) to (d) for the comparison purpose. The measured value of maximum concentration of ozone was observed about 8.00 ± 0.30 ppm, which is very close to the expected values reported earlier. We will find out some theoretical calculation method to generate theoretical data for comparison.

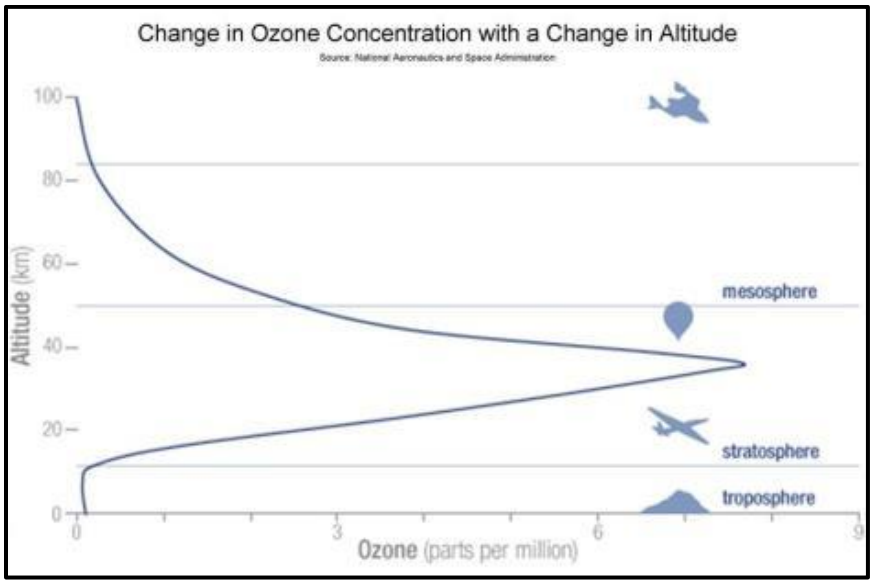

Fig.40 (a) Change in ozone concentration with a change in altitude.
Picture Courtesy: http://sites.gsu.edu/geog1112/lab-2-part-2/

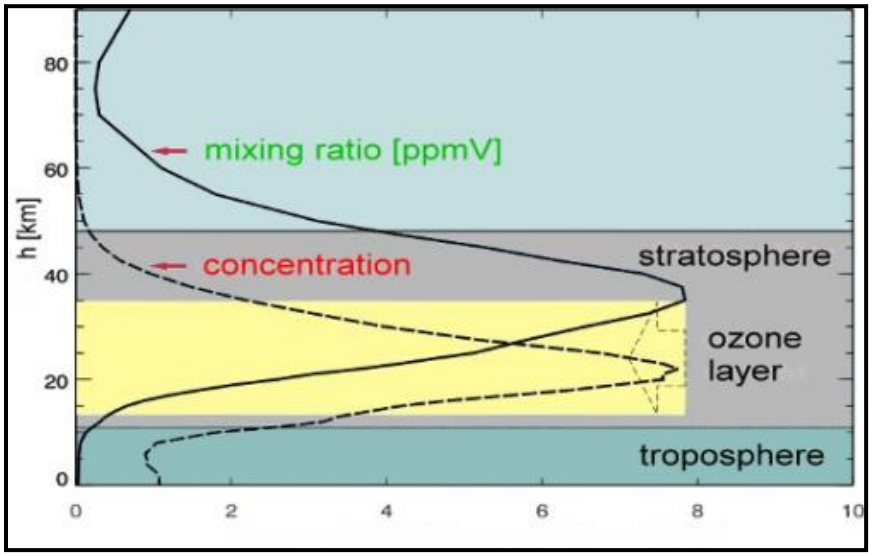

Fig.40 (b) Theoretical ozone profile in stratosphere
Picture Courtesy: http://www.atmosphere.mpg.de/enid/1yy.html
(ppmv = parts per million by volume = volume mixing ratio)

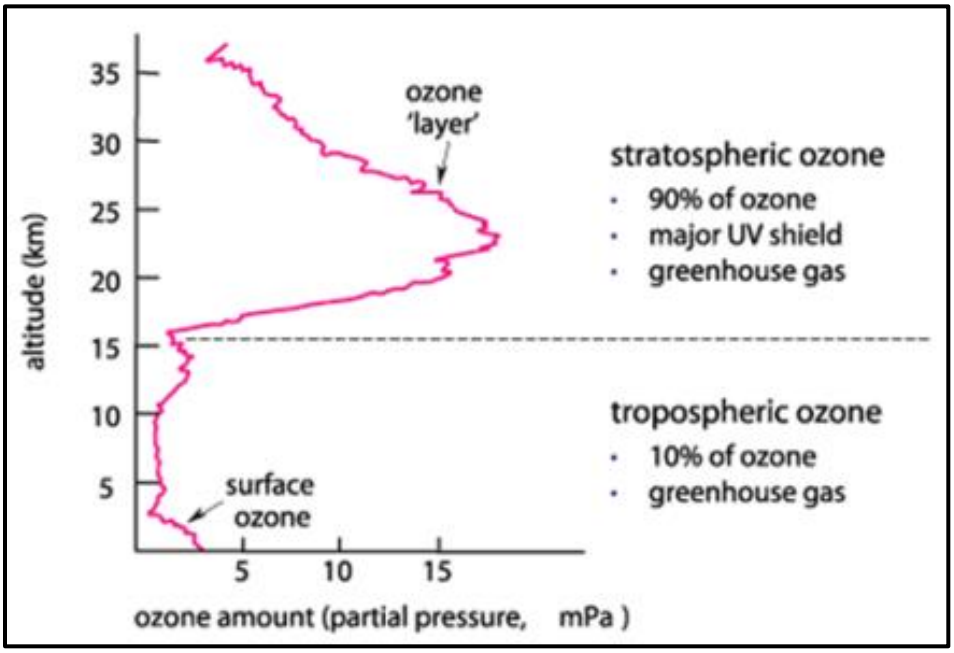

Fig.40(c) Ozone in the atmosphere with its impact

http://www.environment.gov.au/soe/2001/publications/theme-reports/atmosphere/atmosphere03-1.html

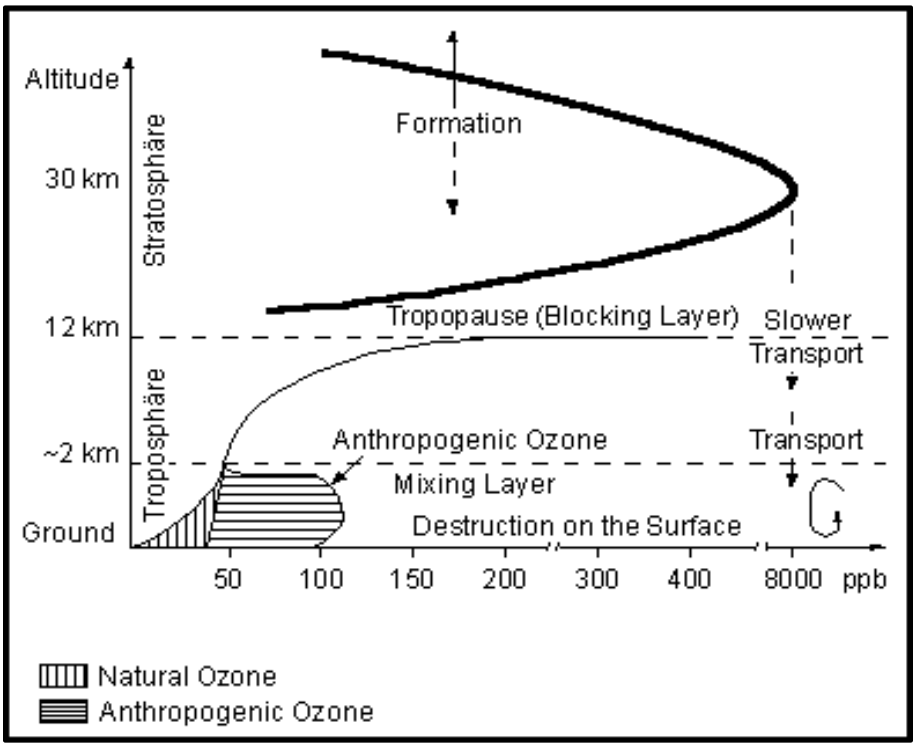

Fig.40 (d) Ozone profile

Courtesy :http://www.stadtentwicklung.berlin.de/umwelt/umweltatlas/ed306_01.htm

10. Problems, failure analysis and future

(1) HASP 2019 flight was completed on single day of September 5, 2019 mostly during daytime. The flight was terminated before nighttime. Therefore, ozone profile peak are not sharp but broad.

(2) Our nanocrystalline ozone gas sensors (Box # S1 and S2) made using ITO and WO_{3-x} + ITO composite thin films worked well for measurement of ozone profile. We made new composite of Ag_2WO_4+ITO to enhance detection of ozone in the stratosphere as well as bad ozone in atmosphere and troposphere and nocturnal ozone at nighttime. Sensors of box #3 worked in the stratosphere, but selectivity of ozone in troposphere was low due to interference and contribution of other reducing pollutant gases. In addition, we found development of many micro cracks on the upper layer of sensors due to partial change in α phase of silver tungstate material to β phase of silver tungstate material by aging of lattice, structural change and oxidation. Ultimately, sensitivity and selectivity for detection of oxidizing gas such as ozone affected. Hence, calibration of these sensors after flight was not match with calibration of sensors parameters before flight within 2-sigma deviation. We therefore did not converted measured response of sensors in the concentration of ozone in ppm. We will continue to improve the performance of sensors by changing materials, composition, and fabrication parameters of sensors.

(3) We have focused on measurements of good ozone in the stratosphere. In addition, we have also focused on measurements of bad ozone in atmosphere and troposphere. Measurements of bad ozone is equally important as good ozone. We did not able to observe any possible nocturnal ozone maxima at nighttime because early termination of flight before night.

(4) We did not get data files after termination and during descending due to no availability of data communications.

(5) Pressure sensor was saturated at 110 mbar. We found that that pressure sensor can work only up to 110 mbar. We planned to replace it by new pressure sensor in the next flight.

(6) We are working on development and fabrication of nano sensors using an electron beam lithography technique (www.raith.com) attached with scanning electron microscope. We are interested to examine the performance of nano sensors. We will accelerate our work and we may try it in the next HASP 2020 or 2021 balloon flight.

11. Conclusions

(i) All UNF students' team members worked HASP first time very well.

(ii) The payload worked very well during the flight. We got very good data during the flight.

(iii) Our science objectives of all sensors were successfully tested and scientifically verified for measurement of good ozone in stratosphere. We will further improve the performance of our gas sensors and payload during next HASP flight.

(iv) The improved nanocrystalline ITO thin film gas sensors (Box#1) and nanocomposite WO_{3-x} +ITO thin film gas sensors fabricated (Box#2) by the UNF team have good selectivity with ozone gas and worked well during entire flight period and measured the ozone profile of the stratosphere. The fabrication parameters of nanocomposite Ag_2WO_4+ITO thin film gas sensors need to improve and stabilize it phase.

(v) Light sensor proved the presences of UV light, which are responsible to generate more ozone gas by converting oxygen into ozone. We will further investigate any effect of temperature on response characteristics.

(vi) Improved temperature control circuit and software program gave better stability of temperature of sensors during entire flight period. No need to reset or change the commands during the flight.

(vii) Our UBLOX GPS worked well without any issue of blocking data.

(viii) New modified JAVA based software handles all sensors data and faster conversion of RAW file into EXCEL file for quick view of the plots. LabVIEW program will further improve for better monitoring of real-time monitoring the plots.

(ix) After receiving payload back, we found the payload is working in good condition.

(x) We will focus again to measure bad ozone in atmosphere and troposphere and nocturnal ozone at nighttime, in addition to good ozone in stratosphere in the next HASP flight.

(xi) UNF team is interested to make further improve sensors payload and seeking another opportunity for the next HASP flight.

12. References

[1] Perry J. Samson, "Nocturnal Ozone Maxima"
Atmospheric Environment, Vol.12 (1978) 951-955.

[2] A. Mavrakis, H. Flocas, E. Mavromatidis, G. Kallos, G. Theoharatos and A. Christides, "A Case of Nightime High Ozone Concentration over the Greater Athens Area", Meterologische Zeitschrift, Vol. 19, No.1 (2010) 035-045.

[3] R. San Jose, A. Stohl, K. Karatzas, T. Bohler, P.James and J.L. Perez, "A Modelling Study of an Extraordinary Night Time Ozone Episode over Madrid Domain". Environmental Modelling & Software 20 (2005) 587-593.

[4] Thermoelectric cooling effect in a p-Sb2Te3-n-Bi2Te3 thin film thermocouple
N. G. Patel and P.G. Patel
Solid State Electronics, Vol 35, No.9 (1992) 1269-1272 (UK)

13. Acknowledgements

We are very grateful to

(i) Dr. Gregory Guzik and Mr. Doug Granger HASP-LSU for their continuous help, cooperation and encouragement. We also appreciate help of Mr. Doug Granger for sharing temperature data and pictures. We also thankful to Mr. Anthony Ficklin and Mr. Joshua Collins for their cooperation during the thermal vacuum test.

(ii) Columbia Scientific Balloon Facilities (CSBF)-NASA and Northrop Grumman, Palestine TX and CSBF, Fort Sumner, NM, and their team.

(iii) Florida Space Grant Consortium and Dr Jaydeep Mukherjee, Director, Florida Space Grant Consortium (FSGC) for support and encouragement.

(iv) Websites links mentioned in this report for using their pictures and references to explain the science of this report. Our intention is not to violate any copyright, but purposes of education and research training.

14. Presentation of Research work.

(a) UNF students' team (Joseph, Kyle and Karli) presented a research poster on "Measurements of Ozone Profile Using Ozone Sensor Payload on HASP 2019 Flight" at UNF – Physics, Chemistry and Biology Departments poster session on Friday, November 1, 2019.

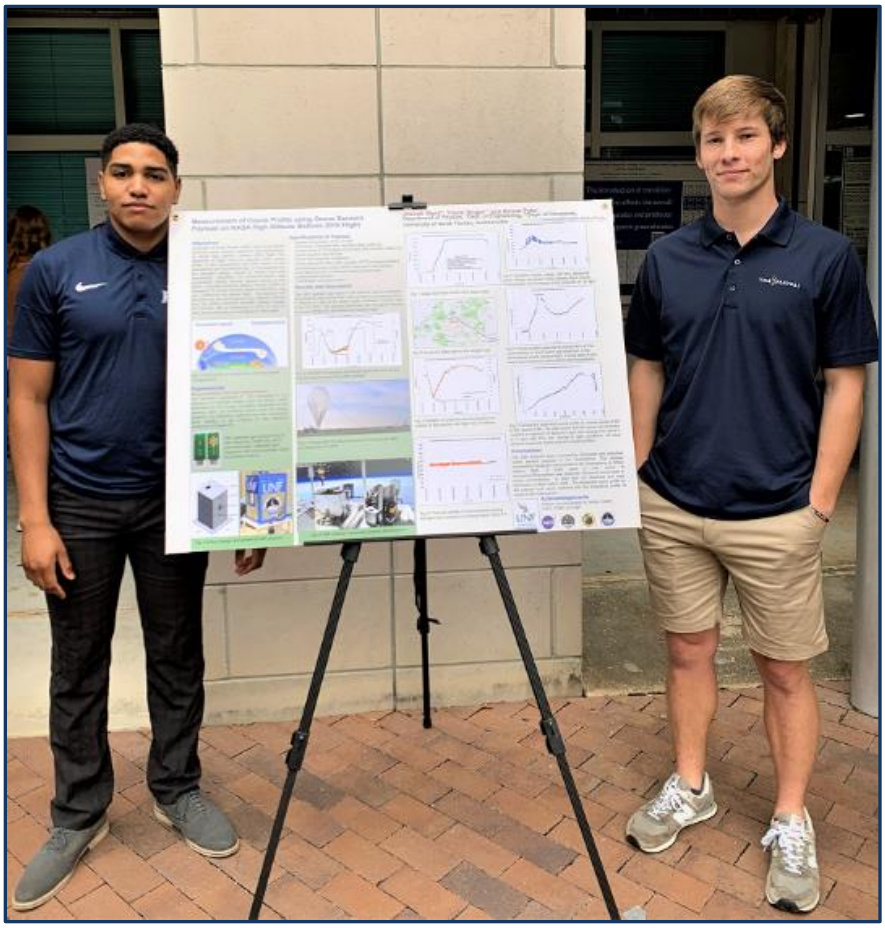

Joseph and Kyle (UNF) presented a research poster.

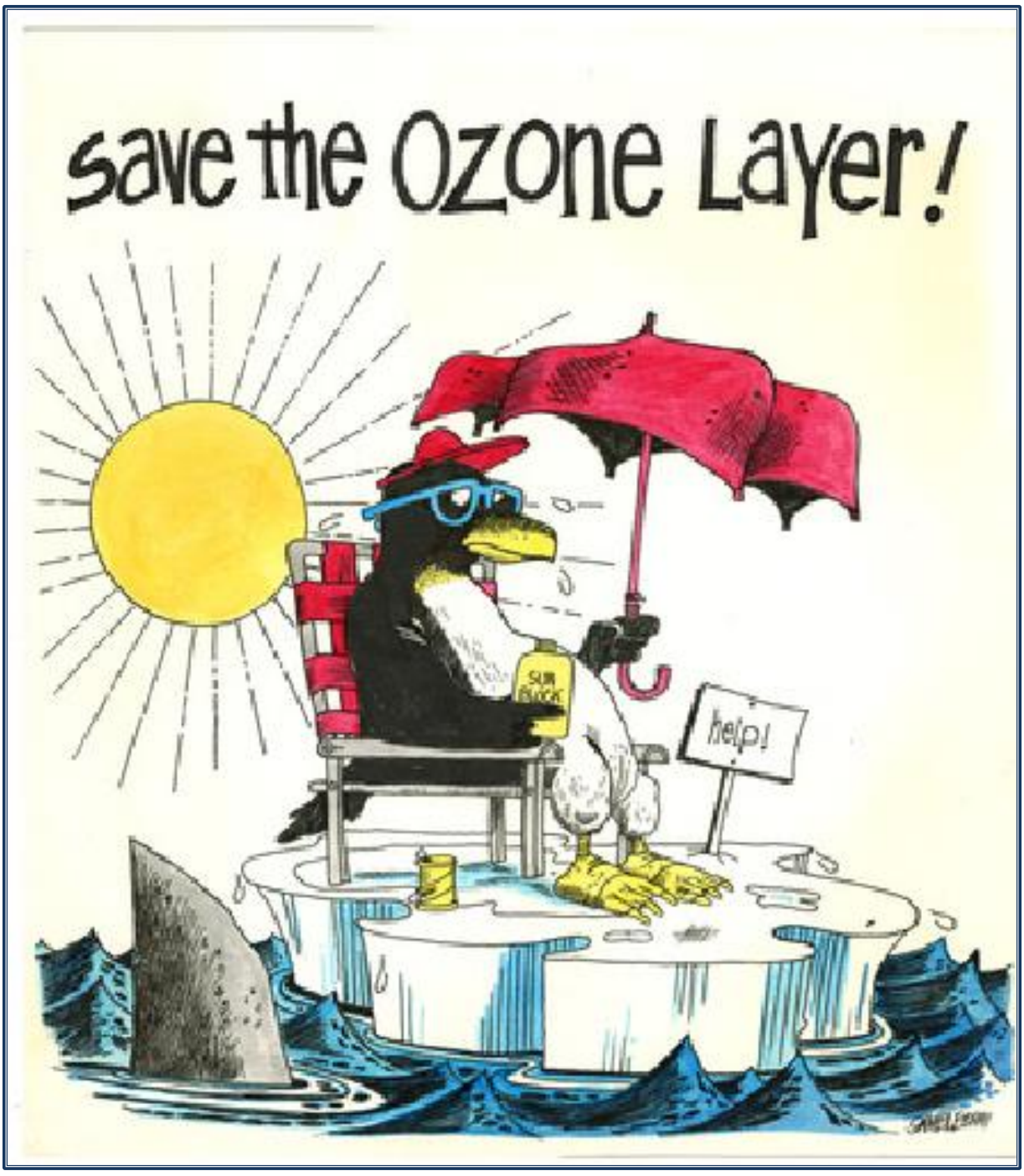
save the Ozone Layer!
help!